5
Results and Discussion

Regression models derived from experimental and characterization findings of developed electrode coatings are discussed in this chapter. It also addressed the impact of electrode coating components on the different properties and used analysis of variance (ANOVA) to verify that the established regression models are adequate. This chapter also analyses the findings of numerous experiments on the dissimilar welds produced. Results from mechanical and microstructural analyses of the welds are also thoroughly covered.

5.1 Establishing regression models to analyze electrode coating's physicochemical, thermophysical, and wettability properties

The experiment aimed to measure the physicochemical, thermophysical, and wettability properties, such as density, change in enthalpy, weight loss, thermal diffusivity, thermal conductivity, specific heat, and wettability of the flux coatings. The results are summarized in Table 5.1 and Table 5.2. The developed regression models are analyzed using linear, quadratic, cubic, and special cubic parameters based on the percentage of electrode coating compositions, individual constituents, and their binary and ternary interaction, as shown in Eq. 5.1- 5.10.

Density (g/cm³) = -0.12145 x CaO -0.93281 x SiO_2 -0.19310 x TiO_2-0.45225 x Na_3AlF_6 -2.88354E-003 x CaO x SiO_2 -8.53358E-003 x CaO xTiO_2 +0.013957 x CaO x Na_3AlF_6 +0.033272 x SiO_2 x TiO_2 +0.060507 x SiO_2 x Na_3AlF_6 +0.022961 x TiO_2 x Na_3AlF_6 +1.33991E-003 x CaO x SiO_2 x TiO_2 -1.00729E-003 x CaO xSiO_2 x Na_3AlF_6 +1.56109E-004x CaO xTiO_2 x Na_3AlF_6-2.06096E-003 xSiO_2 xTiO_2 xNa_3AlF_6 Eq. **(5.1)**

Enthalpy Change (J/g) = -1.14477E+005 x CaO+ 21233.11175 x SiO_2 -2090.01168 x TiO_2 +69530.36827 x Na_3AlF_6 +2326.71830 x SiO_2 x CaO +1465.58112 x TiO_2x CaO +1385.53505 x Na_3AlF_6 x CaO -1208.39445 x SiO_2 x TiO_2 -2649.31279 x SiO_2 x Na_3AlF_6 -1882.03137 x TiO_2 x Na_3AlF_6 +40.94364 x CaO x TiO_2 x Na_3AlF_6 +67.43947x SiO_2 x TiO_2 x Na_3AlF_6 +73.13842 x CaO x Na_3AlF_6 x (CaO Na_3AlF_6)+20.74788 x TiO_2 x Na_3AlF_6 x (TiO_2-Na_3AlF_6) Eq. **(5.2)**

Thermal Conductivity (W/mK) =+0.064930xCaO-0.56061xSiO_2+0.075337x TiO_2+3.10905E-003xNa_3AlF_6+0.011191x SiO_2xCaO-4.28553E-003xTiO_2xCaO+1.92916E-004xCaO x Na_3AlF_6 +2.38706E-003 x SiO_2 x TiO_2+0.017131x SiO_2 x Na_3AlF_6 -1.52251E-003 xTiO_2 x Na_3AlF_6 +2.38302E-004 x TiO_2 x SiO_2x CaO -3.03148E-004 x SiO_2 x CaO x Na_3AlF_6-1.80996E-004 x CaOxSiO_2x(CaO-SiO_2)+1.69089E-004xSiO_2xNa_3AlF_6x(SiO_2-Na_3AlF_6) Eq. **(5.3)**

Thermal Diffusivity(mm²/s)= +0.85463 x CaO +3.88835 x SiO_2 +2.25113 x TiO_2 -1.57343 x Na_3AlF_6 -0.070927 x CaO x SiO_2- 0.051650 x CaO x TiO_2 +8.23502E-003 x CaO x Na_3AlF_6-0.11530 x SiO_2 x TiO_2-0.083143 x SiO_2 x Na_3AlF_6 -0.020474 x TiO_2 xNa_3AlF_6+6.27495E-004 x CaO xSiO_2 x Na_3AlF_6 +1.22337E-003x SiO_2 xTiO_2 x Na_3AlF_6 +5.23417E-004 x CaO x TiO_2 x (CaO-TiO_2)-9.02373E-004 x CaO x Na_3AlF_6 x (CaO-Na_3AlF_6)-1.53269E-003 x SiO_2 x Na_3AlF_6 x (SiO_2-Na_3AlF_6)-1.23427E-003xTiO_2xNa_3AlF_6x(TiO_2-Na_3AlF_6) Eq. **(5.4)**

Specific Heat (MJ/m³K)= -3.92436 x CaO -36.26039 x SiO_2 -10.89031 x TiO_2 +7.65958 x Na_3AlF_6 +0.78418xSiO_2xCaO+0.25857xTiO_2xCaO-0.029402xNa_3AlF_6xCaO +0.90362 x SiO_2 x TiO_2+0.81442 x SiO_2 x Na_3AlF_6+0.10118 x TiO_2 x Na_3AlF_6 -4.07497E-003 x CaO x SiO_2 x TiO_2-9.18026E-003 x CaO xSiO_2 x Na_3AlF_6 -9.99128E-004 x CaO xTiO_2 x Na_3AlF_6-8.62426E-003 x SiO_2 x TiO_2 x Na_3AlF_6-3.61194E-003xCaOxSiO_2x(CaO-SiO_2)-2.69417E-003x CaO x TiO_2 x(CaO-TiO_2) +4.22733E-003 x CaO x Na_3AlF_6 x (CaO-Na_3AlF_6) +2.14796E-003 x SiO_2 x TiO_2

$x(SiO_2\text{-}TiO_2)+0.010316xSiO_2xNa_3AlF_6x(SiO_2\text{-}Na_3AlF_6)+6.08624E\text{-}003xTiO_2xNa_3AlF_6x\ (TiO_2\text{-}Na_3AlF_6)$ Eq. **(5.5)**

Weight Loss (mg) = $+12.82256 \times CaO -15.71052 \times SiO_2 -14.46427 \times TiO_2 -1.85613 \times Na_3AlF_6 +0.15874 \times SiO_2 \times CaO -0.096912 \times TiO_2 \times CaO -0.16800 \times Na_3AlF_6 \times CaO +0.75864 \times SiO_2 \times TiO_2 +0.59166 \times SiO_2 \times Na_3AlF_6 +0.41003 \times TiO_2 \times Na_3AlF_6 -0.014361 \times SiO_2 \times Na_3AlF_6 \times CaO -0.018193 \times TiO_2 \times SiO_2 \times Na_3AlF_6 -0.011199 \times CaO \times TiO_2 \times (CaO\text{-}TiO_2) +2.43476E\text{-}003 \times TiO_2 \times Na_3AlF_6 \times (TiO_2\text{-}Na_3AlF_6)$ Eq. **(5.6)**

Contact Angle (θ^o) = $-67.90436 \times CaO - 52.76254 \times SiO_2 +56.21861 \times TiO_2 -1.62320 \times Na_3AlF_6 +2.87326 \times CaO \times SiO_2 -0.42076 \times CaO \times TiO_2 -1.99903 \times CaO \times TiO_2 -0.53522 \times SiO_2 \times TiO_2 +1.03731 \times SiO_2 \times Na_3AlF_6 -1.42550 \times TiO_2 \times Na_3AlF_6$ Eq. **(5.7)**

Spread Area (mm^2) = $-16238.51482 \times CaO + 31655.23605 \times SiO_2 -12853.71705 \times TiO_2 -11082.68363 \times Na_3AlF_6 -1092.37932 \times CaO \times SiO_2 +1047.83293 \times CaO \times TiO_2 +973.37637 \times CaO \times Na_3AlF_6 -704.12512 \times SiO_2 \times TiO_2 -211.62164 \times SiO_2 \times Na_3AlF_6 +796.60550 \times TiO_2 \times Na_3AlF_6 +35.67032 \times CaO \times SiO_2 \times TiO_2 +0.72511 \times CaO \times SiO_2 \times Na_3AlF_6 -45.50505 \times CaO \times TiO_2 \times Na_3AlF_6 -4.48880 \times SiO_2 \times TiO_2 \times Na_3AlF_6$ Eq. **(5.8)**

Adhesion Energy (J/M^2) = $-0.92990 \times CaO +2.12621 \times SiO_2 +0.035309 \times TiO_2 +0.17955 \times Na_3AlF_6 +0.016730 \times CaO \times SiO_2 +0.043862 \times CaO \times TiO_2 +0.025320 \times CaO \times Na_3AlF_6 -0.10170 \times SiO_2 \times TiO_2 -0.081450 \times SiO_2 \times Na_3AlF_6 -9.12422 \times 10^{-3} \times TiO_2 \times Na_3AlF_6 -4.57840 \times 10^{-4} \times CaO \times SiO_2 \times TiO_2 -4.33020 \times 10^{-4} \times CaO \times SiO_2 \times Na_3AlF_6 -1.12929 \times 10^{-3} \times CaO \times TiO_2 \times Na_3AlF_6 +3.98553 \times 10^{-3} \times SiO_2 \times TiO_2 \times Na_3AlF_6$ Eq. **(5.9)**

Surface Tension (mN/M) = $+9.58853 \times CaO +5.93387 \times SiO_2 +7.16397 \times TiO_2 +3.52264 \times Na_3AlF_6 -0.034136 \times CaO \times SiO_2 -0.011781 \times CaO \times TiO_2 +0.061477 \times CaO \times Na_3AlF_6 -0.038059 \times SiO_2 \times TiO_2 -0.038892 \times SiO_2 \times Na_3AlF_6 +0.011364 \times TiO_2 \times Na_3AlF_6$ Eq. **(5.10)**

5.1.1 Regression analysis for electrode coatings physicochemical, thermophysical, and wettability properties

Analyses of variance (ANOVA) were performed on the developed regression models. As shown in Table 5.3, this was done to see if the model was adequate and to determine the relevance of the input parameters and how they interacted with the responses.

Table 5.1: Experimental results of different physicochemical and thermophysical properties

Coating	Density (g/cm^3)	Change in enthalpy (J/g)	Thermal Conductivity (W/mK)	Thermal Diffusivity (mm^2/s)	Specific heat (MJ/m^3K)	Weight loss (%)
C1	1.67	-23725.91	0.2246	0.1854	1.211	18.52
C2	1.67	-21343.05	0.2151	0.2018	1.066	17.31
C3	1.63	-24037.61	0.2207	0.1886	1.170	14.31
C4	1.57	-21006.81	0.2262	0.2200	1.028	20.67
C5	1.59	-31519.18	0.2158	0.1964	1.099	17.22
C6	1.59	-24186.34	0.2234	0.2057	1.086	15.15
C7	1.60	-33713.12	0.2291	0.2198	1.043	14.34
C8	1.56	-26011.36	0.2294	0.2289	1.002	14.79
C9	1.59	-27352.16	0.2221	0.2036	1.091	15.59
C10	1.59	-20081.46	0.2299	0.2062	1.115	15.72
C11	1.58	-26914.17	0.2198	0.2184	1.006	25.80
C12	1.62	-21933.38	0.2199	0.2094	1.050	16.36
C13	1.53	-24481.64	0.2240	0.2227	1.006	16.77
C14	1.59	-30225.39	0.2208	0.2297	0.961	13.03
C15	1.61	-28113.10	0.2179	0.2040	1.068	16.41
C16	1.56	-24210.23	0.2133	0.2272	0.939	15.14
C17	1.58	-26275.23	0.2202	0.2413	0.912	16.02
C18	1.61	-28820.11	0.2168	0.2272	0.954	16.71
C19	1.62	-23586.18	0.2181	0.2078	1.050	15.22
C20	1.57	-19741.03	0.2201	0.2098	1.049	14.98
C21	1.58	-23714.41	0.2169	0.2095	1.036	10.96
C22	1.56	-22260.71	0.2264	0.2139	1.058	15.17
C23	1.63	-22702.01	0.2249	0.1955	1.151	15.56
C24	1.60	-22825.61	0.2265	0.2563	0.884	12.14
C25	1.57	-23914.05	0.2140	0.2164	0.989	14.81
C26	1.60	-22547.93	0.2286	0.2104	1.086	14.45

Table 5.2: Experimental results of different wettability properties

Coating	Contact angle (θ°)	Spreading Area (mm^2)	Adhesion energy (J/M^2)	Surface tension γ (mN/M)
C1	7.36	3967.80	0.8027	447.960
C2	0.00	4625.81	0.9143	457.126
C3	45.17	4491.88	0.7360	431.606
C4	90.00	399.19	0.4415	441.176
C5	0.00	3573.84	0.9130	456.519
C6	36.67	2760.92	0.7933	440.186
C7	49.38	3411.02	0.6934	419.923
C8	69.89	2617.79	0.5811	432.246
C9	28.24	3476.93	0.8506	452.204
C10	12.46	4514.33	0.8911	450.872
C11	34.95	4055.47	0.7443	408.970
C12	2.72	3600.33	0.9231	461.833
C13	32.04	3274.58	0.8251	446.520
C14	36.55	5149.36	0.8003	443.738
C15	36.55	5245.34	0.8792	448.134
C16	35.17	3070.82	0.8023	441.393
C17	6.39	2929.39	0.9183	460.597

C18	3.89	3199.46	0.9039	452.466
C19	26.55	2562.46	0.8352	440.833
C20	59.25	1468.44	0.6685	442.195
C21	0.00	4053.77	0.7904	395.196
C22	18.02	2993.22	0.8710	446.459
C23	0.00	4059.46	0.9262	463.104
C24	44.21	2254.78	0.7084	412.587
C25	49.58	2852.84	0.7141	433.139
C26	79.38	2923.57	0.5024	423.998

Table 5.3. ANOVA analysis of developed regression for measured properties

Property	*Source*	*Sum of squares*	*df*	*Mean square*	*F value*	*P value*	*Significance*	*R^2 value*
Density	Model	0.021	13	1.599E-003	4.05	0.0105	S	0.81
	Linear mixture	8.676E-003	3	2.892E-003	7.33	0.0047	S	
	SiO_2.CaO	4.271E-006	1	4.271E-006	0.011	0.9188	NS	
	TiO_2.CaO	3.035E-005	1	3.035E-005	0.077	0.7862	NS	
	Na_3AlF_6. CaO	1.423E-004	1	1.423E-004	0.36	0.5592	NS	
	TiO_2.SiO_2	7.081E-004	1	7.081E-004	1.80	0.2051	NS	
	Na_3AlF_6.SiO_2	3.471E-003	1	3.471E-003	8.80	0.0118	S	
	Na_3AlF_6.TiO_2	6.374E-004	1	6.374E-004	1.62	0.2277	NS	
	SiO_2.TiO_2.CaO	1.380E-003	1	1.380E-003	3.50	0.0859	NS	
	CaO.SiO_2.Na_3AlF_6	7.802E-004	1	7.802E-004	1.98	0.8828	NS	
	CaO.TiO_2.Na_3AlF_6	8.940E-006	1	8.940E-006	0.023	0.0126	S	
	SiO_2.TiO_2.Na_3AlF_6	3.390E-003	1	3.390E-003	8.60			
	Residual	4.733E-003	12	3.944E-004				
	Cor Total	0.026	25					
Enthalpy	Model	2.546E+008	13	1.959E+007	4.76	0.0054	S	0.84
	Linear mixture	1.682E+008	3	5.608E+007	13.63	0.0004	S	
	CaO. SiO_2	3.340E+007	1	3.340E+007	8.12	0.0147	S	
	CaO.TiO_2	8.891E+005	1	8.891E+005	0.22	0.6504	NS	
	CaO.Na_3AlF_6	1.426E+006	1	1.426E+006	0.35	0.5670	NS	
	SiO_2.TiO_2	1.340E+006	1	1.340E+006	0.33	0.5788	NS	
	SiO_2. Na_3AlF_6	8.911E+006	1	8.911E+006	2.17	0.1669	NS	
	TiO_2. Na_3AlF_6	3.237E+006	1	3.237E+006	0.79	0.3926	NS	
	CaO.TiO_2.Na_3AlF_6	5.509E+005	1	5.509E+005	0.13	0.7208	NS	
	SiO_2.TiO_2.Na_3AlF_6	3.496E+006	1	3.496E+006	0.85	0.3748	NS	
	CaO.Na_3AlF_6. (CaO-Na_3AlF_6)	3.672E+007	1	3.672E+007	8.92	0.0113	S	
	TiO_2.Na_3AlF_6. (TiO_2-Na_3AlF_6)	3.977E+006	1	3.977E+006	0.97	0.3450	NS	
	Residual	4.938E+007	12	4.115E+006				
	Cor Total	3.040E+008	25					
Thermal Conductivity	Model	4.788E-004	13	3.683E-005	3.19	0.0265	S	0.77
	Linear mixture	3.775E-005	3	1.258E-005	1.09	0.3909	NS	
	SiO_2.CaO	2.355E-005	1	2.355E-005	2.04	0.1788	NS	
	TiO_2.CaO	1.576E-004	1	1.576E-004	13.65	0.0031	S	
	Na_3AlF_6.CaO	3.230E-007	1	3.230E-007	0.028	0.8700	NS	
	TiO_2.SiO_2	5.468E-006	1	5.468E-006	0.47	0.5045	NS	
	Na_3AlF_6.SiO_2	1.215E-004	1	1.215E-004	10.52	0.0070	S	
	Na_3AlF_6.TiO_2	1.041E-004	1	1.041E-004	9.02	0.0110	S	

	SiO_2.TiO_2.CaO	3.219E-005	1	3.219E-005	2.79	0.1209	NS	
	SiO_2.Na_3AlF_6.CaO	4.321E-005	1	4.321E-005	3.74	0.0770	NS	
	CaO.SiO_2. (CaO- SiO_2)	1.013E-004	1	1.013E-004	8.77	0.0119	S	
	SiO_2.Na_3AlF_6. (SiO_2-Na_3AlF_6)	1.181E-004	1	1.181E-004	10.22	0.0077	S	
	Residual	1.386E-004	12	1.155E-005				
	Cor Total	6.174E-004	25					
Thermal Diffusivity	Model	5.584E-003	15	3.722E-004	5.74	0.0041	S	0.89
	Linear mixture	6.815E-004	3	2.272E-004	3.50	0.0573	NS	
	SiO_2.CaO	2.173E-003	1	2.173E-003	33.52	0.0002	S	
	TiO_2.CaO	2.088E-003	1	2.088E-003	32.20	0.0002	S	
	Na_3AlF_6.CaO	1.740E-004	1	1.740E-004	2.68	0.1324	NS	
	TiO_2.SiO_2	2.753E-003	1	2.753E-003	42.47	<0.0001	S	
	Na_3AlF_6 .SiO_2	2.082E-003	1	2.082E-003	32.12	0.0002	S	
	Na_3AlF_6 .TiO_2	1.306E-003	1	1.306E-003	20.15	0.0012	S	
	SiO_2.Na_3AlF_6.CaO	2.558E-004	1	2.558E-004	3.95	0.0751	NS	
	TiO_2.Na_3AlF_6.SiO_2	9.410E-004	1	9.410E-004	14.52	0.0034	S	
	CaO.TiO_2. (CaO- TiO_2)	1.540E-003	1	1.540E-003	23.76	0.0006	S	
	CaO.Na_3AlF_6. (CaO -Na_3AlF_6)	1.815E-003	1	1.815E-003	28.00	0.0004	S	
	SiO_2. Na_3AlF_6. (SiO_2-Na_3AlF_6)	2.397E-003	1	2.397E-003	36.97	0.0001	S	
	TiO_2.Na_3AlF_6. (TiO_2-Na_3AlF_6)	2.718E-003	1	2.718E-003	42.08	<0.0001	S	
	Residual	6.483E-004	10	6.483E-005				
	Cor Total	6.232E-003	25					
Specific heat	Model	0.14	19	7.309E-003	5.13	0.0256	S	0.94
	Linear mixture	0.016	3	5.238E-003	3.68	0.0819	NS	
	SiO_2.CaO	0.011	1	0.011	7.77	0.0317	S	
	TiO_2.CaO	0.012	1	0.012	8.29	0.0281	S	
	Na_3AlF_6.CaO	4.478E-004	1	4.478E-004	0.31	0.5953	NS	
	TiO_2.SiO_2	0.015	1	0.015	10.83	0.0166	S	
	Na_3AlF_6.SiO_2	0.012	1	0.012	8.76	0.0253	S	
	Na_3AlF_6.TiO_2	3.587E-003	1	3.587E-003	2.52	0.1636	NS	
	SiO_2.TiO_2.CaO	1.906E-003	1	1.906E-003	1.34	0.2913	NS	
	SiO_2.Na_3AlF_6.CaO	9.674E-003	1	9.674E-003	6.79	0.0403	S	
	TiO_2.Na_3AlF_6.CaO	2.622E-004	1	2.622E-004	0.18	0.6829	NS	
	TiO_2.Na_3AlF_6.SiO_2	0.011	1	0.011	7.82	0.0313	S	
	CaO.SiO_2. (CaO -SiO_2)	5.218E-003	1	5.218E-003	3.66	0.1041	NS	
	CaO.TiO_2. (CaO-TiO_2)	0.010	1	0.010	7.08	0.0374	S	
	CaO.Na_3AlF_6. (CaO-Na_3AlF_6)	0.025	1	0.025	17.44	0.0058	S	
	SiO_2.TiO_2. (SiO_2-TiO_2)	1.438E-003	1	1.438E-003	1.01	0.3538	NS	
	SiO_2.Na_3AlF_6. (SiO_2-Na_3AlF_6)	0.033	1	0.033	23.29	0.0029	S	
	TiO_2.Na_3AlF_6. (TiO_2- Na_3AlF_6)	0.024	1	0.024	16.81	0.0064	S	

	Residual	8.546E-003	6	1.424E-003				
	Cor Total	0.15	25					
Weight Loss	Model	2.69	13	0.21	4.79	0.0052	S	0.83
	Linear mixture	0.75	3	0.25	5.82	0.0108	S	
	SiO_2.CaO	0.021	1	0.021	0.48	0.5018	NS	
	TiO_2.CaO	0.13	1	0.13	2.98	0.1101	NS	
	Na_3AlF_6.CaO	0.094	1	0.094	2.19	0.1651	NS	
	TiO_2.SiO_2	0.42	1	0.42	9.70	0.0089	S	
	Na_3AlF_6.SiO_2	0.32	1	0.32	7.49	0.0180	S	
	Na_3AlF_6.TiO_2	0.62	1	0.62	14.42	0.0025	S	
	SiO_2.Na_3AlF_6.CaO	0.16	1	0.16	3.68	0.0792	NS	
	TiO_2.Na_3AlF_6.SiO_2	0.25	1	0.25	5.85	0.0324	S	
	CaO.TiO_2 (CaO- TiO_2)	0.98	1	0.98	22.67	0.0005	S	
	TiO_2. Na_3AlF_6 (TiO_2-Na_3AlF_6)	0.055	1	0.055	1.28	0.2808	NS	
	Residual	0.52	12	0.043				
	Cor Total	3.21	25					
Contact angle	Model	14089.88	9	1565.54	12.57	<0.0001	S	0.88
	Linear mixture	7326.07	3	2442.02	19.61	<0.0001	S	
	CaO.SiO_2	941.68	1	941.68	7.56	0.0142	S	
	CaO.TiO_2	70.61	1	70.61	0.57	0.4624	NS	
	CaO.Na_3AlF_6	1593.93	1	1593.93	12.80	0.0025	S	
	SiO_2.TiO_2	29.16	1	29.16	0.23	0.6350	NS	
	SiO_2.Na_3AlF_6	109.52	1	109.52	0.88	0.3623	NS	
	TiO_2.Na_3AlF_6	684.61	1	684.61	5.50	0.0323	S	
	Residual	1992.47	16	124.53				
	Cor Total	16082.36	25					
Spreading Area	Model	2.172E+007	13	1.671E+006	3.71	0.0148	S	
	Linear mixture	1.682E+008	3	2.757E+006	6.13	0.0090	S	
	CaO. SiO_2	6.129E+005	1	6.129E+005	1.36	0.2657	NS	
	CaO.TiO_2	4.576E+005	1	4.576E+005	1.02	0.3330	NS	
	CaO.Na_3AlF_6	6.923E+005	1	6.923E+005	1.54	0.2384	NS	
	SiO_2.TiO_2	3.171E+005	1	3.171E+005	0.71	0.4175	NS	
	SiO_2. Na_3AlF_6	42463.48	1	42463.48	0.094	0.7639	NS	
	TiO_2.Na_3AlF_6	7.672E+005	1	7.672E+005	1.71	0.2160	NS	
	CaO.SiO_2.TiO_2	9.783E+005	1	9.783E+005	2.18	0.1660	NS	
	CaO.TiO_2.Na_3AlF_6	7.596E+005	1	7.596E+005	1.69	0.2181	NS	
	CaO.SiO_2.Na_3AlF_6	404.28	1	404.28	8.989 E-004	0.9766	NS	
	SiO_2.TiO_2. Na_3AlF_6	16081.65	1	16081.65	0.036	0.8532	NS	
	Residual	5.397E+006	12	4.497E+005				
	Cor Total	2.712E+007	25					
Adhesion Energy	Model	0.34	13	0.026	4.22	0.0089	S	0.82
	Linear mixture	0.23	3	0.077	12.37	0.0006	S	
	CaO.SiO_2	1.437E-004	1	1.437E-004	0.023	0.8819	NS	
	CaO.TiO_2	8.018E-004	1	8.018E-004	0.13	0.7263	NS	
	CaO.Na_3AlF_6	4.684E-004	1	4.684E-004	0.075	0.7888	NS	
	SiO_2.TiO_2	6.615E-003	1	6.615E-003	1.06	0.3236	NS	
	SiO_2.Na_3AlF_6	6.290E-003	1	6.290E-003	1.01	0.3353	NS	

	$TiO_2.Na_3AlF_6$	1.006E-004	1	1.006E-004	0.016	0.9011	NS	
	$CaO.SiO_2.TiO_2$	1.612E-004	1	1.612E-004	0.026	0.8750	NS	
	$CaO.SiO_2.Na_3AlF_6$	1.442E-004	1	1.442E-004	0.023	0.8817	NS	
	$CaO.TiO_2.Na_3AlF_6$	4.678E-004	1	4.678E-004	0.075	0.7889	NS	
	$SiO_2.TiO_2.Na_3AlF_6$	0.013	1	0.013	2.03	0.1796	NS	
	Residual	0.075	12	6.243E-003				
	Cor Total	0.42	25					
Surface Tension	Model	7213.21	9	801.47	19015.28	<0.0001	S	0.99
	Linear mixture	7210.18	3	2403.39	57021.88	<0.0001	S	
	$CaO.SiO_2$	0.13	1	0.13	3.15	0.0948	NS	
	$CaO.TiO_2$	0.055	1	0.055	1.31	0.2686	NS	
	$CaO.Na_3AlF_6$	1.51	1	1.51	35.77	<0.0001	S	
	$SiO_2.TiO_2$	0.15	1	0.15	3.50	0.0799	NS	
	$SiO_2.Na_3AlF_6$	0.15	1	0.15	3.65	0.0741	NS	
	$TiO_2.Na_3AlF_6$	0.044	1	0.044	1.03	0.3247	NS	
	Residual	0.67	16	0.042				
	Cor Total	7213.88	25					

Note: S – Significant, NS – Not significant

Table 5.3 shows that the coefficients of R^2 for all properties are near unity, indicating a close match between the response model and experimental results with minimal variation. Figure 5.1 illustrates how predicted values differ from actual values for certain attributes.

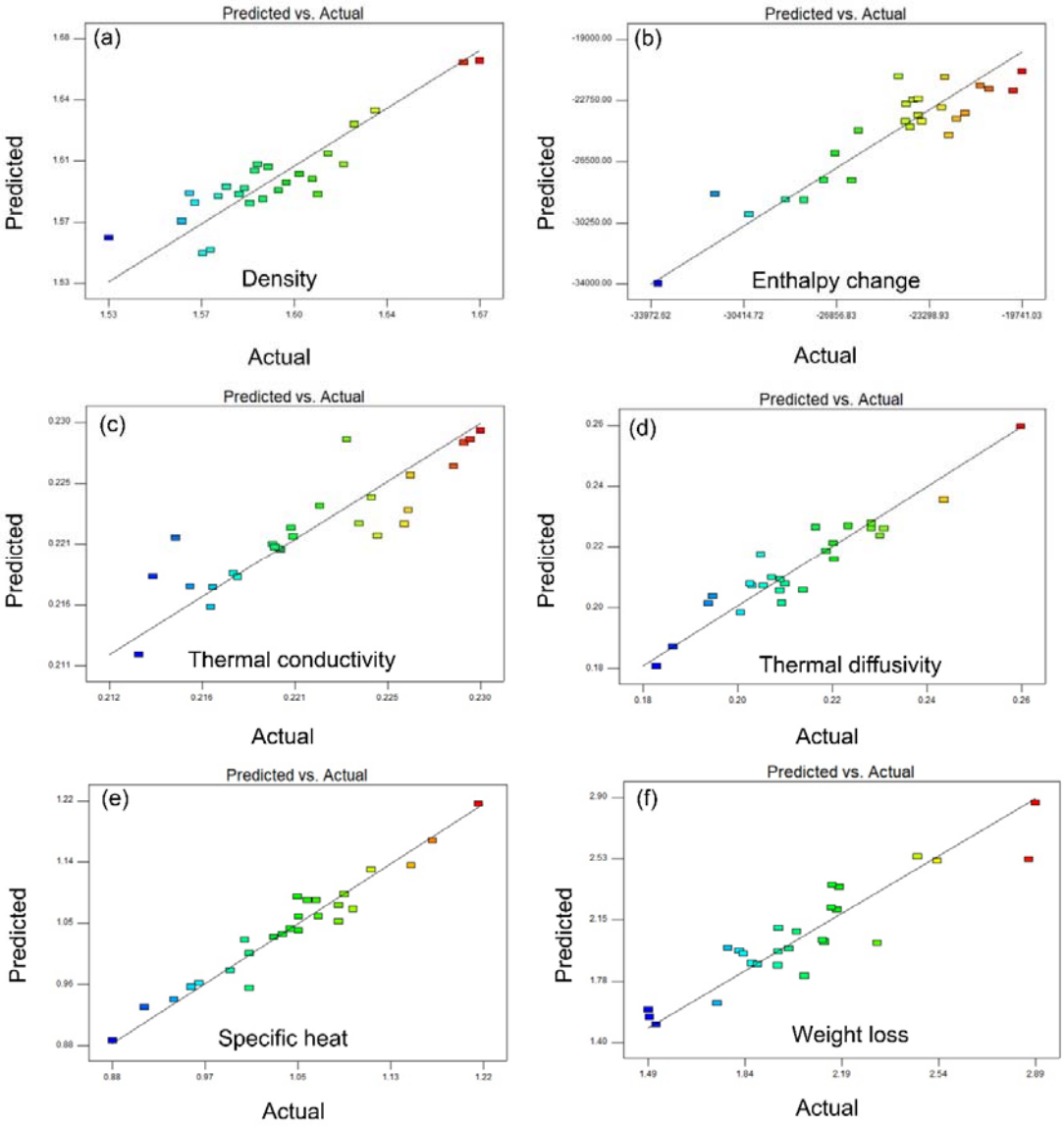
Predicted vs. Actual
(a)
Density
Predicted
Actual
Predicted vs. Actual
(b)
Enthalpy change
Predicted
Actual
Predicted vs. Actual
(c)
Thermal conductivity
Predicted
Actual
Predicted vs. Actual
(d)
Thermal diffusivity
Predicted
Actual
Predicted vs. Actual
(e)
Specific heat
Predicted
Actual
Predicted vs. Actual
(f)
Weight loss
Predicted
Actual

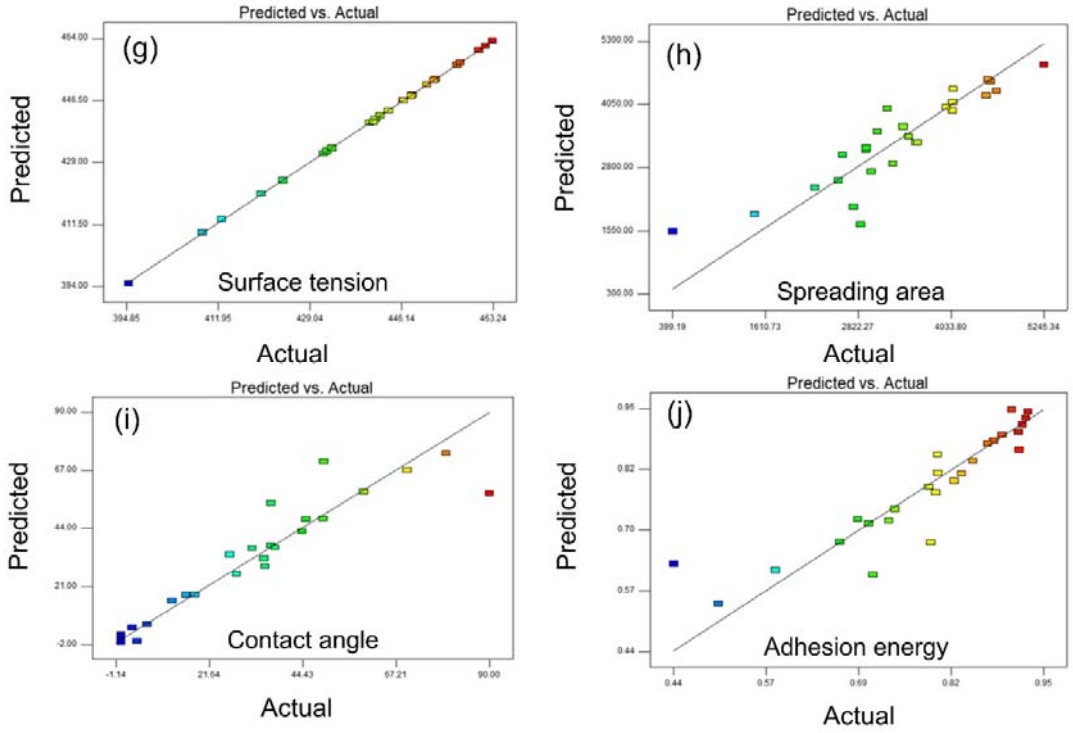

Figure 5.1: predicted vs. actual value plot of various properties

5.1.2 Effect of coating constituents and their interactions on various properties.

The developed regression model analysis shows that coating ingredients remarkably influence thermophysical and physicochemical properties. Several chemical reactions occur when the coating is exposed to the high-temperature range during welding. Obtaining better performance at a high temperature requires maintaining the coating properties, i.e., minimum weight loss, high thermal stability, high conductivity, appropriate enthalpy, suitable specific heat, and thermal diffusivity. During the fusion process, the coating composition melts, dissolves, and mixes with the liquid weld pool, filler wire, and base metal.

5.1.2.1 Density

Table 5.3 demonstrates that the developed density regression model is significant, with a p-value of 0.0105. Table 5.3 and Table A-1 show that each individual coating component significantly decreases density. $SiO_2.Na_3AlF_6$ is the only binary interaction that shows a significant and increasing effect on density. $CaO.TiO_2.Na_3AlF_6$ is the ternary mixture that shows a significant increase in density. The ternary combination of CaO, TiO_2, and Na_3AlF_6 improves slag detachability and weld cleanliness. Slag-metal reactions occur while welding using coated electrodes. Al_2O_3 and SiO_2 oxides are well-known network former, showing an increasing effect on the density of the molten slag. Increased oxide inclusions in welds can reduce fluidity and increase density by forming networks. During the welding process, a chemical reaction occurs, and CaO present in the coating dissociates into Ca^{2+} and O^{2-}ions. Further, O^{2-} ions react with SiO_2 present in electrode coating and form complex silicate ion SiO_4^{4-}. These complex tetrahedral structured silicate ions reduce the oxide inclusion, decreases fluidity and increases density. The restricted fluidity of the molten weld pool ensures a good density of coating composition. Cryolite reacts with silica present in the coating, and Al_2O_3 (slag) is formed, improving slag detachability and reducing diffusible hydrogen concentration. This enhances the weld quality (Burck et al., 1990; Fellner and Matiašovský, 1973). The important aspect of density is that it should not be too high since

this might lead to several weld defects. The regression model developed from the experimental results obtained from 2nd flux system and ANOVA were performed to check the adequacy of model as shown in Table A5. The developed regression model of density shows significance with a p-value of 0.0200, which is under the desirable confidence limit of 95%. The regression model (Tables A5 and A6) reported that the primary constituent has an increasing impact on the density parameter. It was also observed that ternary components contained silicon dioxide and strontium oxide $CaO.SiO_2.SrO$, $CaF_2.SiO_2.SrO$ has a significant and increasing impact, whereas other components show a decreasing effect on the density. The mixture components containing SiO_2 and SrO enhanced the slag detachability and tends to improve its other associated parameters. The presence of SrO in the flux coating helps in controlling the viscosity of the slag. Proper slag viscosity is important for easy slag removal and for producing a clean and smooth weld bead. Therefore, it improves the weld quality, stability, and mechanical properties.

5.1.2.2 Enthalpy change

A chemical reaction occurs during the welding process, and heat evolves (either released or absorbed), and the quantity of energy in the form of heat associated with the process is expressed by enthalpy. In the present experiment, enthalpy values of different coating mixtures show negative values, which means the nature of the reaction is exothermic. Another important aspect is that enthalpy should not have an excessively high negative value because it produces more heat and affects the base metal, weld metal, and heat-affected zone. Enthalpy regression analysis shows significance, having a p-value of 0.0054 (From Table 5.3 and Table A-1). It was evident that every individual and binary interaction of $SiO_2.CaO$ significantly affects change in enthalpy. The ternary mixture of $TiO_2.Na_3AlF_6.CaO$ and $TiO_2.Na_3AlF_6.SiO_2$ has an increasing effect on change in enthalpy, whereas other interactions show opposite effects on enthalpy. The values of change in enthalpy for all coating compositions are shown in Table 5.1. It was observed that a minimum change in enthalpy for coating 20, whereas maximum value coating 7. Figure 5.2 shows the graph of heat flow corresponding to temperature for some coating compositions. Thus, these plots estimated enthalpy change for each coating composition. The regression model developed for the 2nd flux coating system is shown in Table A5. A p-value of 0.0388 indicates that the enthalpy regression analysis is significant. Results suggest that it was affected significantly by the individual ingredients. Ternary mixture $CaO.CaF_2$. SrO, $CaO.SiO_2.SrO$, and $CaF_2.SiO_2.SrO$ is the most effective and has an increasing effect on enthalpy, while others negatively affect enthalpy (Table A5and A6). The values of enthalpy change for all coatings are shown in Table A3. The presence of SrO in the flux coatings influence the enthalpy change by enhancing thermal stability and participating in heat-absorbing and heat-releasing reactions.

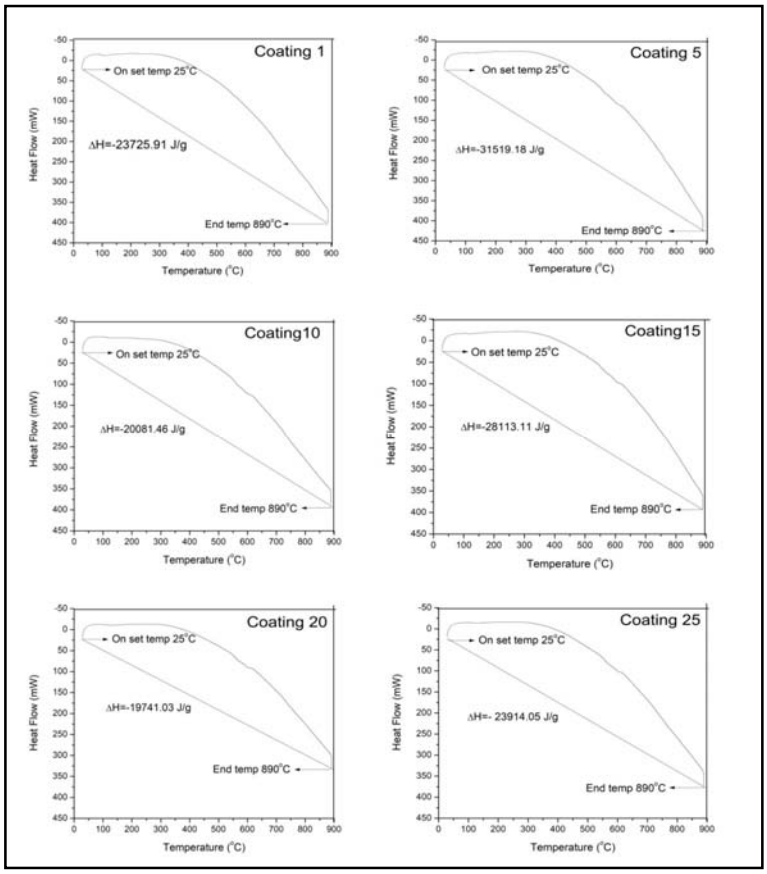

Figure. 5.2 Heat flow of various coatings composition

5.1.2.3 Weight loss

The thermal stability of flux coating component is essential to welding at high temperatures, ensuring better weld quality and weld performance. It might be affected if the flux constituents have thermal instability (Sharma and Chhibber, 2019). From Table 5.3 and Table A1, the developed regression analysis of weight loss reported that it was affected significantly by individual constituents while binary interaction of $CaO.SiO_2$, $SiO_2.TiO_2$, $SiO_2.Na_3AlF_6$, TiO_2. Na_3AlF_6 shows an increasing effect and increases thermal stability. Coating mixture 21 is the most thermally stable with the least weight loss, and coating mixture 11 is the least thermally stable with more weight loss because higher weight loss is due to the higher amount of CaO as it has the hygroscopic nature of electrode coatings. The hygroscopic nature leads to a decrease in the viscosity of the slag and increases the chances of contamination from air or moisture. Moisture has significant effects on the coating mixture containing basic oxides. CaF_2 lowers the hygroscopicity of CaO, as previously documented (Kanjilal et al., 2006). A higher amount of CaO results in higher weight loss, whereas the presence of acidic flux (TiO_2) influences thermal stability synergistically(Mahajan and Chhibber, 2019). Figure 5.3 shows the weight loss for some coating compositions. Plots show that flux coating weight decreases with increasing temperature. The thermal stability of flux coatings is demonstrated by weight loss with increasing temperature. The regression model developed for the 2nd flux coating system is shown in Table A5. From Table A5 and Table A6 show the regression analysis of weight loss is significant with a p-value of 0.0373 and affected significantly by the individual mixture. It was also observed that the ternary component of $CaO.CaF_2.SiO_2$, $CaO.CaF_2.SrO$, and $CaF_2.SiO_2.SrO$ enhanced the thermal stability of electrode coatings. The coating mixture 3 shows the least thermally stable with a higher percentage of weight loss because a higher amount of calcium oxide gives more weight losses due to its hygroscopic behavior. Weight

loss in the coating increases as the amount of basic oxide increases because of its hygroscopic nature, and it is more susceptible to contamination from moisture or air.

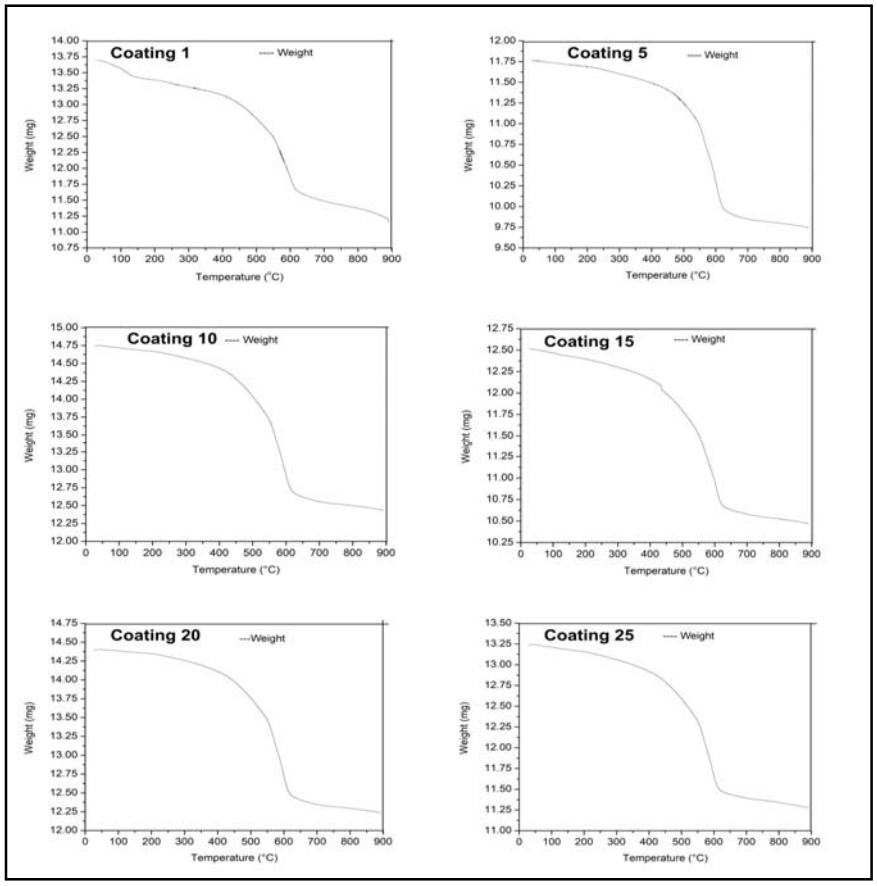

Figure. 5.3 Weight loss for coating compositions

5.1.2.4 Thermal properties

The regression analysis for thermal conductivity shows that individual constituents have no significant effect, while binary interaction of $CaO.SiO_2$, $CaO.Na_3AlF_6$, $SiO_2.TiO_2$, $SiO_2.Na_3AlF_6$ and ternary interaction of $CaO.SiO_2.TiO_2$ shows an increasing effect on conductivity (Table 5.3 and Table A1). The coating conductivity increases with the amount of silica because of the network chain formation of covalently bonded ions Si^{4+}. The nature of cations that exist in the mixture affects thermal conductivity significantly. It was observed from the previous literature (Kang et al., 2014; Kerstan et al., 2011; Mills, 2011) that thermal and physical properties were significantly affected by the non-bridging oxygen (NBO) that exists in the system. Alkaline ions play an important role in governing the thermophysical behavior, such as thermal conductivity, thermal diffusivity, thermal expansion, and density of alumina silicate-based glasses. Similarly, thermal diffusivity regression analysis shows significance, having a p-value of 0.0041, and reported that individually, CaO, SiO_2, TiO_2, binary mixture of $CaO.Na_3AlF_6$ and the ternary mixture of $CaO.SiO_2.Na_3AlF_6$,TiO_2. $Na_3AlF_6.SiO_2$ shows an increasing effect on thermal diffusivity (Table 5.3 and Table A1). The regression of specific heat shows significance, having a p-value of 0.0256. From this model analysis, no individual constituent significantly affects specific heat. $SiO_2.CaO$, $TiO_2.CaO$, $TiO_2.SiO_2$, $Na_3AlF_6.SiO_2$ binary mixture shows a significant and increasing effect on specific heat. The heat needed to raise the temperature of a unit quantity of coating mixture is called specific heat (SH). The electrode will need a lot of energy to melt and fuse; hence, the specific heat should be low. Conversely, low specific heat causes the temperature to rise rapidly from modest heat input, causing rapid temperature rise. Hence, it causes an exothermic reaction

that releases a large amount of heat and damages the weld. The regression model developed for the 2nd flux coating system is shown in Table A5. From Table A5 and A6 show regression analysis of thermal conductivity indicates that model is significance with a p-value of 0.0140, and results reported that individual constituents of fluorspar, strontium oxide, and binary mixture of CaO. SiO_2 has a significant and increasing impact on thermal conductivity. It was also observed that ternary components of $CaO.CaF_2.SiO_2$, $CaO.CaF_2.SrO$, and $CaF_2.SiO_2.SrO$ has an increasing effect on thermal conductivity. The thermal diffusivity regression analysis, which yielded a statistically significant p-value of 0.0239, revealed that primary constituents CaO, SiO_2, CaF_2, SrO, and binary constituents of CaO. SrO and the ternary components containing SrO and SiO_2 ($CaO.SiO_2.SrO$, $CaF_2.SiO_2.SrO$) have an increasing impact on the thermal diffusivity, whereas other components show decreasing impact on diffusivity. When it comes to coating compositions, the diffusion coefficient should be kept as low as possible because a high value of diffusion in the coating mixture indicates that the coatings mixture is not stable, resulting in poor thermo-physical properties. The specific heat regression model shows significance with a p-value of 0.0478. The results present for this model show that individually strontium oxide and the ternary components containing strontium oxide ($CaO.CaF_2.SrO$, $CaF_2.SiO_2.SrO$) show an increasing impact on specific heat. A high amount of energy is needed for an electrode to melt, hence keeping the lowest specific heat. The rapid rise in temperatures may be caused by an increase in specific heat, which allows the temperature to rise from low heat input.

5.1.2.5 Wetting properties

The developed regression model analysis shows that coating ingredients influence the wettability attributes significantly. Several chemical reactions influence the coating characteristic when the coating exhibits a high-temperature range during welding. The contact angle is essential for wettability measurement. It represents the degree of wetness on the solid-liquid interface. High wettability is associated with small contact angles, and low wettability with large contact angles. Welding requires optimum wetting properties. It ensures that flux shields the weld pool from contaminants and gases. The influence of coating composition components on wettability characteristics was studied using regression models and analyzed by ANOVA (Table 5.3 and Table A2). The regression analysis for contact angle reported the binary interaction of $CaO.SiO_2$, $CaO.Na_3AlF_6$, and $SiO_2.Na_3AlF_6$ has a significant and increasing effect, while the binary mixture $CaO.TiO_2$ and $TiO_2.Na_3AlF_6$ has shown a decreasing effect. Previous studies reported that the amount of free oxygen available governs the contact angle during high-temperature chemical reactions. The strongly basic oxides CaO and CaF_2 undergo a reduction reaction that provides free oxygen; as a result, the contact angle decreases as the concentration of these basic oxides increases (Mahajan and Chhibber, 2019).The strong network-forming capacity of silica (SiO_2) reduces the availability of free oxygen ions (O^{2-}) during reactions, which increases the interfacial tension and contact angle. Free oxygen ions are typically present on the solid/liquid interface (Joshi and Chhibber, 2018; Kim et al., 2018; Kingery and Humenik Jr, 1953; Liu et al., 2014) Lower contact angles enhanced wettability between the substrate and the coating mixture, which resulted in better spreadability. The coating mixture with a lower contact angle had the largest spreading area. Hence, the contact angle is inversely proportional to spreadability. The regression analysis for the spreading area reported that the binary interactions of $TiO_2.Na_3AlF_6$, $CaO.TiO_2$, and ternary interaction of $CaO.SiO_2$. Na_3AlF_6, $CaO.SiO_2.TiO_2$ has an increasing effect. Adding basic oxides reduces melt viscosity, resulting in a low contact angle and broad spreading area (Cruz-Crespo et al., 2010; Mahajan et al., 2020). Surface tension was calculated by a constituent mole fraction and surface tension factor (Hara and Ogino, 1989; Kim et al., 2018; Kucharík and Vasiljev, 2006; Liu et al., 2014; Nakamoto et al., 2007). The surface tension for different compositions was calculated and given in Table 5.1. The surface tension quadratic regression model is significantly under the

confidence limit (Table 5.3 and Table A2). It shows the individual constituent and the binary mixture of $CaO.Na_3AlF_6$ is significant and has an increasing effect on surface tension while binary interaction of $CaO.SiO_2$, $CaO.TiO_2$, and $SiO_2.TiO_2$ has a decreasing effect. Previous studies found that interfacial tension and contact angle were correlated. The chemical processes at the solid/liquid interface are due to electron sharing, leading to increased binding energies and strong chemical interactions. Because of its strong network-forming capacity, free oxygen (O^{2-}) is released when basic oxides such as CaO and CaF_2 dissociate. This free oxygen has the potential to change the complex network structures formed by SiO_2. The interfacial tension is raised because SiO_2 decreases the free oxygen ions. (Kim et al., 2018) found that raising the TiO_2/SiO_2 ratio raises surface tension while decreasing it when the SiO_2/Al_2O_3 ratio rises. The adhesion work is the amount of energy needed to remove the contacting material from the substrate. The regression model developed for adhesion energy suggests that binary interactions of $CaO.SiO_2$, $CaO.TiO_2$, and $CaO.Na_3AlF_6$, along with ternary interaction of $SiO_2.TiO_2$. Na_3AlF_6 has an increasing effect. The molten slag flow is enhanced as the contact angle lowers, while adhesion energy improves as the contact angle decreases. A decrease in the contact angle and an increase in adhesion energy result from the production of free oxygen ions during the dissociation of basic oxides. Weld bead smoothness is affected by viscosity and interfacial tension during welding processes. A convex bead is formed by high interfacial tension, whereas a concave bead is formed by low interfacial tension. Thus, the mineral fraction in the electrode coating significantly influences the physicochemical, thermophysical properties, and wettability characteristics. The regression model developed for 2nd system from the experimental results and shown in Table A5. From the Table A5 and A11 indicates that the regression model for contact angle is significance, with a p-value of 0.0481. It also observed that the binary mixture of CaO.SrO, CaF_2.SrO, and SiO_2.SrO shows an increasing effect significantly. From Table A4, it can be seen that coating composition having a lower contact angle corresponds to the higher spread area. The regression model of the spread area indicated that all the primary constituents significantly have an increasing effect. $CaO.CaF_2.SiO_2$ and $CaO.CaF_2$.SrO ternary interaction is the most effective and has an increasing impact on the spreading area. The model with a p-value of 0.0220 shows significance. The regression analysis of surface tension suggested that all primary constituent shows an increasing effect significantly. Binary interaction of $CaO.CaF_2$is the most effective and has an increasing impact on surface tension. $CaO.SiO_2$, CaO.SrO and $CaF_2.SiO_2$ binary mixture shows decreasing effect on surface tension. From the developed regression model, it was observed that all primary constituents, along with $CaO.CaF_2$.SrO, $CaO.SiO_2$.SrO, and $CaF_2.SiO_2$.SrO ternary mixture is the most favourable and has an increasing effect on adhesion energy. Binary interactions of $CaO.CaF_2$, $CaO.SiO_2$, and CaO.SrO show a decreasing effect. As the contact angle is smaller, the molten slag flow gets better. Hence the adhesion energy increases.

5.1.3 Contour plots for different properties

A contour plot is a graphical representation that displays the relationship between the response variable and different combinations of mixture components in a two-dimensional (2D) format. Contour plots indicate expected values of various properties responses for varying amounts of the coating mixture. The multiple colors in the contour curve indicate the different ranges of a particular output obtained. The variation in the coating composition of constant response value can also be represented by lines crossing the plot. The contour graph for different acquired properties can be shown in Figure 5.4. The plots clearly demonstrate the correlation between the electrode coating constituents and the variance in a certain property response.

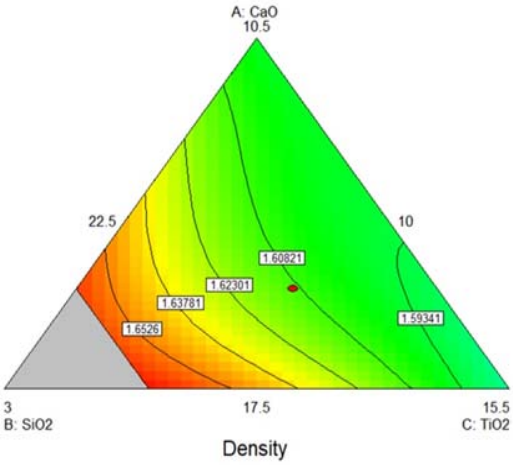

Density

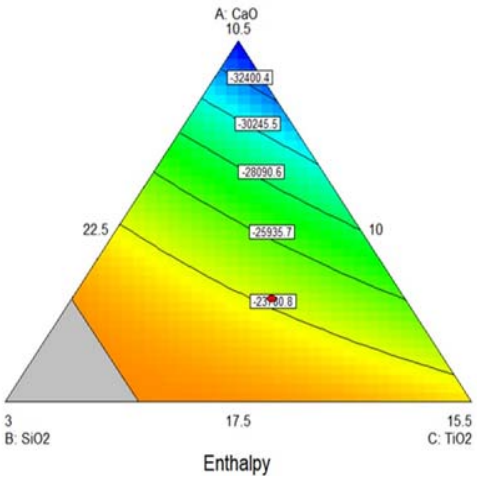

Enthalpy

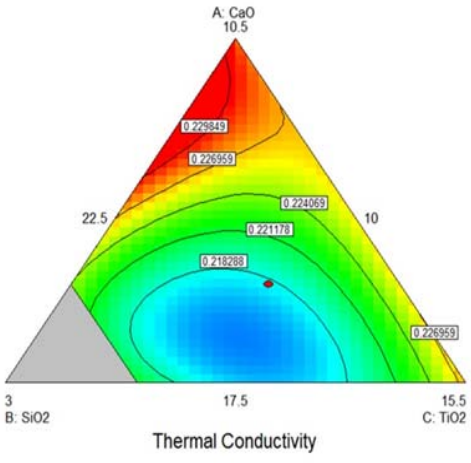

Thermal Conductivity

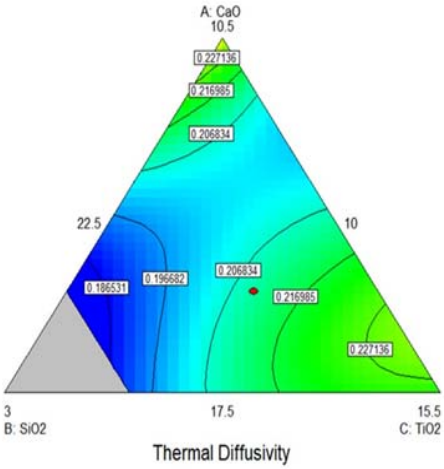

Thermal Diffusivity

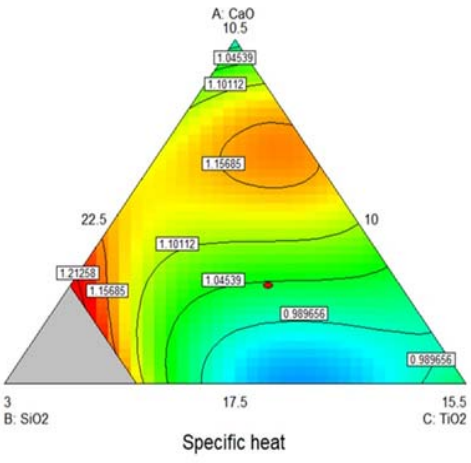

Specific heat

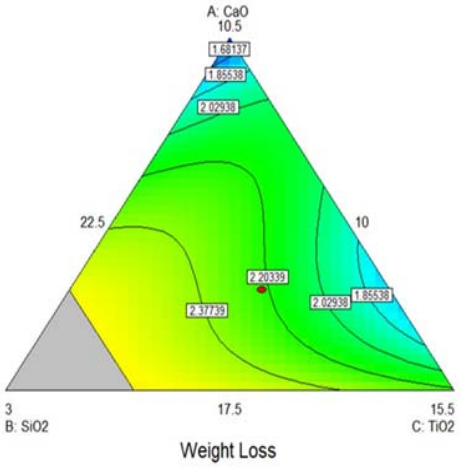

Weight Loss

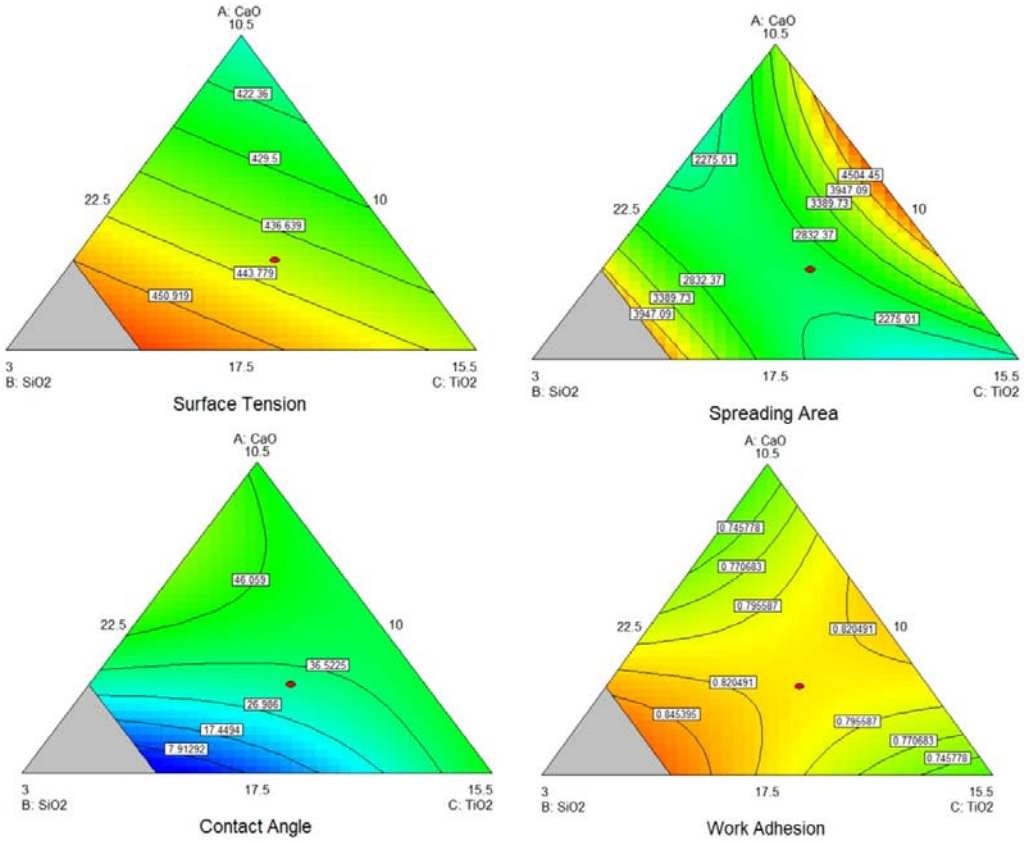

Figure. 5.4 Contour plots for different properties

5.1.4 Model Validation

The developed regression models validated the actual and predicted values by randomly choosing three coating compositions for confirmatory experiments. The model validation for error percentage and average error percentage for various physicochemical, thermophysical, and wettability properties are presented in Table 5.4 -Table 5.7. The average error percentage for all the responses is under the limit, which validates the model.

Table 5.4: Error percent (%) for density, weight loss, and enthalpy change

Mixture				Predicted Value			Actual Value			Error (%)		
CaO	SiO_2	TiO_2	Na_3AlF_6	ρ	ΔW	ΔH	ρ	ΔW	ΔH	ρ	ΔW	ΔH
15.00	10.00	20.00	25.00	1.596	1.833	26994.10	1.635	1.887	25888.20	2.39	2.87	4.27
14.50	10.00	19.00	26.50	1.595	1.865	27586.30	1.631	1.775	26262.20	2.19	5.06	5.04
14.00	08.00	22.00	26.00	1.623	2.213	25394.10	1.662	2.118	24301.40	2.34	4.47	4.50
									Avg % Error	**2.31**	**4.13**	**4.60**

Table 5.5: Error percent (%) for thermal conductivity, diffusivity, and specific heat

Mixture				Predicted Value			Actual Value			Error (%)		
CaO	SiO_2	TiO_2	Na_3AlF_6	TC	TD	SH	TC	TD	SH	TC	TD	SH
15.00	10.00	20.00	25.00	0.2248	0.1631	1.323	0.2294	0.1718	1.273	1.99	5.05	3.92
14.50	10.00	19.00	26.50	0.2262	0.1983	1.162	0.2305	0.2012	1.190	1.85	1.43	2.31
14.00	08.00	22.00	26.00	0.2283	0.1748	1.280	0.2299	0.1828	1.199	0.71	4.36	6.83
									Avg% Error	**1.52**	**3.61**	**4.35**

Table 5.6- Error percent (%) for contact angle and surface tension

Mixture				Predicted Value		Actual Value		Error (%)	
CaO	SiO_2	TiO_2	Na_3AlF_6	ST	CA	ST	CA	ST	CA
15.00	10.00	20.00	25.00	437.258	31.53	437.449	30.67	0.0436	2.80
14.50	10.00	19.00	26.50	431.449	37.19	431.668	35.51	0.0507	4.73
14.00	08.00	22.00	26.00	437.544	47.88	437.858	45.62	0.0717	4.95
							Avg % Error	**0.0553**	**4.16**

Table 5.7: Error percent (%) for adhesion energy and spreading area

Mixture				Predicted Value		Actual Value		Error (%)	
CaO	SiO_2	TiO_2	Na_3AlF_6	AE	SA	AE	SA	AE	SA
15.00	10.00	20.00	25.00	0.8677	4912.89	0.8134	4996.25	6.6756	1.668
14.50	10.00	19.00	26.50	0.8425	4948.22	0.7831	4745.23	7.5852	4.277
14.00	08.00	22.00	26.00	0.7814	2439.21	0.7442	2495.63	4.9986	2.261
							Avg % Error	**6.4198**	**2.735**

Note: ρ= Density, ΔH = Change in enthalpy, TC= Thermal conductivity, ΔW = Weight loss TD = Thermal diffusivity, ST = Surface tension , SH = Specific heat, CA = contact angle, AE =Adhesion energy , SA= Spreading area

5.2 Structural examination of electrode coatings

The structural behavior of the coating compositions was analyzed using X-ray diffraction (XRD) and Fourier transformation infrared spectroscopy (FTIR) techniques. Here, the prominent phases identified using XRD were $CaCO_3$, TiO_2, SiO_2, CaF_2, and Na_3AlF_6. Also, Ti is found to bond with [O] in different molar ratios. Separate peaks corresponding to TiO_2 and Ti_8O_{15} were found in the XRD plots. Due to similar constituent minerals, the peaks were almost similar in nature, corresponding to the same phases for all the coating compositions. Almost the same phases were observed for all the coatings. Figure 5.5 shows a representative X-ray diffraction plot for some coating compositions. FTIR analysis helps identify the bond's nature between the elements present in the mixture. The type of bonds present between different elements affects the thermophysical and physicochemical properties of the electrode coating mixture. Due to the network-forming nature of silicate ion (SiO_4^{4-}), this will improve the thermal conductivity of the coating mixtures, and the

concentration of these anions depends upon the non-bridging oxygen available. So, different bonds were analyzed using their respective bond position from the IR spectra. Previous researchers studied the nature of different bonds corresponding to various peaks (Garai et al., 2015, 2014; Kaur et al., 2011; Sowmya and Sankaranarayanan, 2004). Various peaks were seen in the entire range of wave number span, as shown in Figure 5.6. A peak in the approximate range of 450-500 cm^{-1} represents [Si-O] bond stretching. XRD results have indicated the presence of compounds of Ti and O in different molar ratios. This is further verified by a peak in the range of 700-750 cm^{-1} which corresponds to Titanyl (Ti-O) group vibration. A peak in the 750-800 cm^{-1} approximate range exhibits Si-OH stretching vibrations in the coating composition. The asymmetric Si-O vibration mode has a peak range of approximately 1000-1250 cm^{-1}. It is due to the formation of non-bridging oxygen (NBO). Non-bridging oxygen increases with the different network-forming elements and stabilizes the network structure. The 1250-1500 cm^{-1} range peak shows anti-asymmetric Si-O vibration caused by the complex SiO_4^{-4} ion. Silicate anion (SiO_4^{4-}) binds together with the network modifiers such as K^+, Li^{2+}, $Al^{3+}$and Ti^{3+} by the electrostatic force of attraction and develops an ionic bridge between two types of non-bridging oxygen. Small peaks in the range of 1500-1750 cm^{-1} and 3500-3750 cm^{-1} wavenumber reflect H-OH bonding and OH vibration mode, which is mainly due to some moisture content in the pellets.

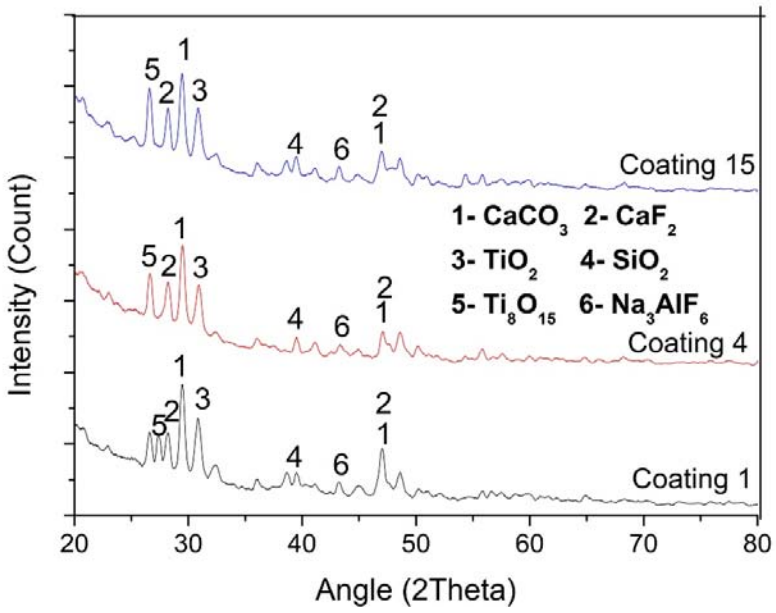

Figure. 5.5 XRD plot of the coating composition

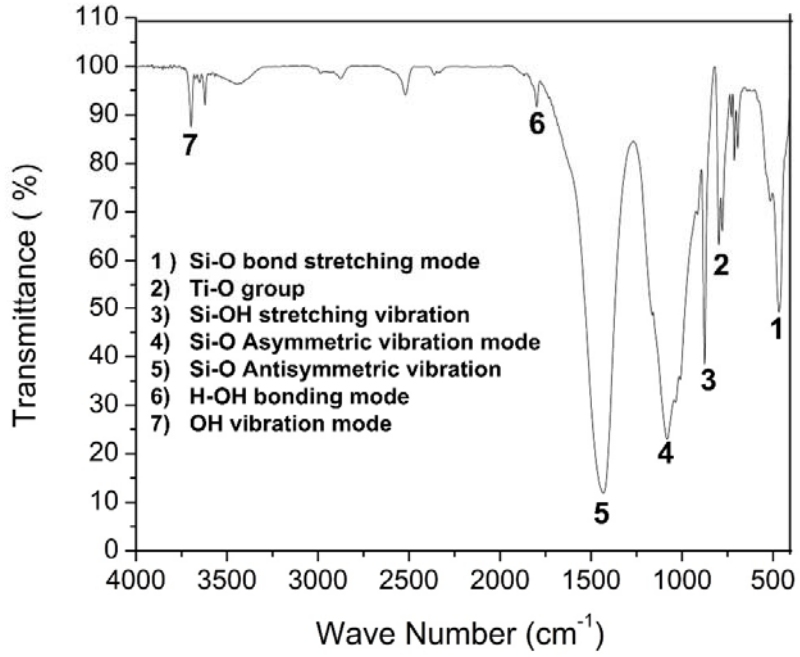

Figure. 5.6 FTIR curves of the coating composition

5.3 Multipass bead on plate analysis

Twenty-six laboratory-developed electrodes were used to deposit weld beads onto a low alloy steel plate. The process of depositing the multi-pass weld beads was accompanied by visual inspections. Slag detachability, smoke reduction, arc stability, and weld quality were improved by coating formulations containing more silica, calcinated bauxite, and cryolite. The behavior of each electrode coating was investigated by recording qualitative observations for all the weld beads. Multi-pass weld beads of some electrode coatings were deposited on 100mm x 30mm x 6 mm low alloy steel plates, as shown in Figure 5.7. Table 5.8 shows the qualitative observations of deposited beads. To determine slag detachability, the base plate was hammered three times after weld beads were deposited. Table 5.9 presents the microhardness values and chemical composition data for all of the deposited welds. Welding fluxes containing rutile are said to have better slag detachability than those containing fluorites (Bhandari et al., 2019; Jindal et al., 2013b). On the other hand, there is evidence that cryolite enhances the slag detachability and weld cleanliness in nickel wire-based electrodes operating in basic flux systems (Qin and He, 2013; Sham and Liu, 2014; Wang and He, 2016). The mechanical behavior of deposited welds was assessed using microhardness testing. The main alloying elements were identified in each deposited weld, as shown in Table 5.9. Among the several alloying elements, nickel and chromium are particularly important for use in high-temperature conditions due to their improved mechanical properties and resistance to corrosion in harsh environments. The slag detachability, bead appearance, and weld quality are all improved in welds produced with electrodes E-6 and E-10. These deposited welds were smoke-free and had no porosity compared to other laboratory-developed electrodes.

Table 5.8 shows the qualitative observations of deposited weld beads

Coating	Slag detachability	Bead Performance	Arc Stability	Porosity
C1	Good	Good	Satisfactory	Yes
C2	Good	Good	Satisfactory	No
C3	Good	Good	Good	No
C4	Satisfactory	Poor	Poor	Yes
C5	Good	Good	Satisfactory	No
C6	V. Good	V.Good	V.Good	No
C7	Satisfactory	Satisfactory	Poor	Yes
C8	Satisfactory	Satisfactory	Satisfactory	No
C9	Good	Good	Satisfactory	No
C10	V.Good	V.Good	V.Good	No
C11	Poor	Satisfactory	Satisfactory	Yes
C12	Good	Satisfactory	Satisfactory	No
C13	V.Good	Satisfactory	V.Good	No
C14	Satisfactory	Poor	Poor	No
C15	Satisfactory	Satisfactory	Poor	Yes
C16	Poor	Satisfactory	Satisfactory	No
C17	Satisfactory	Satisfactory	Poor	Yes
C18	Satisfactory	Good	Good	No
C19	Good	Good	Satisfactory	No
C20	Satisfactory	Satisfactory	Satisfactory	No
C21	Good	Satisfactory	Poor	No
C22	Good	Good	Satisfactory	No
C23	Satisfactory	Satisfactory	Good	No
C24	Poor	Good	Good	No
C25	Poor	Satisfactory	Satisfactory	Yes
C26	Poor	Satisfactory	Poor	Yes

Table 5.9 Chemical composition of weld beads and microhardness value

Bead no	Chromium (Cr)	Iron (Fe)	Nickel (Ni)	Molybdenum (Mo)	Cobalt (Co)	Microhardness (MH)
C1	19.11	7.81	54.81	7.09	10.59	267
C2	20.32	3.85	53.21	8.88	11.62	323
C3	19.48	4.72	53.20	8.81	11.28	280
C4	20.13	3.65	53.25	8.89	11.25	253
C5	19.67	3.68	53.31	9.01	11.49	253
C6	20.53	2.71	53.28	8.04	11.54	272
C7	20.22	3.02	53.23	8.96	10.71	240
C8	20.62	4.63	53.52	8.68	10.77	257
C9	19.54	6.22	53.90	8.69	10.75	228
C10	19.81	7.53	53.74	8.66	10.74	241
C11	19.93	3.79	53.67	8.76	11.12	225
C12	19.45	4.20	53.11	9.13	11.32	244

C13	20.72	5.64	53.13	8.84	10.06	251
C14	20.65	5.59	53.18	9.12	11.02	260
C15	20.42	5.61	53.66	9.15	10.78	240
C16	19.52	3.91	53.25	8.78	10.65	275
C17	19.88	4.52	53.69	8.91	11.15	245
C18	19.63	4.66	53.70	8.98	11.09	262
C19	19.30	2.15	53.74	8.62	10.67	282
C20	20.22	5.21	53.78	8.56	10.57	244
C21	19.79	6.66	53.81	9.05	11.58	270
C22	19.69	3.84	53.84	8.09	11.35	221
C23	20.27	3.32	53.36	8.11	11.14	271
C24	19.03	3.98	53.07	9.13	11.07	250
C25	20.24	4.27	52.98	9.07	10.51	230
C26	20.46	5.66	53.33	8.76	11.04	235

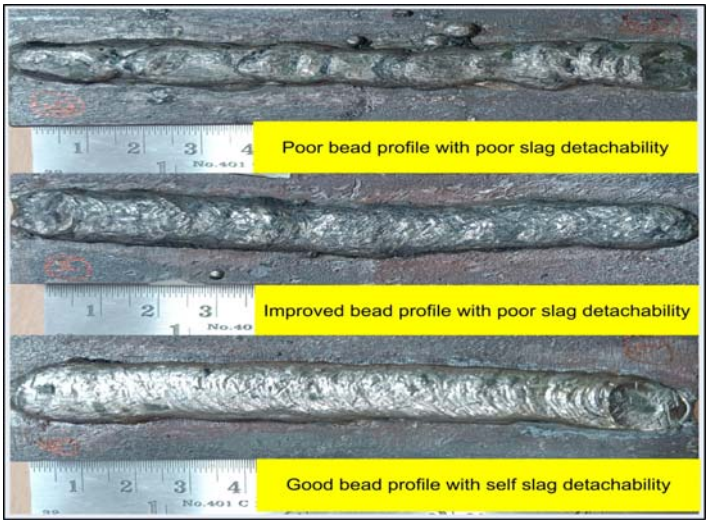

Figure. 5.7 Weld deposits on the base plate using SMAW bead 9, bead 19, and bead 6

5.4 Developing regression models to analyze weld chemistry and microhardness of deposited weld beads

The deposited weld beads were identified for weld chemistry and microhardness. The results are summarised in Table 5.9. The developed regression models are analyzed using linear, quadratic, cubic, and special cubic parameters based on the percentage of electrode coating compositions, individual constituents, and their binary and ternary interaction, as shown in Eq. 5.11- Eq.5.16. The analysis of the regression model is presented in Table 5.10.

Chromium (Cr) = 0.567503851 x A +15.96691083 x B -7.060869181 x C -1.902592314 x D-1.059838402 x A x B +0.36567282 x A x C +0.09275092 x A x D +0.096834062 x B x C-0.315127287 x B x D +0.326096628 x C x D +0.00700659 x A x B x C +0.026790805 x A x B x D -0.015461188 x A x C x D -0.010736595 x B x C x D Eq. **(5.11)**

Iron (Fe) =-37.4451xA-16.14522xB+13.239234xC-16.55901x D+2.8806951xAxB+0.3372403xA xC+1.9495456xAxD-1.684132xBxC+1.6783742xBxD+0.1324118xCxD+0.0501748xAxBxC-0.144831xAxBxD-0.031435 x A x C x D +0.0181476 x B x C x D Eq. **(5.12)**

Nickel (Ni) =-16.01614xA-9.868154xB+4.194244xC-5.685622x D+1.399487xAxB+0.240259x A x C +0.762511 x A x D -0.558342 x B x C +0.623631 x B x D +0.065135 x C x D +0.008664 x A x B x C -0.05466 x A x B x D -0.010807 x A x C x D +0.013242 x B x C x D Eq. **(5.13)**

Molybdenum (Mo)= 4.005948795 x A +8.099402989 x B -12.21820627 x C -0.126818583 x D -1.201567634 x A x B +0.469089479 x A x C -0.142945112 x A x D +0.705636886 x B x C-0.330481283 x B x D +0.406356998 x C x D -0.004451273 x A x B x C +0.044449063 x A x B x D -0.014253206 x A x C x D -0.019912923 x B x C x D Eq. **(5.14)**

Cobalt (Co) = 18.15001xA-9.397128xB+1.6276883xC+2.7693479xD-0.544508xAxB-0.681063 x AxC-0.648476xAxD +0.702098xBxC+0.3269311 x B x D -0.096325 x C x D +0.002977 x A x B x C +0.0146185 x A x B x D +0.0210922 x A x C x D -0.027312 x B x C x D Eq. **(5.15)**

Microhardness (MH)= -345.9026255 x A -1132.2055 x B -822.1519766 x C -441.7786351 x D +11.85781994 x A x B +34.06707924 x A x C +20.76543209 x A x D +73.97581411 x B x C+45.50847376 x B x D +37.83921615xC x D -0.720084369 x A x B x C +0.00714688 x A x B x D -0.978252822 x A x C x D -2.230728243 x B x C x D Eq. **(5.16)**

Table 5.10 Regression model equation using ANOVA analysis for different properties

Property	Origin	SOS	df	MS	F value	P Value	Significance	R^2 Value
Cr	Model	4.9916	13	0.384	4.818	0.0051	Significant	0.84
	Linear mixture	1.9711	3	0.657	8.244	0.003		
	AB	0.5769	1	0.5769	7.239	0.0197		
	AC	0.0557	1	0.0557	0.699	0.4194		
	AD	0.0063	1	0.0063	0.079	0.7836		
	BC	0.006	1	0.006	0.075	0.7885		
	BD	0.0942	1	0.0942	1.181	0.2984		
	CD	0.1286	1	0.1286	1.613	0.2281		
	ABC	0.0377	1	0.0377	0.474	0.5044		
	ABD	0.5519	1	0.5519	6.925	0.0219		
	ACD	0.0877	1	0.0877	1.1	0.3149		
	BCD	0.092	1	0.092	1.154	0.3038		
	Residual	0.9564	12	0.0797				
	Cor Total	5.9479	25					
Fe	Model	44.159	13	3.3968	9.005	0.0003	Significant	0.91
	Linear mixture	2.1142	3	0.7047	1.868	0.1888		
	AB	4.2622	1	4.2622	11.3	0.0057		
	AC	0.0474	1	0.0474	0.126	0.7291		
	AD	2.7771	1	2.7771	7.362	0.0188		
	BC	1.8142	1	1.8142	4.809	0.0487		
	BD	2.671	1	2.671	7.081	0.0208		
	CD	0.0212	1	0.0212	0.056	0.8166		
	ABC	1.9357	1	1.9357	5.131	0.0428		
	ABD	16.129	1	16.129	42.76	< 0.0001		
	ACD	0.3625	1	0.3625	0.961	0.3463		
	BCD	0.2628	1	0.2628	0.697	0.4202		

	Residual	4.5267	12	0.3772				
	Cor Total	48.686	25					
Ni	Model	3.1201	13	0.24	4.489	0.0069	Significant	0.83
	Linear mixture	0.1076	3	0.0359	0.671	0.586		
	AB	1.0059	1	1.0059	18.81	0.001		
	AC	0.0241	1	0.0241	0.45	0.5151		
	AD	0.4248	1	0.4248	7.945	0.0155		
	BC	0.1994	1	0.1994	3.729	0.0774		
	BD	0.3688	1	0.3688	6.897	0.0221		
	CD	0.0051	1	0.0051	0.096	0.7621		
	ABC	0.0577	1	0.0577	1.079	0.3193		
	ABD	2.2973	1	2.2973	42.96	< 0.0001		
	ACD	0.0428	1	0.0428	0.801	0.3883		
	BCD	0.14	1	0.14	2.617	0.1317		
	Residual	0.6416	12	0.0535				
	Cor Total		25					
Mo	Model	4.5997	13	0.3538	0.354	0.0007	Significant	0.89
	Linear mixture	0.5478	3	0.1826	0.183	0.039		
	AB	0.7415	1	0.7415	0.742	0.0019		
	AC	0.0917	1	0.0917	0.092	0.1906		
	AD	0.0149	1	0.0149	0.015	0.586		
	BC	0.3185	1	0.3185	0.318	0.0239		
	BD	0.1036	1	0.1036	0.104	0.1662		
	CD	0.1996	1	0.1996	0.2	0.0633		
	ABC	0.0152	1	0.0152	0.015	0.5822		
	ABD	1.5192	1	1.5192	1.519	0.0001		
	ACD	0.0745	1	0.0745	0.075	0.235		
	BCD	0.3165	1	0.3165	0.316	0.0242		
	Residual	0.572	12	0.0477	0.048			
	Cor Total	5.1716	25					
Co	Model	3.2484	13	0.2499	6.459	0.0014	Significant	0.87
	Linear mixture	0.377	3	0.1257	3.249	0.06		
	AB	0.1523	1	0.1523	3.936	0.0706		
	AC	0.1933	1	0.1933	4.997	0.0452		
	AD	0.3073	1	0.3073	7.943	0.0155		
	BC	0.3153	1	0.3153	8.151	0.0145		
	BD	0.1013	1	0.1013	2.62	0.1315		
	CD	0.0112	1	0.0112	0.29	0.6001		
	ABC	0.0068	1	0.0068	0.176	0.6821		
	ABD	0.1643	1	0.1643	4.248	0.0617		
	ACD	0.1632	1	0.1632	4.219	0.0624		

	BCD	0.5954	1	0.5954	15.39	0.002		
	Residual	0.4642	12	0.0387				
	Cor Total	3.7126	25					
MH	Model	10012	13	770.19	4.094	0.0101	Significant	0.82
	Linear mixture	2761.4	3	920.46	4.893	0.019		
	AB	72.218	1	72.218	0.384	0.5471		
	AC	483.69	1	483.69	2.571	0.1348		
	AD	315.06	1	315.06	1.675	0.22		
	BC	3500.4	1	3500.4	18.61	0.001		
	BD	1963.7	1	1963.7	10.44	0.0072		
	CD	1731	1	1731	9.202	0.0104		
	ABC	398.7	1	398.7	2.119	0.1711		
	ABD	0.0393	1	0.0393	2E-04	0.9887		
	ACD	351.06	1	351.06	1.866	0.197		
	BCD	3971.6	1	3971.6	21.11	0.0006		
	Residual	2257.3	12	188.11				
	Cor Total	12270	25					

Note: - A- CaO, B- SiO_2, C- TiO_2, D-Na_3AlF_6

Table 5.10 shows that the values of R^2 for all properties are near unity, indicating a close match between the response model and experimental results with minimal variation. Figure 5.8 illustrates the predicted and actual values variations for certain attributes.

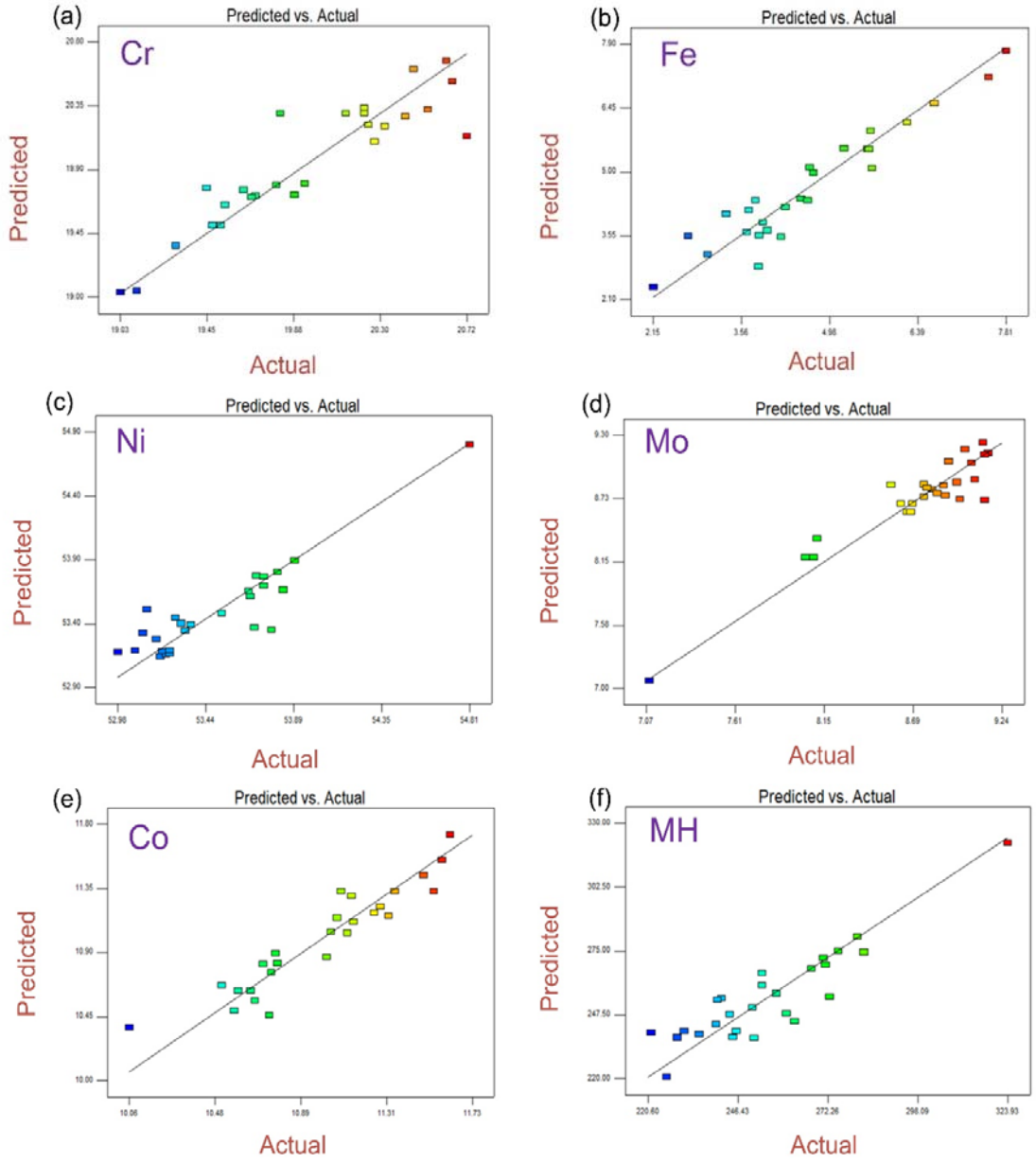

Figure 5.8: Plot of predicted vs. actual value for different welds

5.5 Effect of coating constituents and their interactions on microhardness and weld bead chemistry

5.5.1 Effect of flux compositions on nickel content

Eq 5.13 depicts the regression model used to predict the weight percentage change in nickel content. It was reported that mixture composition significantly affects the variation in nickel content. The flux composition variation has resulted in a variation in the nickel contents from 52.98 to 54.81. From Table 5.9, the maximum loss of nickel content is in bead C25, while the minimum loss is in bead C1. The trace plot is shown in Figure. 5.9 (c) indicates that an increase in TiO_2 in the reference blend leads to a loss of Ni content, whereas an increase in SiO_2 does not have much impact on nickel content. The increase of CaO and Na_3AlF_6 has shown increasing and decreasing behavior on nickel content. The binary interaction of $CaO.SiO_2$, $CaO.Na_3AlF_6$, and $SiO_2.Na_3AlF_6$ has shown a significant and increasing effect on the weld metal nickel. The ternary interaction of $CaO.SiO_2.TiO_2$ and

$SiO_2.TiO_2.Na_3AlF_6$ has a positive effect on nickel. The ternary interaction of $CaO.SiO_2.Na_3AlF_6$ shows the opposite effect on nickel content. During welding, the study of the impact of electrochemical reactions on the weld metal's chemical composition is crucial. The slag-weld and electrode-tip-molten pool interfaces could be where the electrochemical process starts. This study employed electrodes with a positive polarity to produce a direct current with a positive polarity. The extent of these effects, which significantly impact the chemical composition of the weld metal, depends on the slag's ion-to-electron ratio. The resulting electrochemical processes can be easily understood when liquid slag contacts molten metal. The oxidation of the alloy and the release and uptake of oxygen anions from the slag are all examples of possible anodic processes.

$$M(metal) + nO^{2-}(slag) = MO_n(slag) + 2ne^- \quad \text{Eq. (5.17)}$$

Where the M represents the alloying element present at either the electrode tip/slag or the weld pool/slag interface. Therefore, it is anticipated that there will be significant oxidation losses of alloy elements and oxygen adsorption at the anode (Kim et al., 1990).

5.1.2 Effect of flux compositions on chromium content

The regression model to predict change in chromium weight % is shown in Eq. 5.11. It was observed that mixture composition significantly affects the variation in chromium content. In the trace plot shown in Figure. 5.9 (a), it is observed that TiO_2 and Na_3AlF_6 both have a positive impact on chromium transfer. An increase in CaO has a decreasing effect on chromium content. The increase in SiO_2 has a decreasing effect on chromium transfer up to the reference blend, and then it starts increasing. It has been shown that the binary interaction of $CaO.TiO_2$, $CaO.Na_3AlF_6$, and $SiO_2.TiO_2$ increases chromium transfer. On the other hand, the binary interaction of $SiO_2.Na_3AlF_6$ decreases Cr content. The ternary interaction of $CaO.SiO_2.TiO_2$ and $CaO.SiO_2.Na_3AlF_6$ has a positive influence on chromium content. The ternary interaction of $CaO.TiO_2.Na_3AlF_6$ show a decreasing effect on chromium content in the BOP welds. The flux composition variation has resulted in a variation in the chromium contents in the multipass bead on plate welds from 19.03 to 20.72. Cr and Ni are the main elements in nickel welds, improving their strength and resistance to high-temperature corrosion. The presence of chromium enhances corrosion resistance. It is preferable to recoup the highest concentration possible through multi-pass weld deposits. The amount of chromium in the welds was measured, and it was found to be significantly less than in the filler metal. The dissociation of SiO_2 provides oxygen, which is a significant factor. Chromium is oxidized to chromium oxide when SiO_2 is dissociated, releasing oxygen (Maalekian, 2007). Eq. 5.17, which explains how anodic oxidation reactions lead to the loss of chromium content, provides an explanation.

5.1.3 Effect of flux compositions on molybdenum content

The developed regression model predicts the weight % of molybdenum, which is depicted by Eq.5.14. The compositional variation of flux has resulted in a variation of Mo from 7.09 to 9.15. The trace plot in Figure 5.9 (d) shows the increase in SiO_2 in the reference blend leads to a decrease in Mo content in welds, whereas the increase of TiO_2 is more favorable for the gain of Mo up to the reference blend and then starts decreasing. The increase in CaO and Na_3AlF_6 has a decreasing effect on molybdenum transfer up to the reference blend, and then it starts increasing. Because of their strong affinity for oxygen, molybdenum alloys are susceptible to forming oxides and non-metallic inclusions, which alter the alloy's mechanical and microstructural properties. When molybdenum is added, it mainly improves their corrosion and wear resistance (Liu et al., 2019). Bead C1 has shown maximum molybdenum loss, whereas Bead C15 has shown minimum molybdenum loss. The molybdenum loss can be explained by Eq. 5.17, which occurs due to anodic oxidation reactions. The binary interaction of $CaO.TiO_2$, $SiO_2.TiO_2$, and $TiO_2.Na_3AlF_6$ has shown an increasing impact on the molybdenum transfer, whereas the $CaO.SiO_2$ binary interaction has

a decreasing effect on Mo content. The interaction of $CaO.SiO_2.Na_3AlF_6$ has positive effects on molybdenum. The ternary interaction of $CaO.SiO_2.TiO_2$ and $CaO.TiO_2.Na_3AlF_6$ shows a negative effect on molybdenum transfer in the BOP welds.

5.1.4 Effect of flux compositions on Iron and cobalt content

The developed regression model predicts the weight percentage of iron and cobalt, as shown in Eq. 5.12 and Eq. 5.15. It was reported that mixture composition significantly affects the iron and cobalt content variation. The flux composition variation has resulted in a variation in the iron content from 2.71 to 7.81 and the cobalt content from 10.06 to 11.62. Based on the iron regression model that was created, it was found that the binary interaction of $CaO.SiO_2$, $CaO.TiO_2$, and $CaO.Na_3AlF_6$ has a positive effect on the Fe content, while the $TiO_2.SiO_2$ binary interaction has a negative impact. The ternary interaction of $CaO.SiO_2.TiO_2$, and $SiO_2.TiO_2.Na_3AlF_6$ has shown a favorable and positive effect on iron. $CaO.SiO_2.Na_3AlF_6$ shows a negative effect on iron transfer. Arc stability and current carrying capacity are greatly improved due to the iron content of the coating. According to previous literature, Eq. 5.17, which results from anodic oxidation reactions, can explain the loss of iron and cobalt alloying elements. The trace plots in Figure 5.9 (b) show that CaO and Na_3AlF_6 have positively affected Fe content. The increase in SiO_2 and TiO_2 has a decreasing effect on iron transfer up to the reference blend, and then it starts increasing. From the developed regression model of cobalt, it was observed that an individual constituent has a positive influence on cobalt transfer. The binary interaction of $SiO_2.TiO_2$ and $SiO_2.Na_3AlF_6$ has shown a more favorable and increasing effect on the Co content. The interaction of $CaO.SiO_2.TiO_2$, $CaO.SiO_2.Na_3AlF_6$, and $CaO.TiO_2.Na_3AlF_6$ is the most favorable and positively affects the cobalt. Figure 5.9 (e) shows a trace plot of cobalt; it states that SiO_2 and Na_3AlF_6 positively affect cobalt transfer, whereas CaO negatively impacts Co content. The increase in CaO has an increasing effect on cobalt transfer up to the reference blend; then it slightly decreases.

5.1.5 Effect of flux compositions on microhardness

The microhardness prediction model is shown in Eq. 5.16. The flux composition variation has resulted in a microhardness variation from 225.97 Hv to 282.62 Hv. Figure 5.9 (f) observed that microhardness is increasing with the increase in SiO_2. An increase in CaO has shown a decreasing effect on microhardness. TiO_2 and Na_3AlF_6 have shown an increasing effect up to the reference blend, then start decreasing in the microhardness value. The regression model predicted that an individual constituent has a negative effect on microhardness. The interaction between $CaO.SiO_2$, $CaO.TiO_2$, $CaO.Na_3AlF_6$, and $SiO_2.TiO_2$ has been shown to improve and make the microhardness better. The ternary interaction of $CaO.TiO_2.Na_3AlF_6$ has a decreasing effect on microhardness. The weld beads C11 (225.85 Hv), C9 (228.97 Hv), and C25 (230.85 Hv) have shown minimum microhardness, and C16 (275.22 Hv), C3 (280.69 Hv), and C19 (282.62 Hv) have shown maximum hardness. The phases enriched with Mo are known for their higher hardness in the welds. During welding, the alloying elements in the filler and coating migrate and form carbides and inter-metallic phases, resulting in the welds' hardness. Microhardness decreases when the percentage of acidic ingredients, such as silicon dioxide, increases in the coating composition.

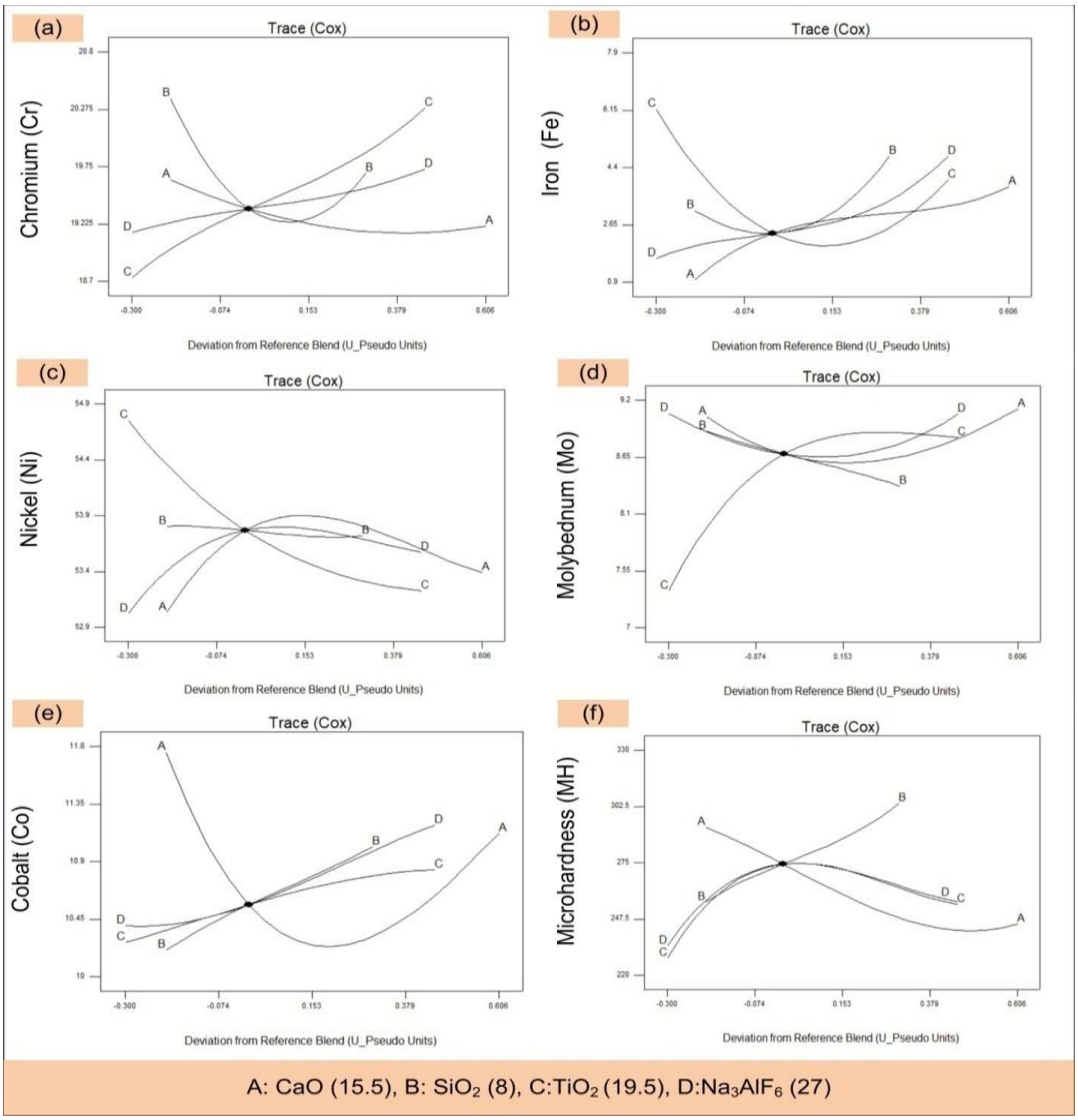

Figure. 5.9 Trace plot showing response variation with the deviation from reference blend (a) Cr, (b) Fe, (c) Ni, (d) Mo, (e) Co, (f) MH

5.6 Contour Plots for different weld responses

The contour plots have been shown in Fig. 5.10. In this plot, the variation of response has been shown in the ternary plot (Na_3AlF_6 = 27). Each color scheme represents a constant value of response. It was reported that the high CaO and SiO_2 with low TiO_2 in the mixture resulted in less loss of chromium. An increase in TiO_2 leads to a loss of iron. Least TiO_2 with high CaO and SiO_2 in the mixture results in the least nickel transfer. Lower CaO and SiO_2 with high TiO_2 have an increase in molybdenum transfer. Microhardness increases with high SiO_2 in the mixture.

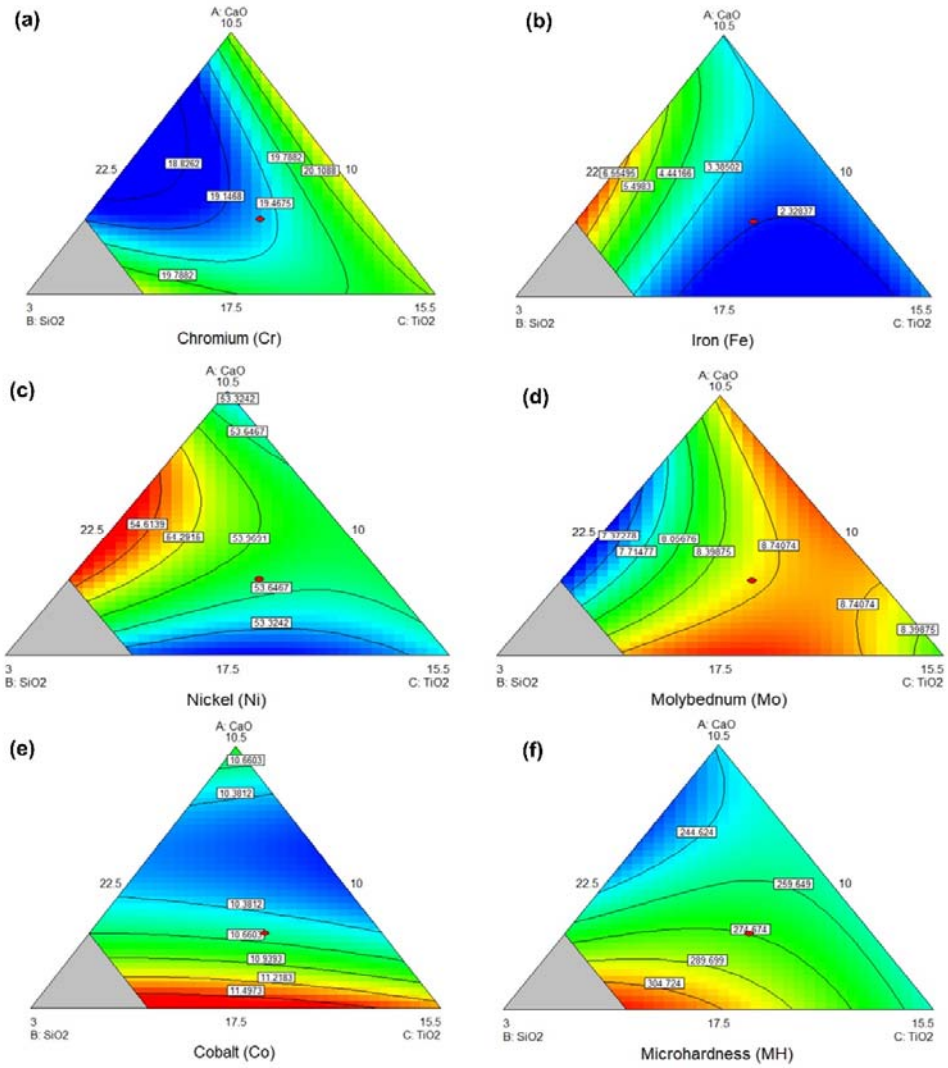

Figure. 5.10 Contour plots showing response variation (a) Cr, (b) Fe, (c) Ni, (d) Mo, (e) Co, (f) MH

5.7 Microstructural analysis of weld bead

The microstructural study of the as-received and welded sample was carried out using a Leica microscope (DMC4500). These samples were taken from the extreme points of the design matrix. Figure 5.11 shows the optical microscopic image. The as-received image of alloy 617 consists of an austenitic structure and annealing twins inside the austenitic grain boundary. Weld metal comprises a columnar grain boundary along with a carbide phase. A typical micrograph with a variable region of columnar grain, migrated grain boundary (MGBs), solidified grain boundary (SGBs), and solidified sub-grain boundary (SSGBs) morphology has been observed. Cr, Nb, and Mo are anticipated to be concentrated in the boundary-segregated precipitates (SGBs and SSGBs) (Shakil et al., 2014). The weld's microstructure varies from region to region and is austenitic with Ni content. The dendritic microstructure is seen in the weld, with precipitates scattered along SGBs and the matrix. The columnar dendrites are primarily located in the weld metal of upper and central areas. MGBs are mainly seen in the center of the weld, which may be attributable to the greater concentration of precipitates along SGBs and SSGBs. It was observed that Mo and Cr enrichment of the precipitates found at SGBs and SSGBs. The Mo-rich phases occur in inter-dendritic regions due to the segregation of Mo, which is more pronounced than that of other alloying elements due to Mo's large radii relative to the Ni matrix and low partition coefficient. The substantial constitutional under-cooling cooling impact of Mo and higher

nickel content is the primary cause of the columnar dendrites in the weld structure (Flemings, 1974). Regardless of coating type, all the multipass welds exhibited a similar microstructure. No variations were found, as both the base and core wires are consistent across all welds.

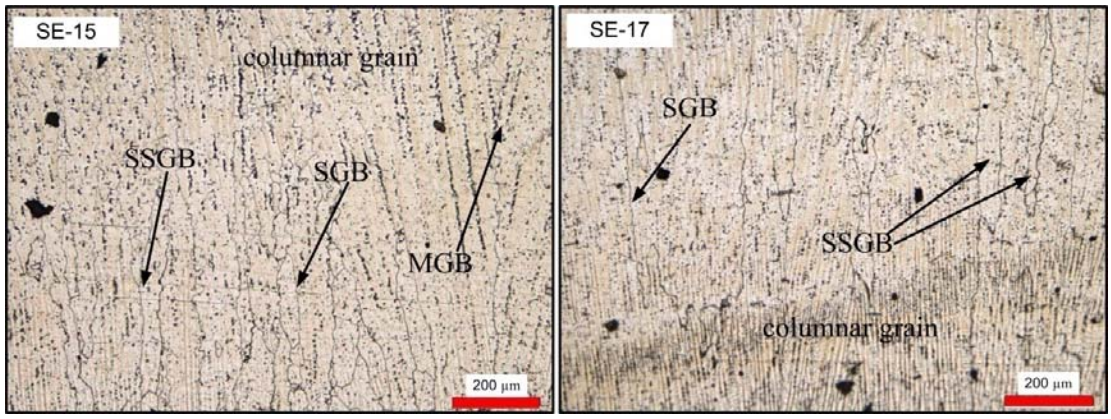

Figure. 5.11 Optical microstructure of weld bead

5.8 Model Validation for a bead on weld experiment

The developed regression models were validated using the actual and predicted values by randomly choosing three coating compositions for confirmatory experiments. The model validation for error percentage and average error percentage for weld chemistry and microhardness are presented in Table 5.11- Table 5.12. The average error percentage for all the responses is under the limit, which validates the model.

Table 5.11- Error percent (%) in the bead on plate for Cr, Fe, Ni

Mixture				Predicted Value			Actual Value			Error (%)		
CaO	SiO_2	TiO_2	Na_3AlF_6	Cr	Fe	Ni	Cr	Fe	Ni	Cr	Fe	Ni
15.00	10.00	20.00	25.00	20.38	3.39	53.74	20.41	3.46	53.28	0.14	2.02	0.86
14.50	10.00	19.00	26.50	20.42	3.09	53.80	20.13	3.06	53.18	1.44	0.98	1.16
14.00	08.00	22.00	26.00	19.91	5.10	54.50	20.31	5.12	53.24	1.96	0.39	2.36
									Avg% Error	**1.18**	**1.13**	**1.46**

Table 5.12- Error percent (%) in the bead on plate for Mo, Co, MH

Mixture				Predicted Value			Actual Value			Error (%)		
CaO	SiO_2	TiO_2	Na_3AlF_6	Mo	Co	MH	Mo	Co	MH	Mo	Co	MH
15.00	10.00	20.00	25.00	8.98	10.26	255.63	8.84	10.46	254.47	1.58	1.91	0.45
14.50	10.00	19.00	26.50	8.96	10.13	255.44	8.85	10.11	260.4	1.24	0.19	1.90
14.00	08.00	22.00	26.00	8.74	11.24	239.88	8.92	11.19	234.16	2.02	0.44	2.44
									Avg% Error	**1.61**	**0.84**	**1.59**

5.9 Selection of final electrodes to fabricate IN617/SS304H DWJs

The multipass bead on-plate analysis was carried out using nickel-based electrodes (IN-617). A total of forty-seven sets of electrodes were tested with core wire (IN 617) for both the flux system and their performance was assessed using qualitative analysis. Among the forty-seven sets of nickel-based electrode coatings examined, the electrodes made with C6, C10 coating (1st flux system) and C5, C6 coating (2nd flux system) performed the best in the qualitative examination of multipass beads deposited with these electrodes. These developed electrodes are referred as E6M, E10M, E5M and E9M, respectively. This study used several deoxidizers such as ferrosilicon, ferrotitanium, ferroniobium, and chromium powders. After adding deoxidizers in small amounts, welding trials were performed. These deoxidizers were added to enhance the bead appearance, slag detachability, cleanliness, and quality of the final welds. The dissimilar welds produced using modified electrode coatings from both flux systems are shown in Table 5.13 and Table 5.14.

Table 5.13- Modified electrode coatings from 1st flux system to produce IN617/SS304 dissimilar joints

Coating	CaO	TiO_2	SiO_2	Na_3AlF_6	CaF_2	Fe-Si	Fe-Ti	Fe-Nb	Cr	Binder
E6M	17.5	15.0	5.0	27.5	15.0	1.0	1.5	2.0	5.5	balance
E10M	11.5	20.0	10.0	30.0	5.0	1.5	2.0	2.5	7.5	balance

Table 5.14- Modified electrode coatings from 2nd flux system to produce IN617/SS304 dissimilar joints

Coating	CaO	CaF_2	SiO_2	SrO	Na_3AlF_6	TiO_2	Fe-Ti	Fe-Nb	Cr	Binder
E5M	20.5	25.0	10.0	5.0	15	10	1.0	0.5	3.0	balance
E9M	15.0	27.5	15.0	7.5	12	5	2.0	1.0	5.0	balance

5.10 Fabrication of IN617/SS304H dissimilar weld joints and its characterization

5.10.1 Non-destructive analysis to analyze defect

The non-destructive test (NDT) to assess any internal defects in the joints was performed on the welded plate.

5.10.1.1 Liquid dye penetration test

The liquid penetrant inspection (LPI) test is a common non-destructive method for inspecting surface flaws, and it is also quite inexpensive. Visual examination is the basis of this method. Figure 5.12(a) shows the initial stage of this approach, which involves using the cleaner to wipe the surface of the specimen that will be analysed. Figure 5.12(b) shows the specimen being evaluated after being exposed to a red liquid, a penetrant, which has strong surface wetting properties. A capillary mechanism allows the penetrant to enter surface discontinuities. Figure 5.12(c) shows that after 8 to 10 minutes of dwell time, or adequate penetration time, the surface is rinsed to eliminate excess penetrant. The trapped penetrant is then brought back to the surface by applying a developer. The specimen's surface was examined and analysed after enough development time had passed. The weld did not exhibit any signs of discontinuities.

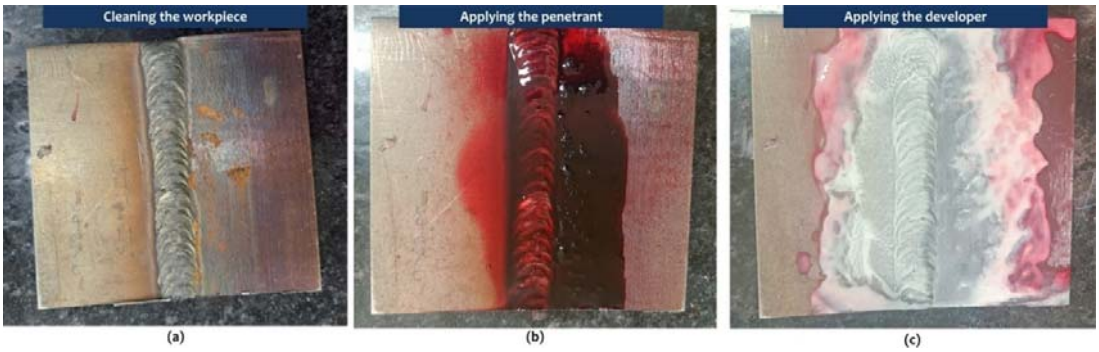

Figure 5.12: (a) Pre-cleaning (b) applying penetrant, and (c) applying developer

5.10.2 Macrostructural analysis

The macrostructure of the IN617/304H DWJ of V-groove geometry with laboratory-developed (E10M, E9M) and commercial electrode (CE) is shown in Figure 5.13- 5.15. The boundary of the weld pass is shown by a dotted line. The number marked represents the sequence of weld passes. The macrograph confirmed that DWJ was free from macroscopic defects. The weld fusion zone area (mm^2) of the laboratory developed are 98±2 (E10M), 88±2(E9M), and 94±2 (CE).

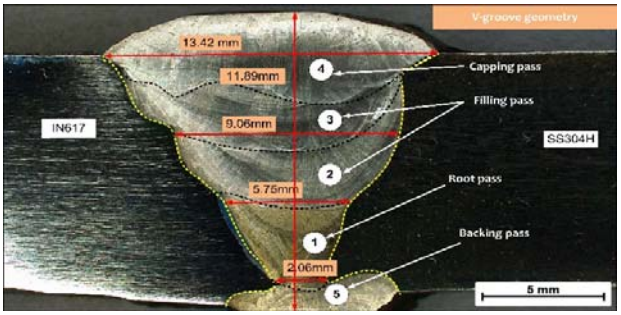

Figure 5.13: Macrograph of fabricated IN617/SS304H DWJ using laboratory-developed electrodes (E10M)

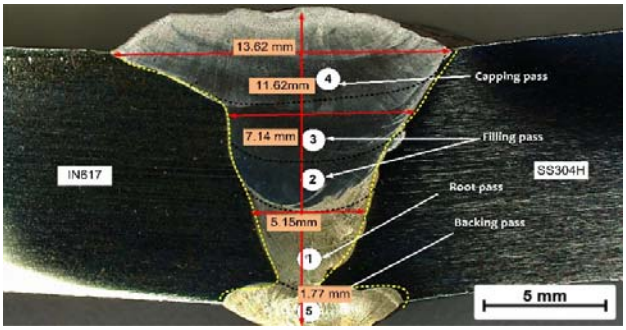

Figure 5.14: Macrograph of fabricated IN617/SS304H DWJ using laboratory-developed electrodes (E9M)

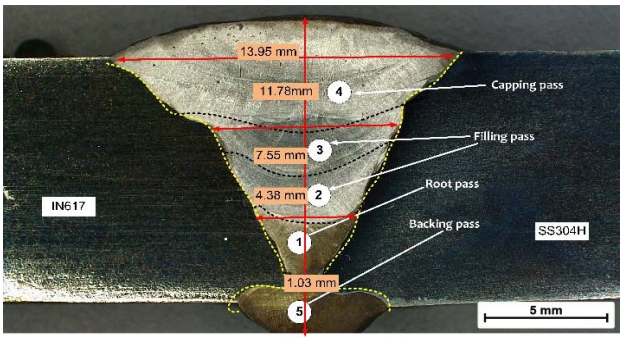

Figure 5.15: Macrograph of fabricated IN617/SS304H DWJ using commercial electrodes (CE)

5.10.3 Weld metallurgical characterization

The optical micrographs of fabricated IN617/304H dissimilar weld using developed electrodes (E9M, E10M) and commercial electrodes (CE) are shown in Figure 5.16- 5.18. It shows the different zones, such as base metal, partially melted zone, weld metal, unmixed zone, and heat affected zone in the given figure.

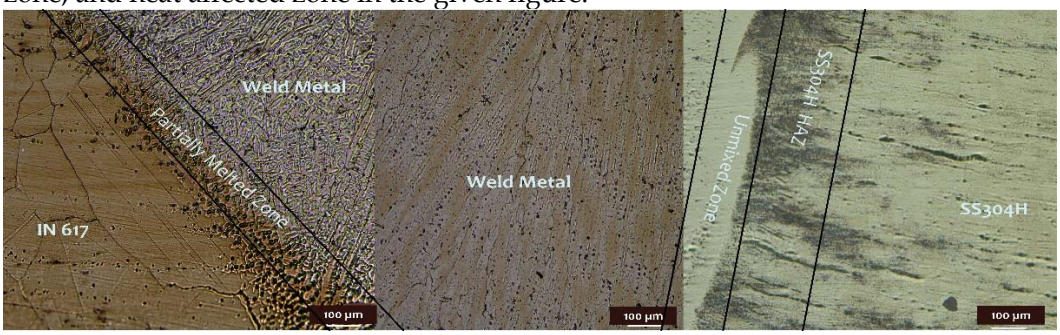

Figure 5.16: Optical micrograph of IN617/SS304H DWJ using developed electrodes (E9M)

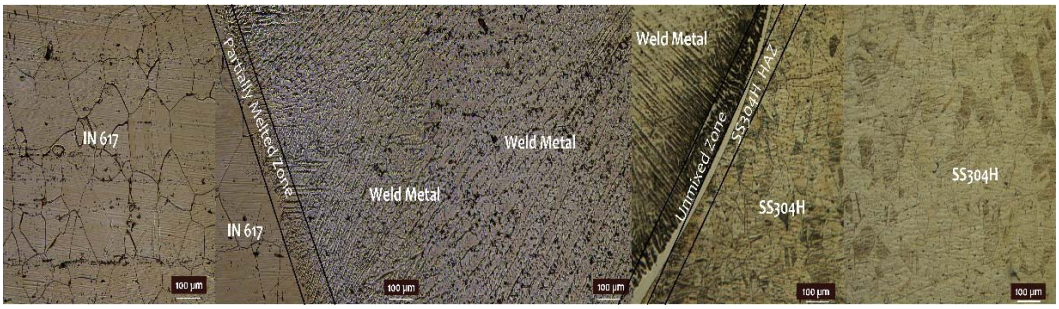

Figure 5.17: Optical micrograph of IN617/SS304H DWJ using developed electrodes (E10M)

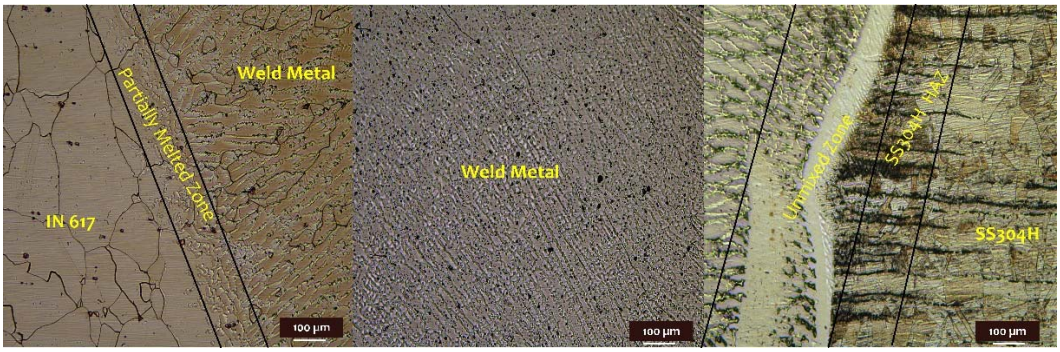

Figure 5.18: Optical micrograph of IN617/SS304H DWJ using commercial electrodes (CE)

5.10.3.1 Base material microstructure

Figure 5.19 (a) shows that the IN617 alloy has an entirely austenitic microstructure with annealing twins and austenite grains of different sizes. Precipitates of different sizes and shapes were observed in the scanning electron micrographs (SEM) pictures (Fig. 5.19 (b)). Among them, Cr-rich $M_{23}C_6$ and Mo-rich Mo_6C were found both within and along the grain boundaries, whereas Ti (C, N) was found intergranular (Bagui et al., 2023; Sirohi et al., 2023a). The EDS results shown in Figure 5.20 confirmed the different precipitates in the IN617 base material. The microstructure of SS304H shows an austenitic with twins and equiaxed polygonal grains, as shown in Figure 5.19(c) and (d).

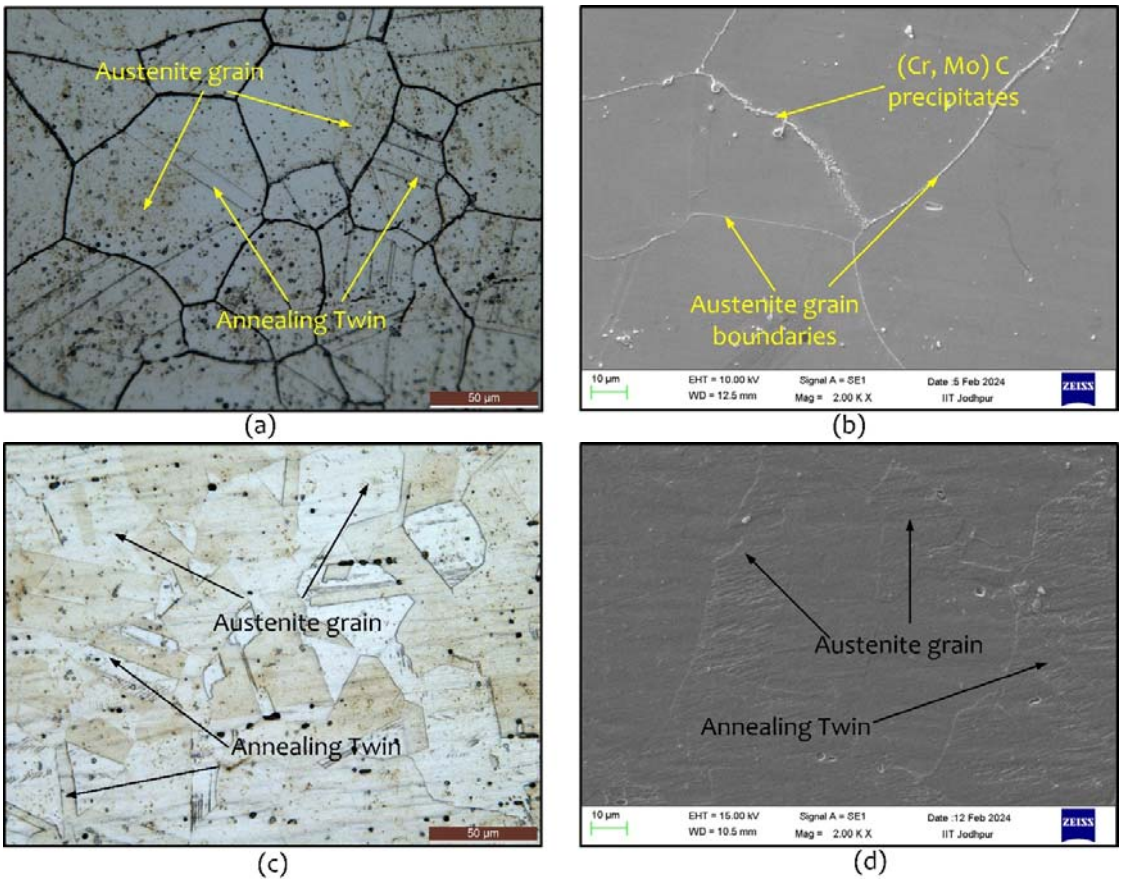

Figure 5.19. Microstructure optical and SEM image (a, b) IN617 alloy, (c, d) AISI 304H steel

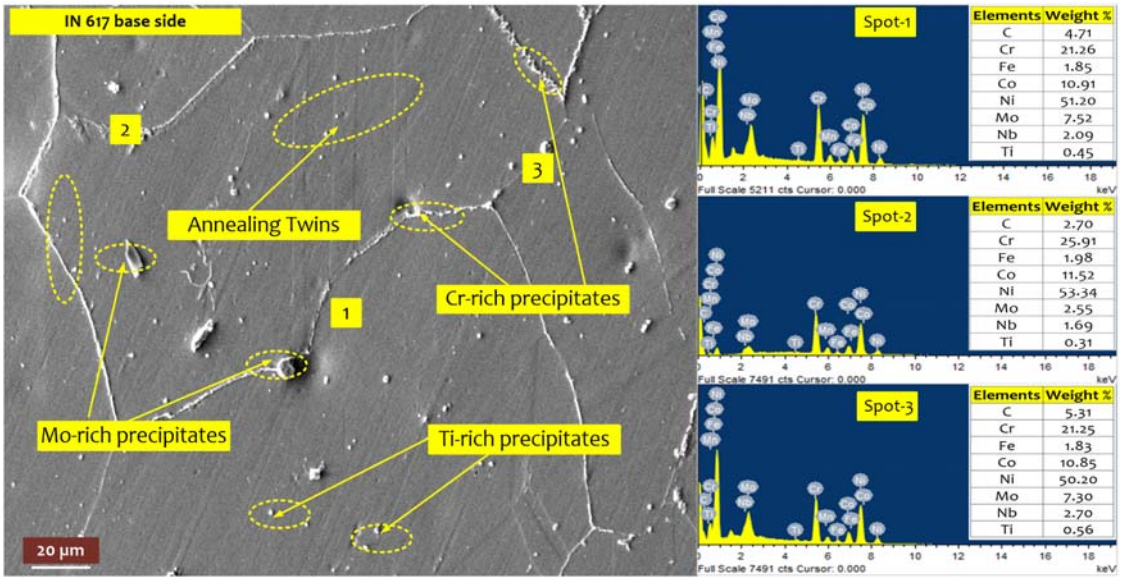

Figure 5.20. SEM micrograph with EDS of IN617 base metal

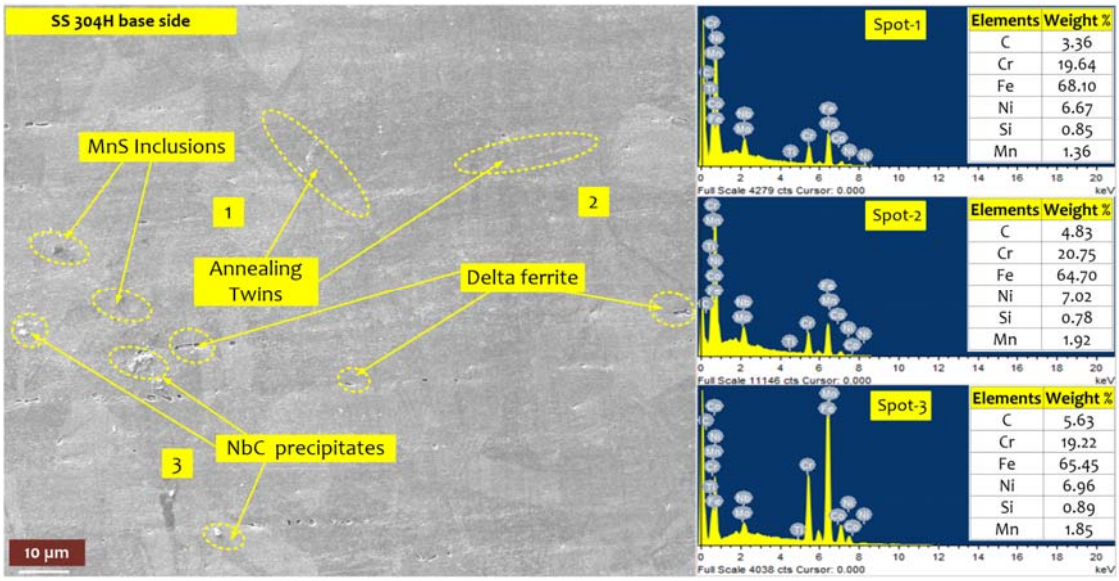

Figure 5.21. SEM micrograph with EDS of SS304H base metal

Figure 5.21 presents the SEM image along with the EDS results of the 304H base material. Images show an equiaxed austenite structure. The structure is characterised by annealing twins, which are formed when austenite grains recrystallize. Additionally, there are Nb-rich precipitates and a minor quantity of MnS inclusions on the 304H side.

5.10.3.2 Weld fusion zone (Interface) microstructure

The unmixed zone (UZ) is the result of variations in thermophysical properties and occurs on the SS304H side of the weld interface fusion boundary where the filler metal (NiCrCoMo-1) is not fully mixed. The UZ was followed by 304H HAZ, which ensures delta ferrite formation and reduces the potential of solidification cracking. Heat dissipation from the fusion zone to the 304H side occurs as a result of 304H higher thermal conductivity than IN617, resulting in the development of the HAZ. Whereas at the IN617 fusion barrier, there is a finer partially melted zone (PMZ) followed by a smaller HAZ. Partially coalescing dissolved molten weld metal and recrystallized weld fusion connecting produced the PMZ. 304H HAZ austenite grains decreases than base metal due to the presence of delta ferrite (Sharma and Dwivedi, 2019). Due to the different chemical composition of the filler and base metal microstructures, a wide unmixed zone is visible on the side of the weld metal fusion interface and the 304H. At the austenite grain boundaries, there is a noticeable presence of Cr-rich carbide precipitation ($M_{23}C_6$) in the form of $(Cr, Co, Mo)_{23}C_6$, but no phase transformation is seen in 304H HAZ (Ding et al., 2018). Figure 5.22 shows the SEM image along with EDS reveal the formation of delta ferrite, which is caused by the high temperatures experienced during welding. This, in turn, causes the appearance of strain-induced martensite, which makes the joint more susceptible to corrosion and has lower tensile strength. The 304H HAZ observed the greater delta ferrite density adjacent to the interface. According to the microstructure at the interface, the representation shows the existence of cellular and columnar structure patterns in the weld metal around the fusion line. The weld metal subsequent to the IN617 BM has a more refined structure than the weld metal near to the AISI 304H BM. A partly melted zone (PMZ) is visible at the IN617 interface, along with a small unmixed zone (UZ). On the AISI 304H side, however, UZ has a broader width parallel to the fusion line. The PMZ occurs as a result of the segregation of impurity elements having low melting at grain boundaries. Furthermore, the grain boundaries inside the PMZ showed a considerable thickening. The significant amount of grain growth was seen at the IN617/weld metal interface. The formation of cellular, columnar, and epitaxial grain within the weld metal and absence of unmixed zone at the interface, can be determined

by the closeness in the elemental composition and microstructure between the weld metal and IN617 base metal. The alloying element segregation was observed at the interface and within the constrained PMZ. SEM/EDS analysis was used to examine the interface area in detail, and the results are shown in Figure 5.23.

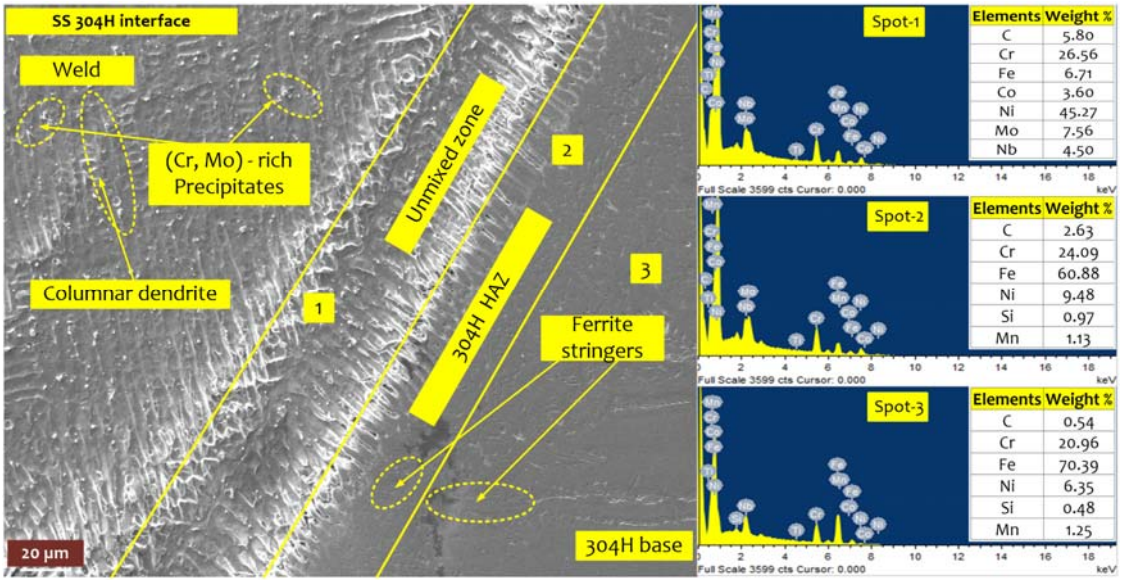

Figure 5.22. SEM micrograph with EDS of SS304H fusion zone (interface)

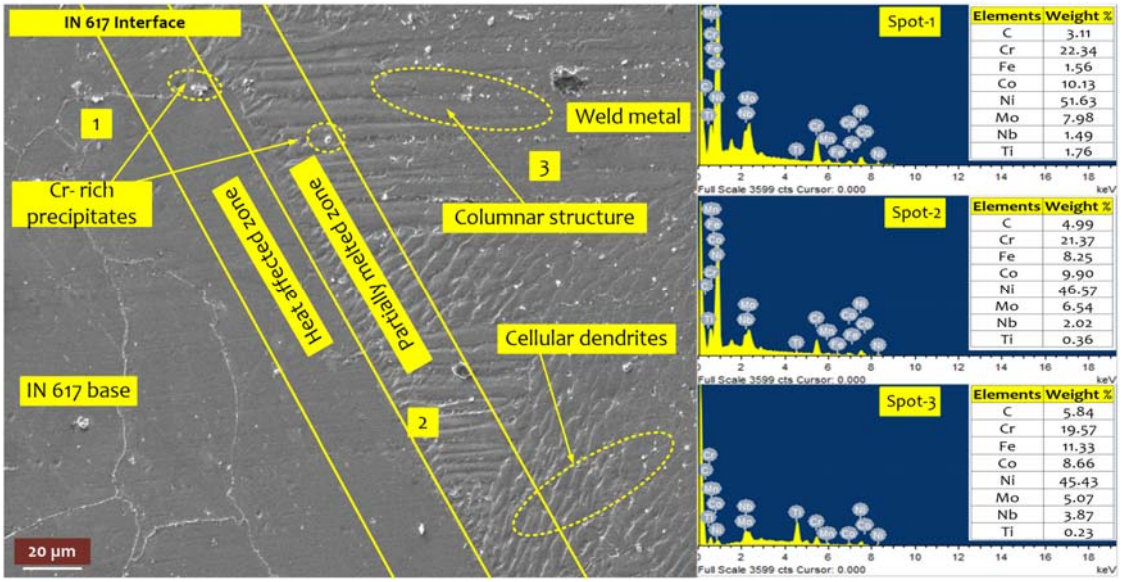

Figure 5.23. SEM micrograph with EDS of In617 fusion zone (interface)

The EDS line mapping was presented in the Figure 5.24. The EDS line map shown in Figure 5.24 and 5.25 illustrates the migration of Fe from 304H to the weld metal. This image demonstrates the movement of the elements Ni, Co, and Mo from the IN617 BM to the weld metal. Nevertheless, the most notable disparity was detected for the element Ni and Fe at the boundary between the AISI 304H and welded metal. The line map analysis revealed a significant rise in Fe intensity close to the IN617 HAZ, which it covered along the IN617 interface. In Figure 5.23 shows the EDS analysis of IN617 interface. The weld metal showed lower Cr, Co, and Ni weight percentages compared to the identical IN617 BM. This might be related to the possible mixture of these two materials (BM and weld metal). The main concentrations of Ni, Co, Mo, Cr, and Fe are shown by the EDS of the weld metal. While the concentration of iron at the interface was higher than that of IN617 BM (8.25%), it was lower

than that of the weld (11.33%). Additionally, the interface had greater amounts of Co, Ni, Cr, and Mo compared to the weld. Both side of weld interface have been subjected to the area mapping, as seen in Figures 5.26 and 5.27. The 304H interface is depicted in Figure 5.22. The results show that the variation of Cr and Mo concentration in the weld metal adjacent to the interface occurs due to which Cr-rich and Mo-rich carbide precipitates formed. Weld metal shows the higher concentrations of Cr, Ni, Co, and Mo than SS304H BM. It was also observed that the concentration of carbon increases slightly at interface because of carbon diffusion from 304H BM to weld metal. The Fe and Ni concentration are clearly observed at the interface of SS304H. The area mapping of IN617 interface is depicted in Figure 5.25. It was confirmed that Mo, and Cr are the major phase in base metal of IN617. The diffusion of Ni, Cr, Mo, and Co confirmed at the interface region. The Ti (C,N) phase formed at some point in IN617 BM due to the more Ti concentration present. Ti (C,N) phase formed near the weld metal interface. From figure 5.21 and 5.22, The 304H HAZ shows the ferrite stringers along with twins and equiaxed austenite structure. Ferrite stabilising components, such as Cr, segregate during solidification, which is an important factor that aids in the development of the ferrite stringer (Lippold and Kotecki, 2005). The substantial grain development occurs in IN617HAZ. The enlargement of grain size occurs within IN617 HAZ near the fusion line are also reported by (Hosseini et al., 2011). It was also observed intra and inter-granular precipitates. Along with the austenitic boundaries and inside the matrix, fine and coarse carbide phases were visible in the HAZ. Specifically, lamellar carbides gradually formed at grain boundaries within the HAZ. This change in behaviour was not seen in the IN617 BM and was caused by weaker grain connections. Furthermore, it was observed larger size of carbide phases then IN617 BM because of the effect of high temperature produce by welding.

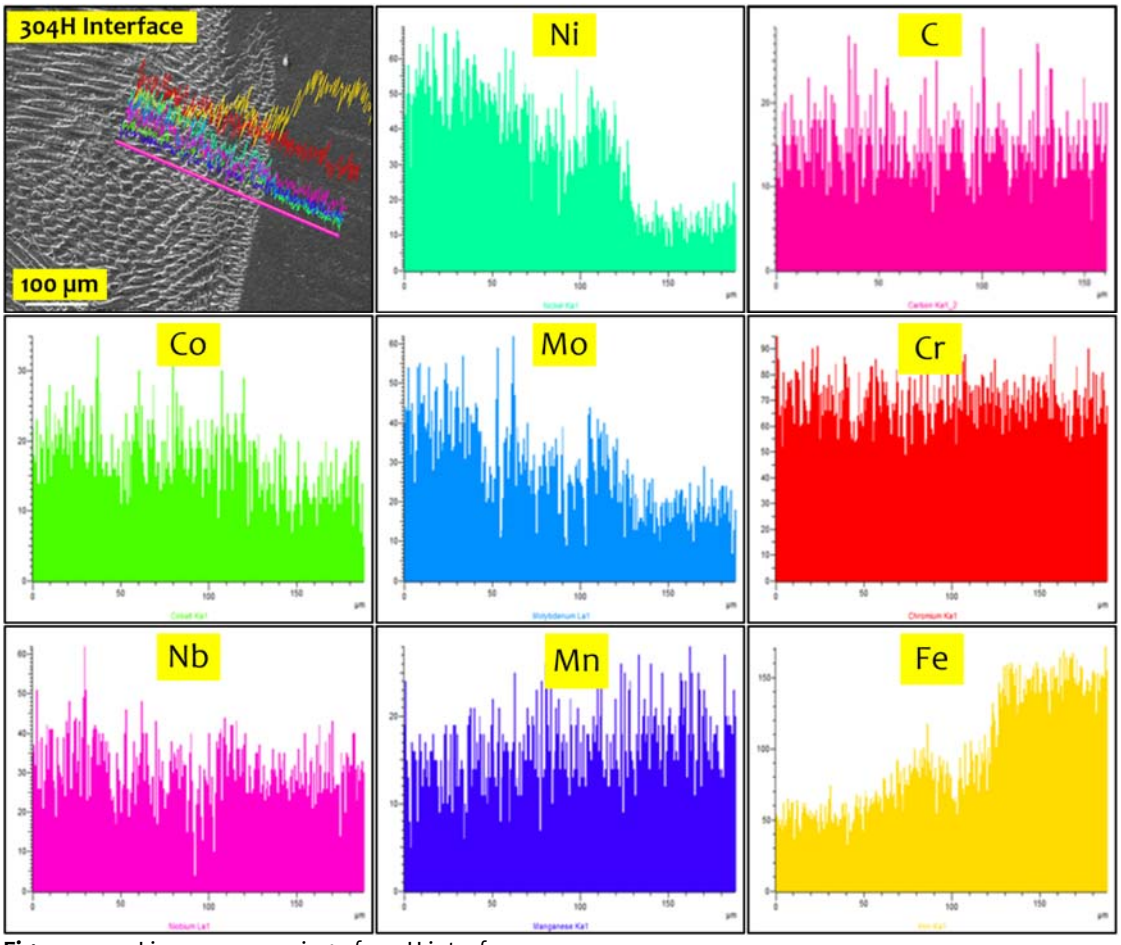

Figure 5.24. Line scan mapping of 304H interface

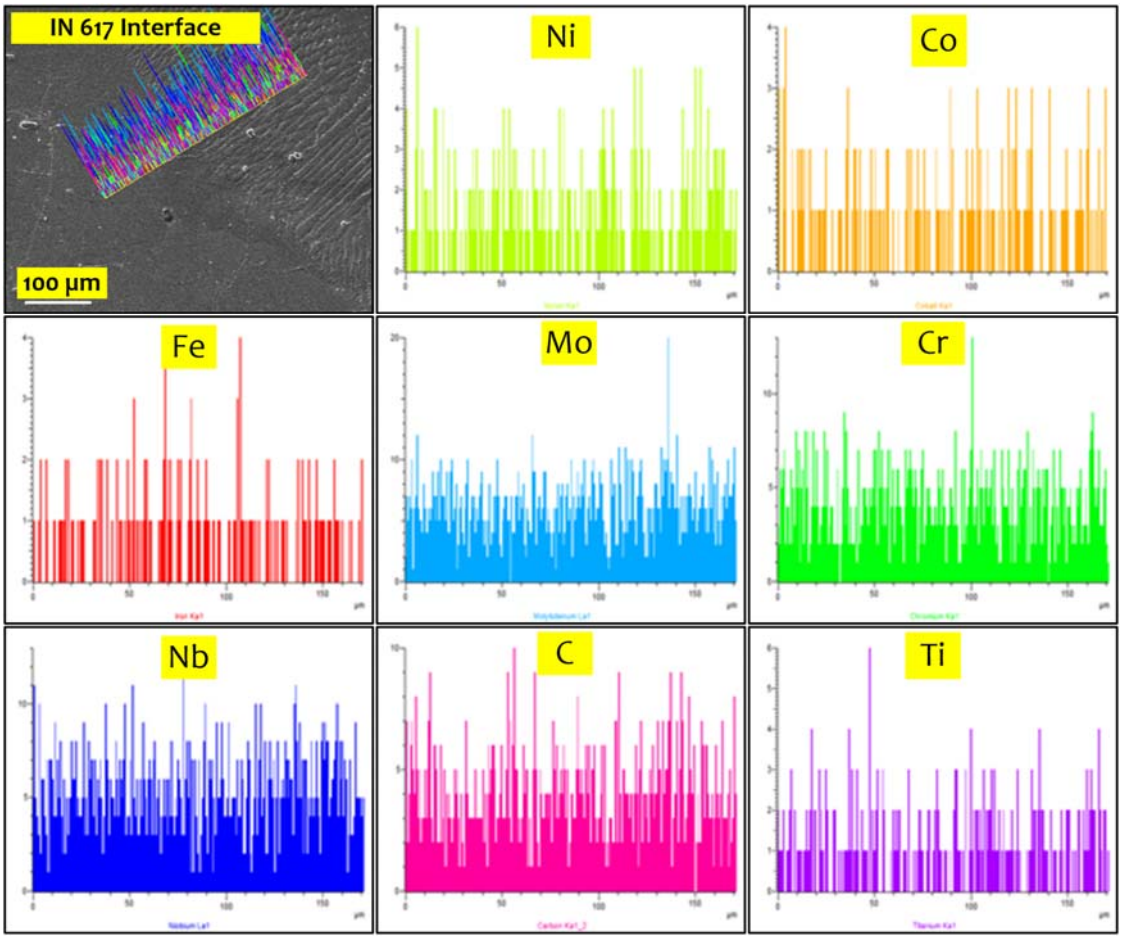

Figure 5.25. Line scan mapping of 304H interface

5.10.3.3 Weld metal microstructure

The scanning electron microscopy (SEM) images of weld metal reveal a microstructure having dendritic grain characterised by columnar solidification and grains that are elongated in the direction counter to the heat extraction. As a result of the enrichment of Mo, Cr and C during welding solidification, the microstructure is composed of higher concentration of Mo-rich precipitates, Cr-rich precipitates located between dendritic areas, and dispersed Ti-rich precipitates randomly. Figure 5.28 shows that the weld metal zone is strengthened by the small particles (fine) precipitates seen within the dendrites. A heterogeneous microstructure was formed inside the weld metal as a result of changes in solidification modes caused by changes in cooling rates of weld zones from top to root region. The amount of constitutional super cooling is a major determinant of the dominating solidified microstructure inside the weld metal. Different region presents different microstructure. The equiaxed dendrite was observed at the upper region of weld due to the segregation of alloying elements. The weld metal observed columnar and cellular dendrite structure. The occurrence of this structure is due to inter-dendritic segregation of alloying elements. It was also reported by previous studies that constitutional cooling is also responsible for the transformation of cellular to columnar dendrite (Hajiannia et al., 2013). From the figure 5.28, shows that the interdendritic area of austenitic includes secondary phases. The dendritic core observed the major element such as, Cr, Ni, Fe, and Co whereas, Cr and Mo along the interdendritic region. It was also observed that greater concentration of Mo and Cr in the inter-dendritic region. This is because the segregation of Cr and Mo during the solidification. Figure 5.29 shows the area mapping of weld metal.

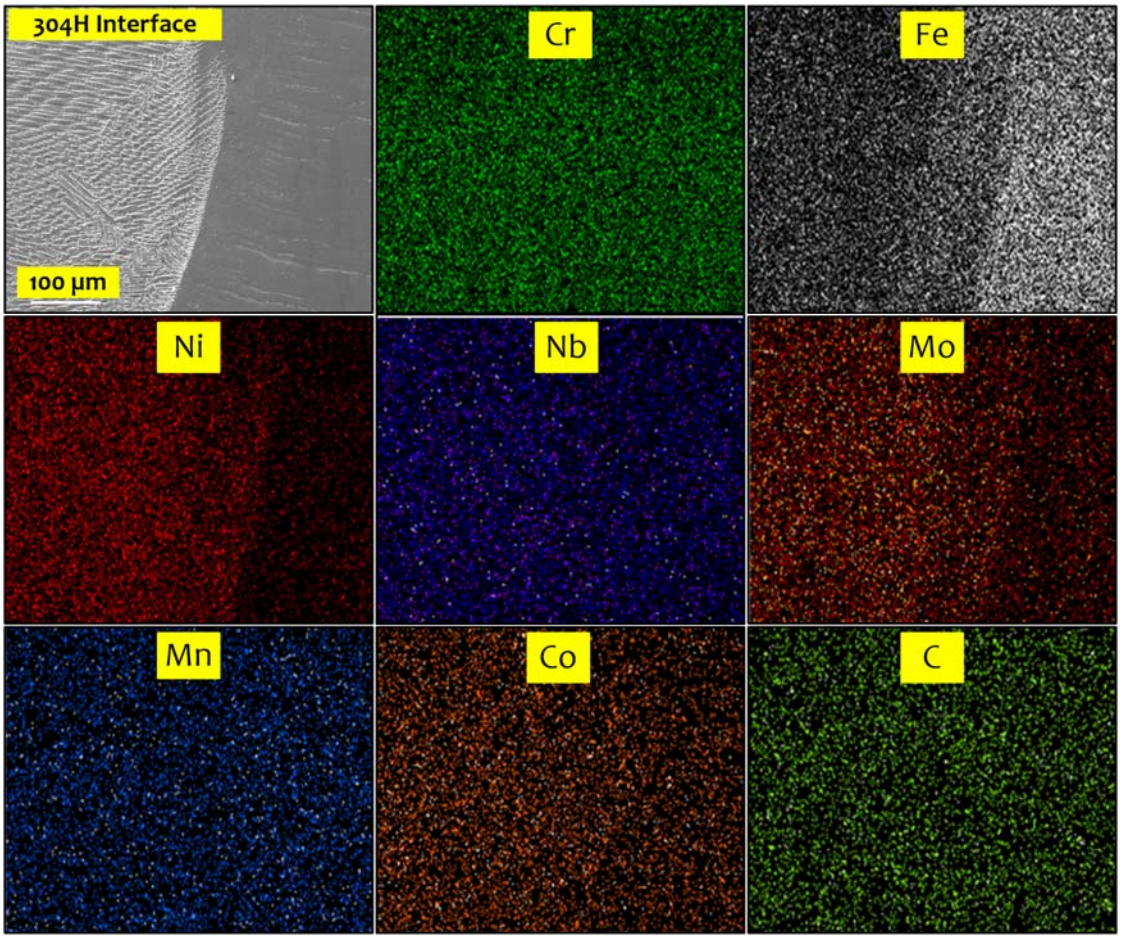

Figure 5.26. Area mapping of 304H interface

The M_6C and $M_{23}C_6$ carbide precipitates rich with Cr and Mo was observed in the inter-dendritic region. Research has been reported earlier that Ni-based alloy and steel weldments present the formation of secondary phases in the weld metal. The segregation of alloying elements and rapid cooling after solidification is the main factor for the formation of secondary phases in the weld metal (Kangazian and Shamanian, 2018; Ramkumar et al., 2015; Ren et al., 2015; Shakil et al., 2014). The NbC precipitates also observed and reported by the (Naffakh et al., 2010). Hence, the secondary phases observed in the weld metal have similar structure and content to those observed in the base metal 617.

The microstructure of dissimilar weld made with commercial electrodes are shown in Figure 5.30- 5.32. The welds made using both commercial and laboratory-developed electrodes exhibit a similarity in the microstructure of the weld zone. This is mostly because identical filler wire was utilized. The only change is in the coating composition, which has small effect on the microstructure of the weld area; however, the different zones shows a significant variation in the width of different zone. A broader region of unmixed zone was observed in the 304H interface in the case of weld made with commercial electrode. The elongated columnar structure with coarse grain was observed at the 304H interface region as compared to commercial electrode. The columnar dendrite with coarse grain was observed near the weld metal and IN617 interface. The segregation of alloying elements was observed near the weld metal and within the PMZ.

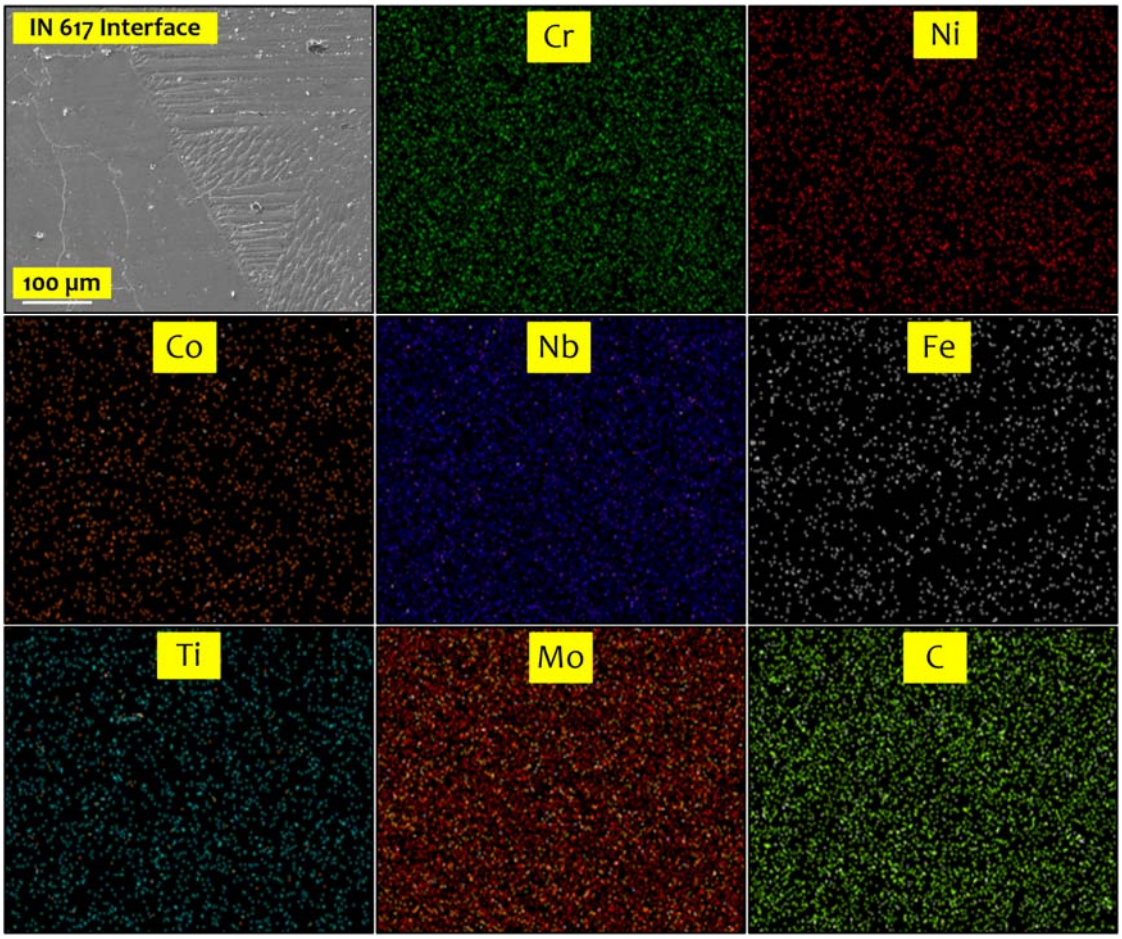

Figure 5.27. Area mapping of IN617 interface

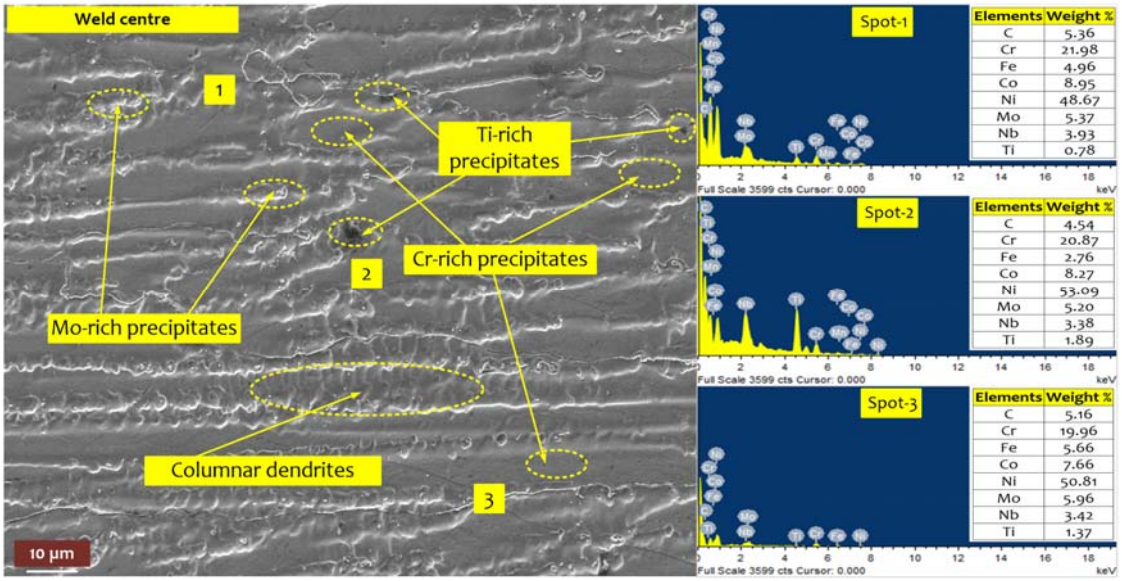

Figure 5.28. SEM micrograph with EDS of weld metal

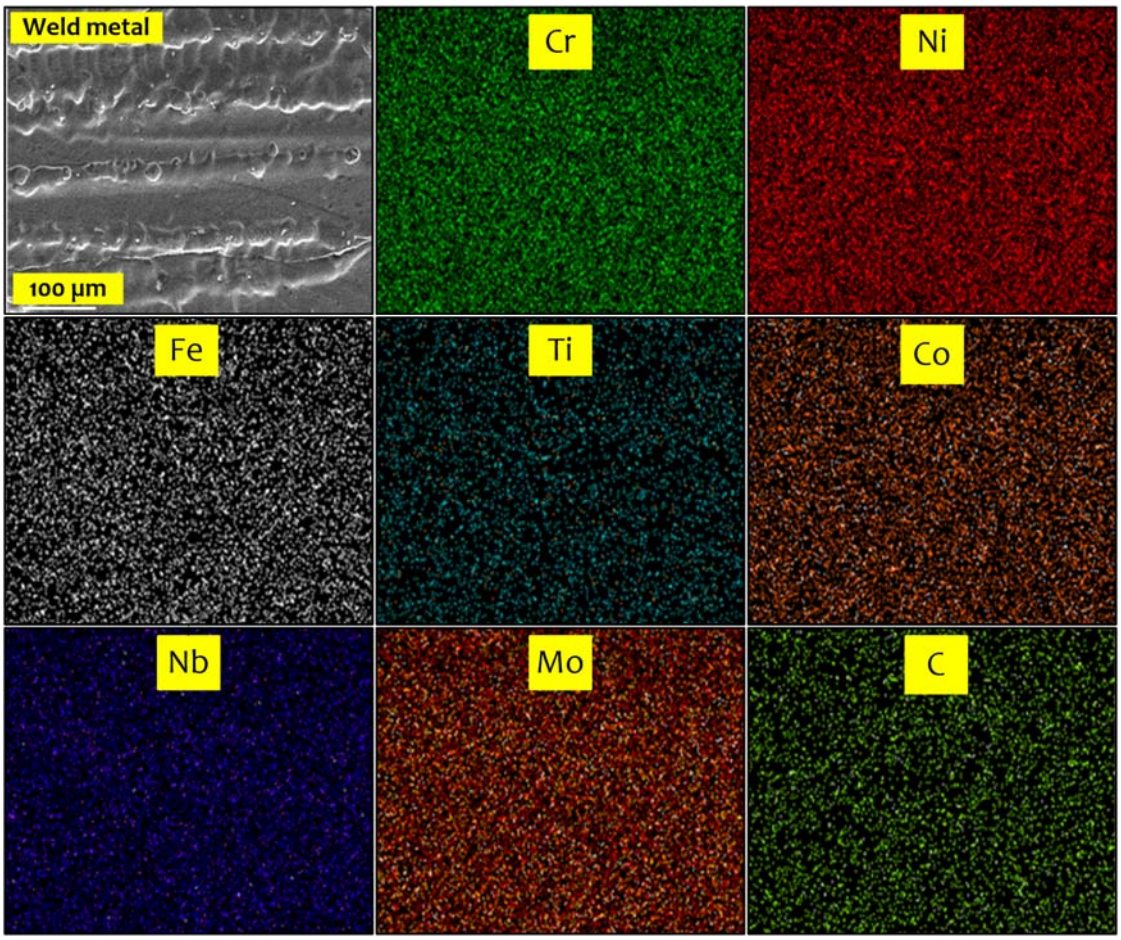

Figure 5.29. Area mapping of weld metal

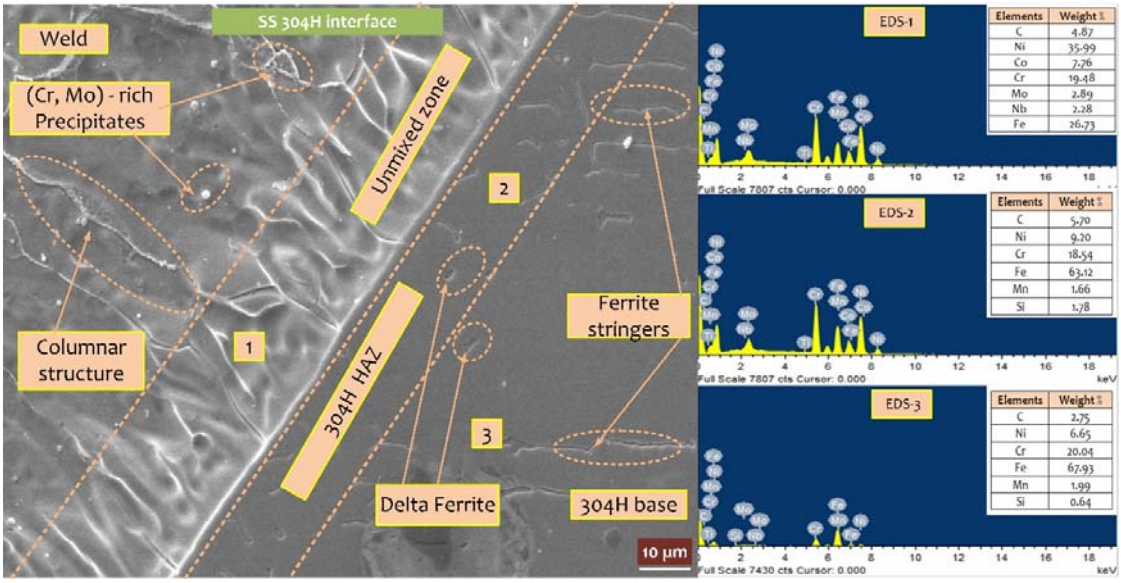

Figure 5.30. SEM micrograph with EDS of SS304H fusion zone (interface) of weld CE

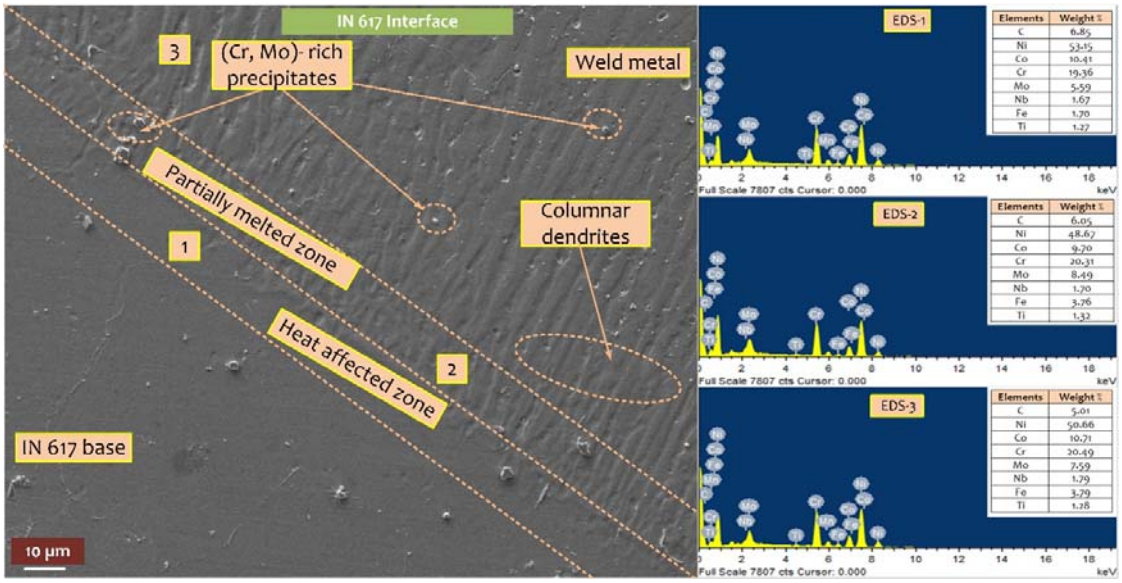

Figure 5.31. SEM micrograph with EDS of IN617 fusion zone (interface) of weld CE

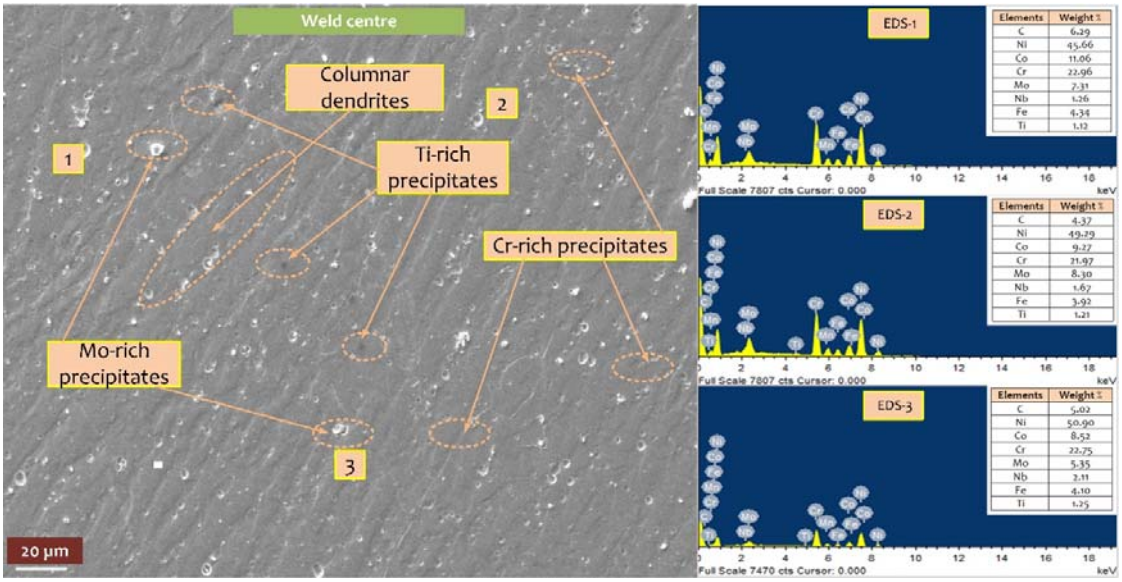

Figure 5.32. SEM micrograph with EDS of weld metal of weld CE

5.10.4 Mechanical characterization

Tensile test was conducted on the specimens extracted from the IN617/304H dissimilar weld joints (DWJ) made using laboratory developed electrodes and commercial electrodes for both the flux system. The tensile test of base material and the fabricated welds were performed on the universal testing machine. The tensile properties of the base metal and fabricated welds for the 1st system was summarized in Table 5.15. The ultimate tensile strength of the IN617 and SS304H (BM) was recorded as 774 MPa and 738 MPa, respectively. The ultimate tensile strength and yield strength of weld made using E10M electrodes was observed as 692 MPa and 335 MPa, respectively. This value of tensile strength was observed higher than value of CE electrode but lower than the 304H base metal. The presence of Cr-rich carbides with fine columnar grains across the fusion zone enhance weld higher tensile strength. The stress strain curve is shown in Figure 5.34



Figure 5.33. Tensile specimens after fracture for 1st system

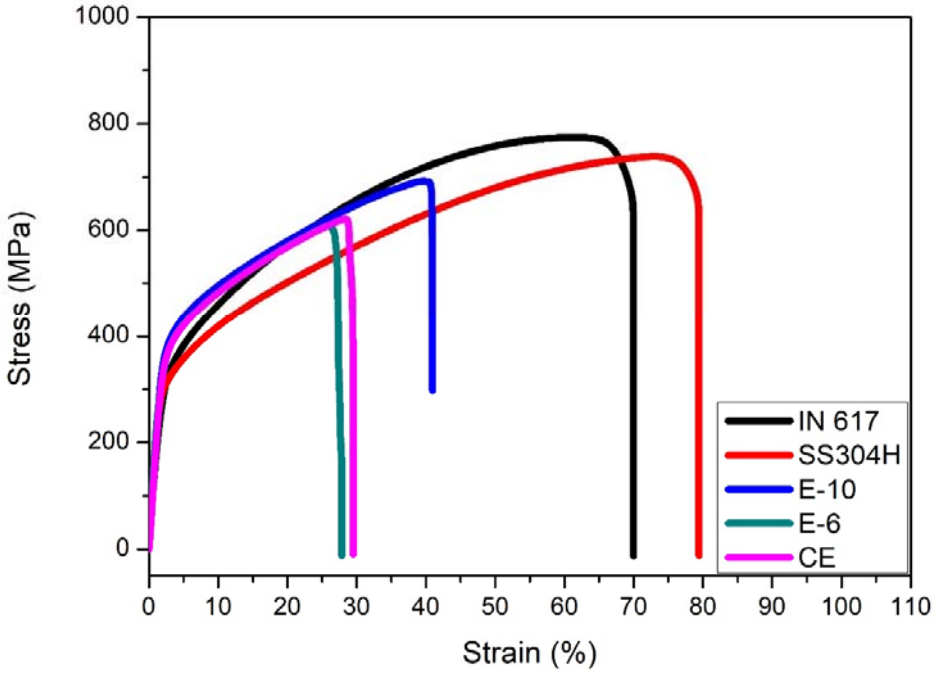

Figure 5.34. Stress strain curve of different specimen for 1st system

Table 5.15: Tensile properties of base and welds for 1st system

Specimens	Tensile strength (MPa)	Yield strength (MPa)	% elongation	Fracture location	Weld mismatch with IN617	Weld mismatch with SS304H
IN617 BM	774	380	70	-	-	-
304H SS BM	738	270	79	-	-	-
E10M	692	335	41	SS HAZ	0.89	0.93
E6M	608	310	28	Weld centre	0.78	0.82
CE	621	290	29	Weld centre	0.80	0.84

The addition of cryolite in the laboratory developed electrode improves the slag detachability and weld cleanliness in nickel wire-based electrodes operating in basic flux systems. Therefore, it produces better weld quality (Sham and Liu, 2014; Wang and He, 2016). Cryolite in coating fluxes increases tensile strength by improving weld pool protection and refining the grain structure of the weld metal. The tensile strength of weld CE is lower due to the segregation of alloying elements (Arivarasan and Kannan, 2022; A. H. V. Pavan et al., 2015b; Sirohi et al., 2023a). The tensile strength outcome findings of dissimilar weld with Ni alloy was reported by (Sirohi et al., 2023b). The fractured location is shown in the Figure 5.33. The fractured surface was analyzed using the fractography of all the tested samples. Figure 5.35(a,b) shows the fractography analysis of IN617 and 304H base metal. Fracture modes and voids were examined in all the fractography analysis. Both dimples and cleavage facets were present in the fractography of IN617 base metal. The volume of cleavage facets is higher than that of dimples, indicating a mixed fracture mechanism. While in the case of 304 H base metal, fractography revealed more dimples as compared to cleavage facets, showing that the SS304 H failed in the ductile mode (Ahmad et al., 2021). Fractography of weld made using commercial and developed electrodes (E10M) are presented in figure 5.35 (c,d). Both weld samples were found dimples and cleavage facets. The area of dimples in weld made by E10M is larger as compared to commercial electrode, Hence the mechanism of fracture may be confirmed as ductile mode. This implies the higher ductility occur with the weld made by E10M during tensile test.

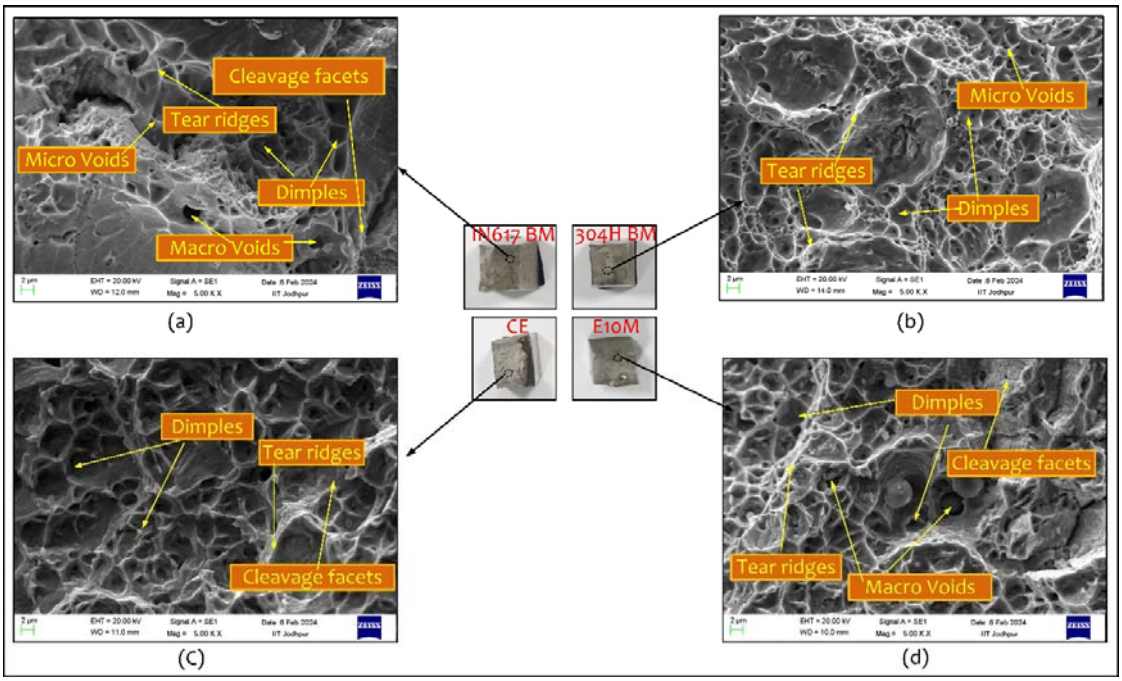

Figure 5.35. Fractography of tensile specimen for 1st system

Similarly, the tensile properties of the base metal and fabricated welds for the 2nd system was summarized in Table 5.16. The ultimate tensile strength of the IN617 and SS304H (BM) was recorded as 774 MPa and 738 MPa, respectively. The ultimate tensile strength and yield strength of weld made using E9M electrodes was observed as 743 MPa and 360 MPa, respectively. This value of tensile strength was observed higher than value of CE electrode and greater than the 304H base metal. The fractured location of E9M is from 304H base metal, which confirm that higher tensile strength exists for weld. The tensile specimen after fracture is shown in the Figure 5.36. The stress strain curve is shown in Figure 5.37. The fractography of the fractured specimen were done to analyze the behaviour of fracture. The analysis of fracture specimens is shown in Figure 5.38.

Table 5.16: Tensile properties of base and welds for 2nd system

Specimens	Tensile strength (MPa)	Yield strength (MPa)	% elongation	Fracture location	Weld mismatch with IN617	Weld mismatch with SS304H
IN617 BM	774	380	70	-	-	-
304H SS BM	738	270	79	-		
CE	621	290	29	SS HAZ	0.80	0.84
E5M	669	325	44	SS HAZ	0.86	0.90
E9M	743	360	62	SS base	0.95	1.00



Figure 5.36. Tensile specimens after fracture for 2nd system

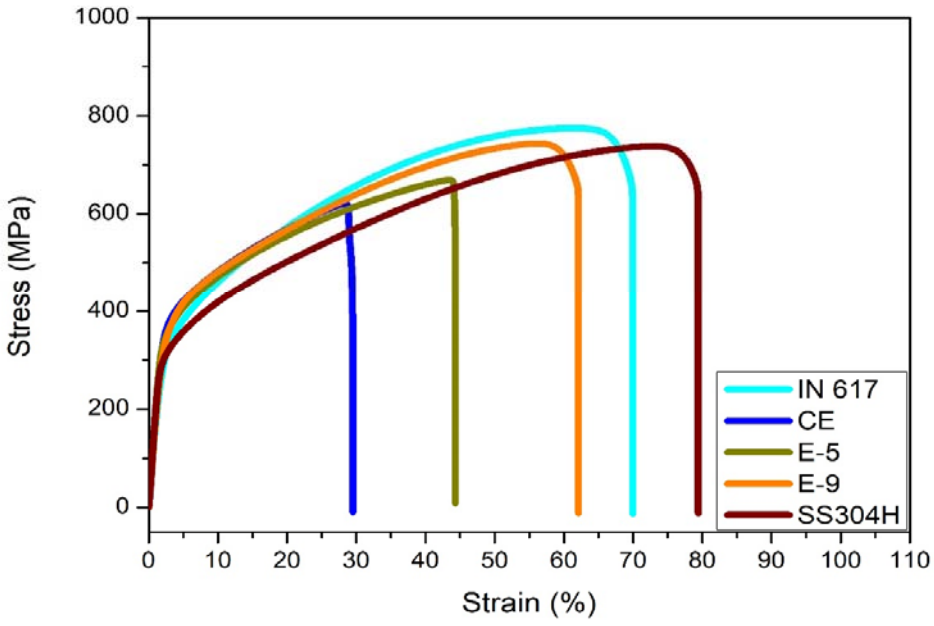

Figure 5.37. Stress strain curve of different specimen for 2nd system

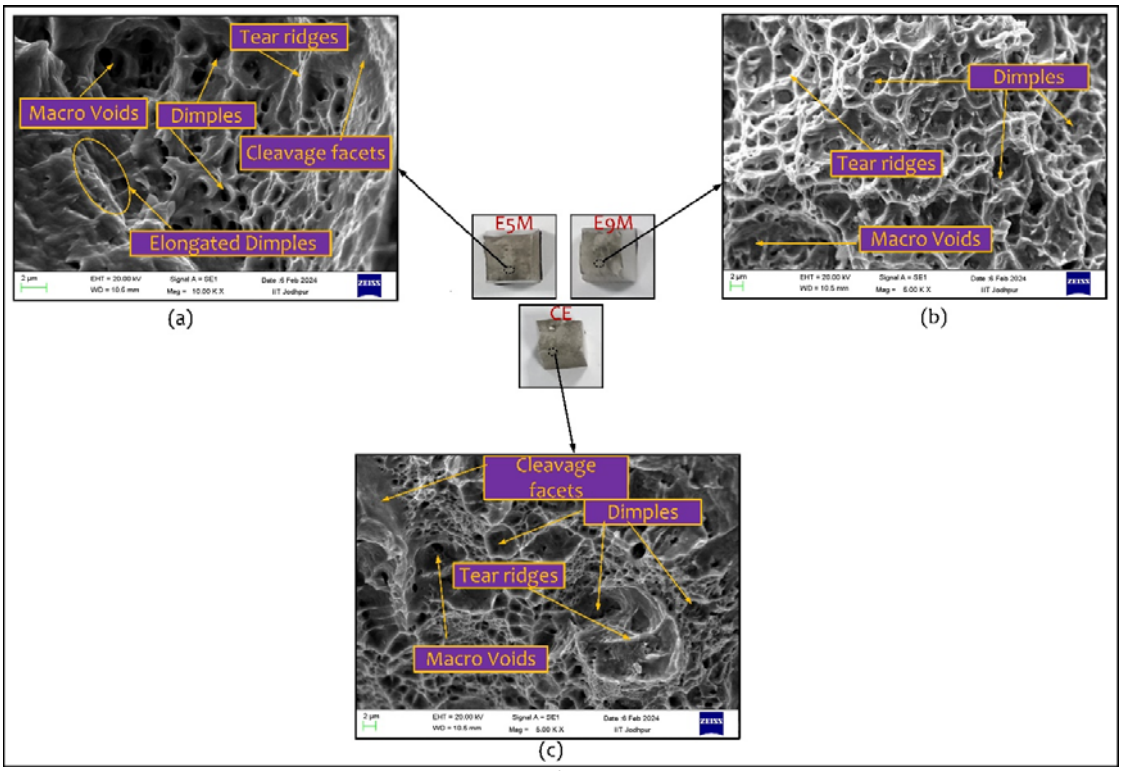

Figure 5.38. Fractography of tensile specimen for 2nd system

Weld joint impact toughness indicates the amount to which the joint can absorb impact energy quickly before fracture. The impact toughness of dissimilar welds is crucial for the production of AUSC power plant components, as these welds are subjected to exceptionally high temperatures that influence the total weld joint composition. The weld fusion zone behaviour under rapid impact load was determined using the impact toughness test. A Charpy V-notch impact tester, which is pendulum-type, was used to measure the weld fusion zone's toughness at room temperature. A V-notch was cut into the weld along its thickness. The impact toughness test was carried out on the base metal and welded specimens on sub-standard size of ($55 \times 10 \times 7.5$ mm^3) at room temperature. Three specimens from each case was carried out for impact toughness test and the average values of toughness was reported. The specimens with the V-notch in the centre of the weld, which are used to measure charpy impact toughness, are shown in Figure 5.39 both before and after the test. The results of the impact toughness test for the 1st system is summarized by bar chart as shown in Figure 5.40. A minimum impact energy of 47 J is necessary to meet the requirements of the European standard EN 1599:1997 for the AUSC application and to reduce the likelihood of brittle fracture in the weld metal. The average impact energy of IN617BM and 304H BM is 230 J and 285 J respectively. The austenitic grains in the 304H BM are wrought and annealed, which contributes to their high impact energy. The impact toughness values for all produced weld was lower than the base materials and higher than the required permissible values. The lower impact toughness of the weld metal is due to the segregation of alloying elements along the inter-dendritic region as reported by (Sirohi et al., 2023a; Yılmaz and Tümer, 2013). It was also reported by previous studies that weld metal oxygen is decrease and toughness is increase by a high basicity flux. Weld metal oxygen levels are reportedly significantly reduced when CaO is substituted with CaF_2, leading to an improvement in toughness (Natalie et al., 1986). The fractography of the impact fractured specimen were done to analyze the behaviour of fracture. The analysis of fracture specimens is shown in Figure 5.41.

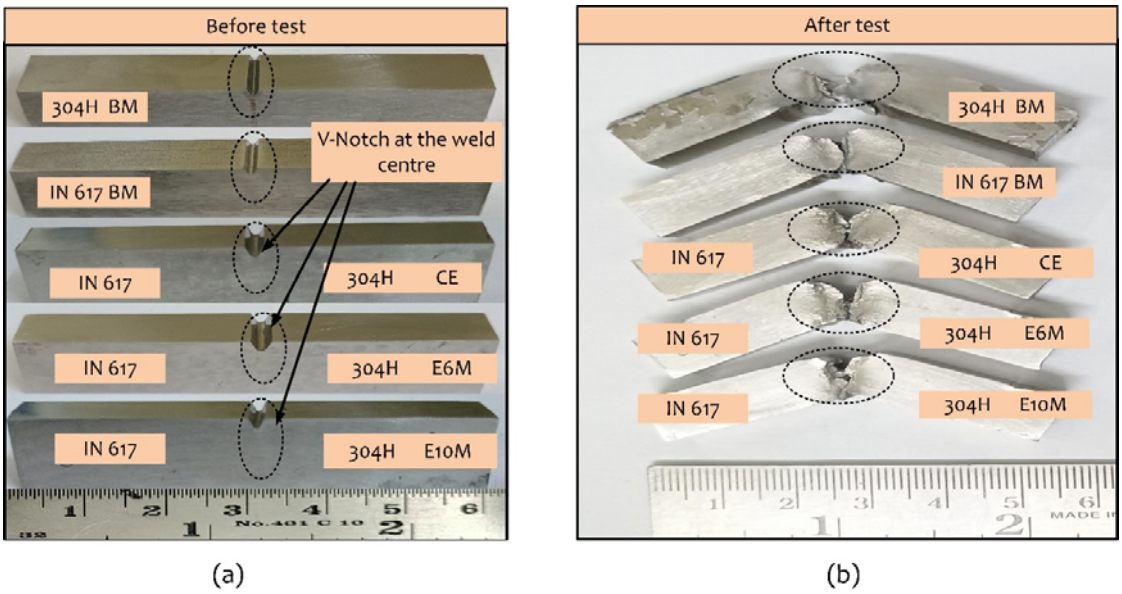

Figure 5.39. Impact toughness specimen before and after test for 1st system

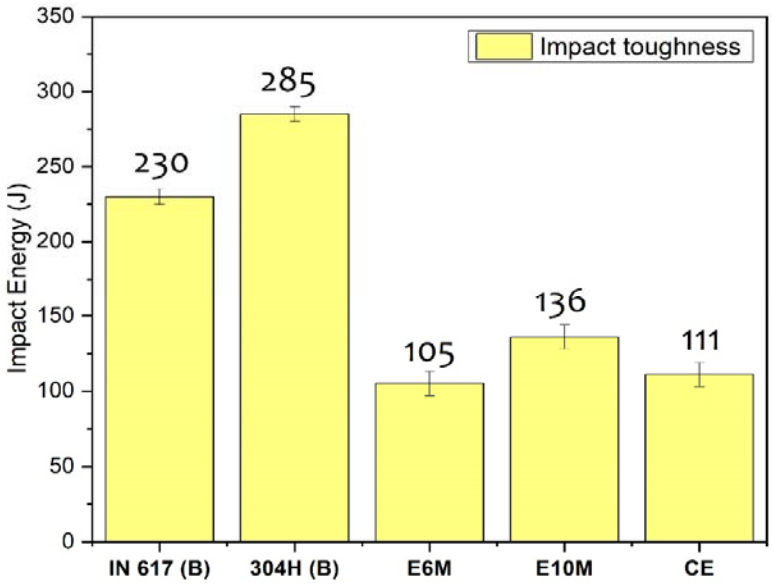

Figure 5.40. Impact toughness results for 1st system

Figure 5.41 (a,b) shows the impact fractography analysis of IN617 and 304H base metal. Fracture modes and voids were observed in all the fractography analysis. Both dimples and cleavage facets were present in the fractography of IN617 base metal. The volume of cleavage facets is more than that of dimples, indicating a ductile-brittle mode of fracture. While in the case of 304 H base metal, fractography revealed more volume of dimples as compared to cleavage facets, showing that the SS304 H failed in the ductile mode (Arivarasan and Kannan, 2022). Fractography of weld made using commercial and developed electrodes (E10M) are presented in figure 5.41 (c,d). In both weld samples, dimples and cleavage facets were present. The area of dimples in weld made by E10M is larger as compared to commercial electrode, which confirmed as ductile mode of fracture.

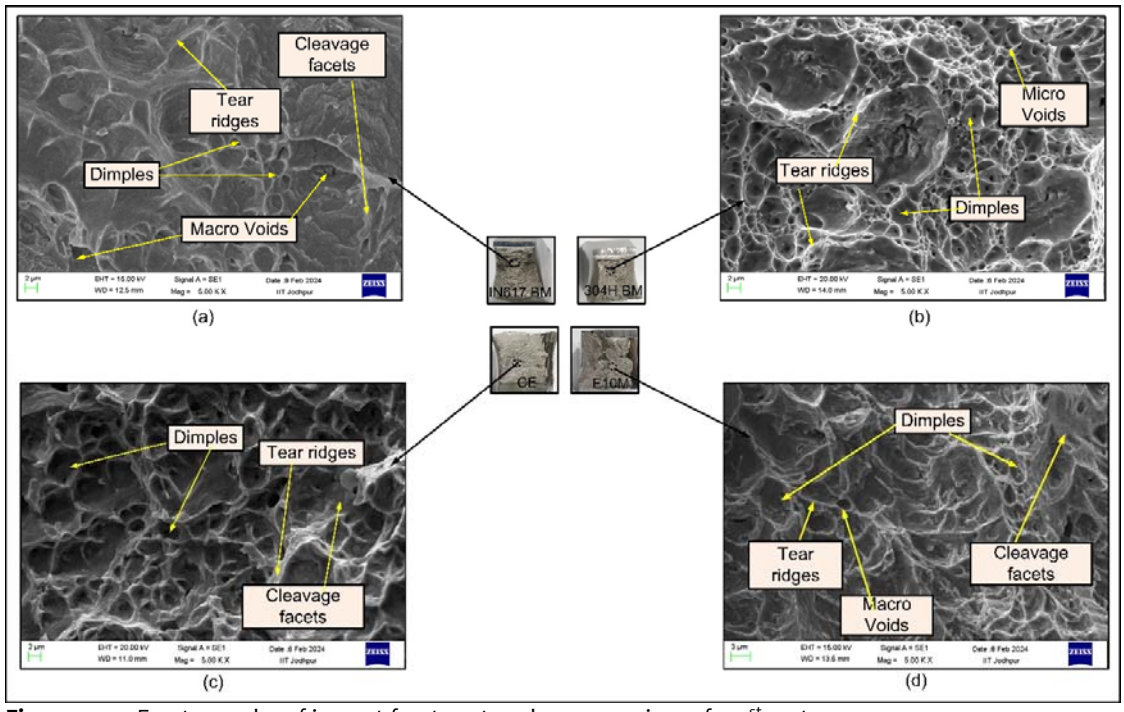

Figure 5.41. Fractography of impact fracture toughness specimen for 1st system

Similarly, the specimens with the V-notch in the centre of the weld, which are used to measure charpy impact toughness, are shown in Figure 5.42 both before and after the test for 2nd system. The results of the impact toughness test for the 2nd system is summarized by bar chart as shown in Figure 5.43. A minimum impact energy of 47 J is necessary to meet the requirements for the AUSC application and to reduce the likelihood of brittle fracture in the weld metal. The impact toughness values for all produced weld was lower than the base materials and higher than the required permissible values. The impact fractured specimen fractography were done to analyze the behaviour of fracture. The analysis of fracture specimens is shown in Figure 5.44.

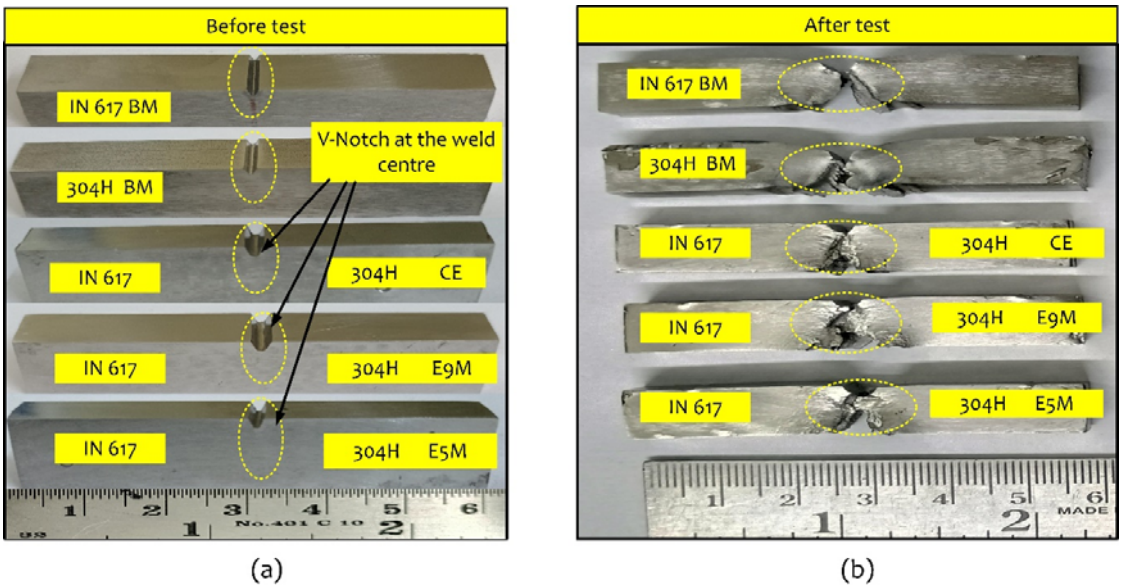

Figure 5.42. Impact toughness specimen before and after test for 2nd system

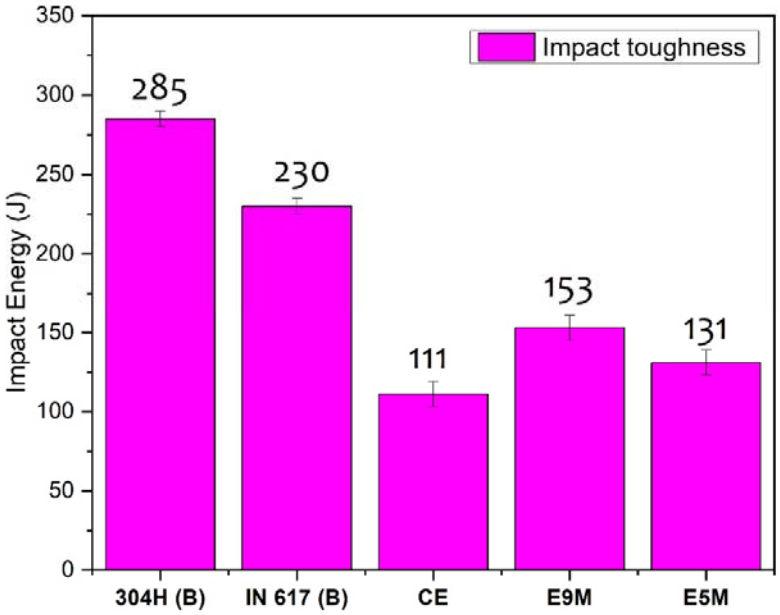

Figure 5.43. Impact toughness results in 2nd system

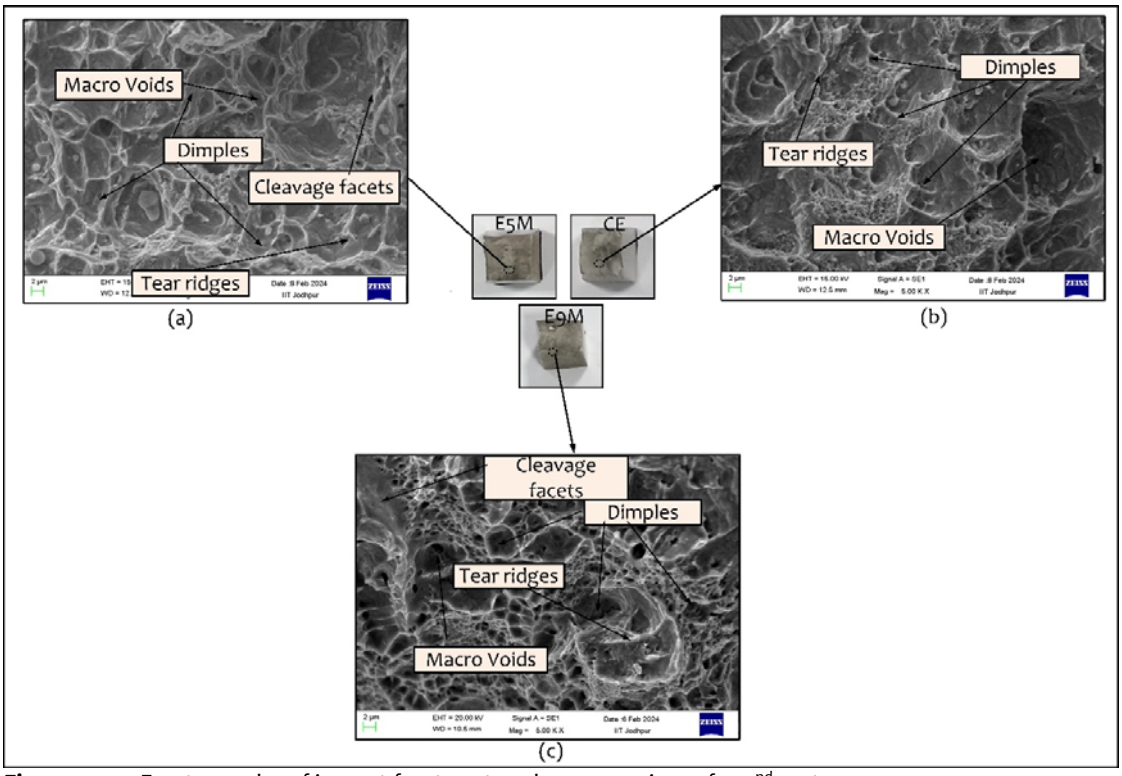

Figure 5.44. Fractography of impact fracture toughness specimen for 2nd system

The microhardness profile across the IN617BM, IN617 HAZ, weld fusion zone, 304H BM, and 304H HAZ region for fabricated weld using laboratory-developed and commercial electrodes is shown in Figure 5.45. The distance between each indentation was 1.0 mm. The OriginPro 8 was used to plot the microhardness profile. The reference point, with x=0, was the weld center. To get the hardness value, the weld center was measured longitudinally.

The longitudinal direction of the weld center was used to measure the hardness value. Microhardness distribution profiles that are not uniform provide further evidence of microstructure heterogeneity. The hardness value of the SS304H BM was found to be lower than the IN617 BM. The IN617, 304H BM, and weld E10M micro-hardness values were 240±5 HV, 230±5 HV, and 251±5 HV, respectively. The average hardness values for microhardness are presented in Table 5.17. The variation in hardness value was mostly caused by the refined grain structure with columnar dendrites and the presence of a suitable amount of carbide dispersed throughout the grain matrix (Pandey, 2020). The weld hardness increases due to the dendrite formation and segregation of alloying element. Welds created with commercial electrodes had greater hardness values recorded in the microhardness profiles compared to welds formed with electrodes coated E10M, which had lower values. It has been noted that electrode coatings with a higher CaO concentration tend to be harder, whereas electrode coatings with a lower SiO_2 content tend to be softer (Bhandari et al., 2019). This may be related to the fact that welds made with E10M coatings tend to be less hard than other fabricated welds.

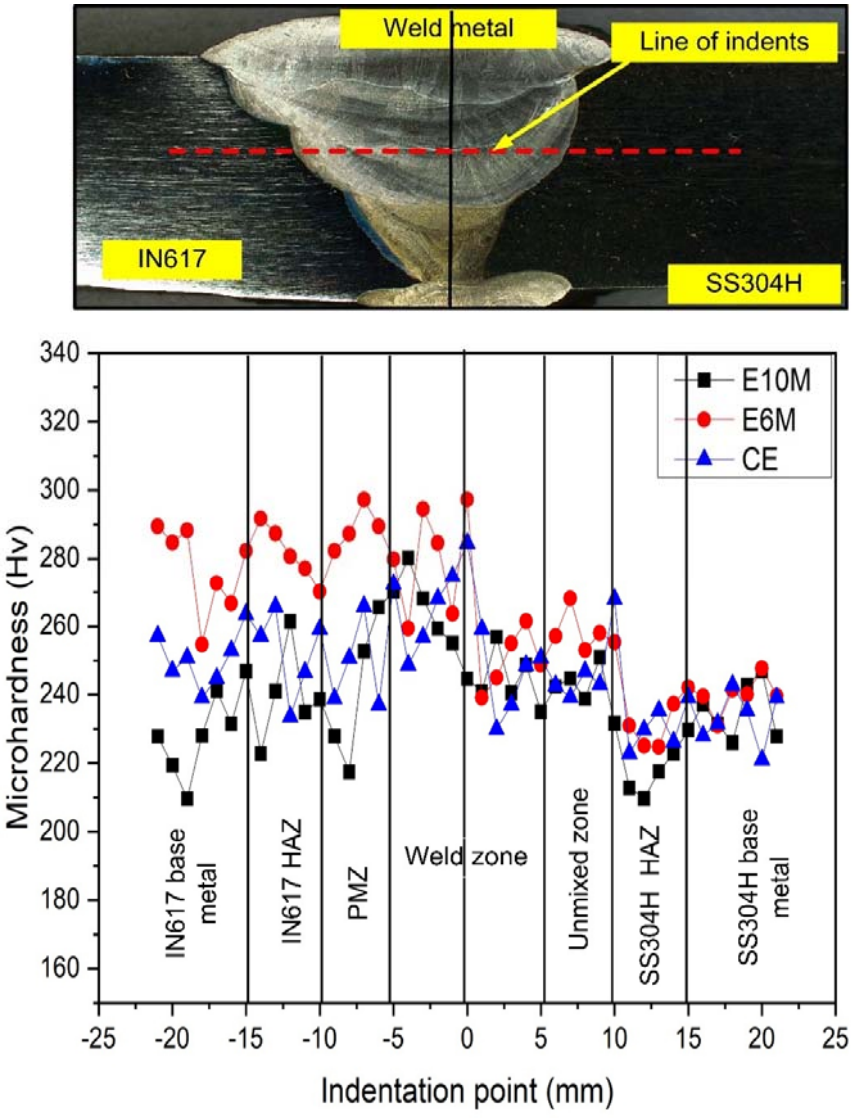

Figure 5.45. Microhardness profile of different welds for 1st system

Table 5.17: Microhardness values across the different region of welds for 1st system

	Base IN617	IN617 HAZ	PMZ	Weld	Unmixed	304H HAZ	304H base
CE	253	244	251	257	243	239	233
E10M	240	241	245	251	240	222	230
E6M	282	289	298	279	293	232	260

Similarly, the microhardness variation profile of different fabricated welds for 2nd system is shown in Figure 5.46. The average value of microhardness across various region is summarized in the Table 5.18.

Table 5.18: Microhardness values across the different region of welds for 2nd system

	Base IN617	IN617 HAZ	PMZ	Weld	Unmixed	304H HAZ	304H base
E5M	281	276	289	277	262	261	241
E9M	228	218	212	228	219	217	202
CE	253	244	251	257	243	239	233

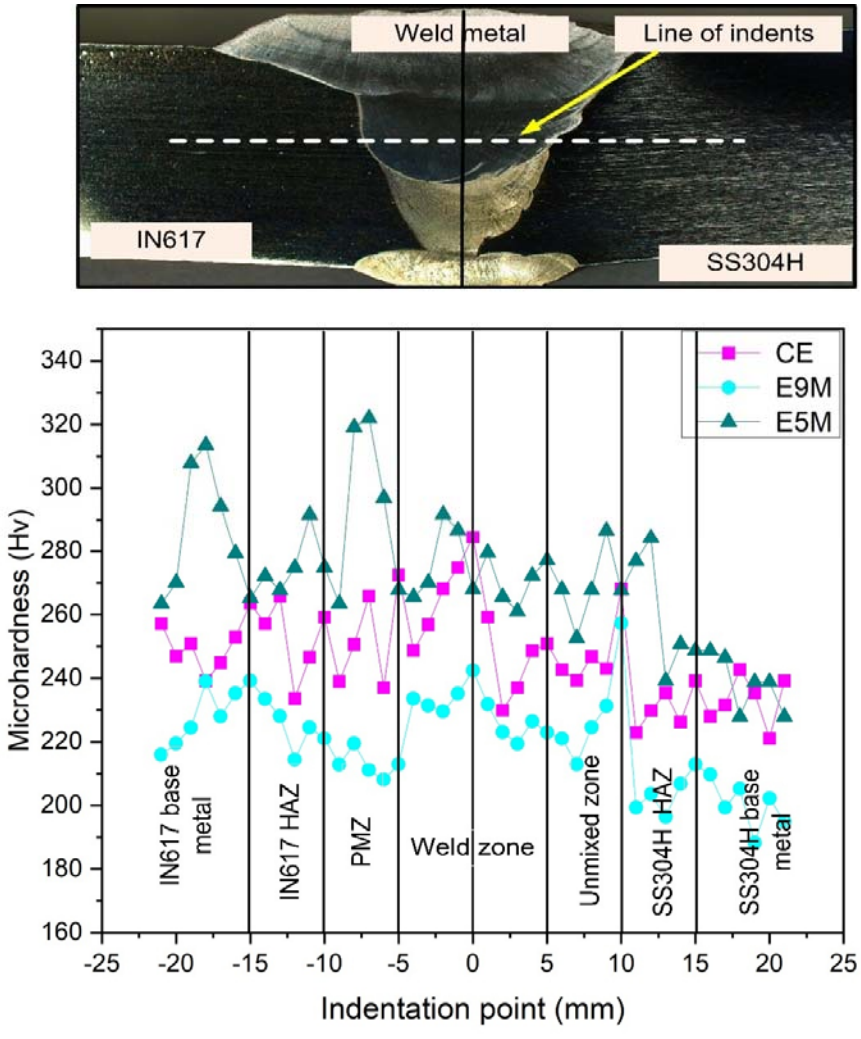

Figure 5.46. Microhardness profile of different welds for 2nd system

5.10.5 Hot corrosion investigations on IN617/304H DWJ

Specimens were cut from the center of the produced welds and base materials to conduct the hot corrosion studies in the presence of salt mixes (SM1, SM2). The detailed steps for preparing the material and conducting the experiments were covered in section 4.5.8. The oxidation kinetics were investigated using thermogravimetric analysis on the prepared specimen. The corroded specimens were characterised using X-ray diffraction and SEM/EDS analysis.

5.10.5.1 Thermogravimetric analysis

Experiments were conducted to study the hot corrosion of base materials and fabricated welds at 850°C in the presence of different salt combinations. Fig 5.47 (a) and (b) represent the weight changes per unit area versus no of cycles (exposure time) for different samples exposed under salt SM1 and SM2. Thermogravimetric graphs show that the oxidation rate drops and remains constant with increasing exposure time for all salt solutions. The parabolic rate constant (K_p) for all specimens was determined by the slope of the curve fitting using the equation $(\Delta W/A)^2 = K_p\, t$ at the studied duration and temperatures, where $(\Delta W/A)$ represents the weight changes, K_p is the parabolic rate constant, and t is the exposure time. The values of the parabolic rate constant (K_p) for different specimens under the given conditions are shown in Table 5.19. It was observed from Figure 5.47 (a) and (b) that the nature of the specimens follows the parabolic rates. It was reported that higher the value of parabolic rate constant (K_p) lower the corrosion resistance and vice versa. This shows that the parabolic rate (K_p) for weld E9M, and E10M is lower as compared to commercial weld for salt mixture (SM-1). Similarly, the parabolic rate (K_p) for weld made with laboratory developed electrode is lower than CE for salt mixture (SM-2) when exposed to hot corrosion at 850 °C. This means that the weld produced using the developed electrodes will be more resistant to hot corrosion than the ones produced using commercial electrodes. A thermal diffusion mechanism is seen in high-temperature parabolic oxidation, suggesting that it regulates the reaction rate (Yuan and Wang, 2010). In case of Ni based welds, there was a quick rise in weight change when V_2O_5 was present and a gradual rise in weight change when it was absent at the exposed temperatures. By creating a eutectic mixture over 650 °C, vanadate, sulfur, and chlorides increase the corrosion rate. Oxidation and the formation of oxide layers with micro pores or cracks are the initial reactions of surfaces exposed to corrosive environments. This makes sense when we consider that molten vanadate when deposited on a metal surface, undergoes oxidation and forms oxide scales and passive layers when heated to higher temperatures. Vanadate causes the oxygen to diffuse more quickly through the fused salt on the metal surface (Khan et al., 2015). Figure 5.47 shows that specimens exposed to molten salt solutions at 850°C acquire weight during the first few cycles, and slower corrosion rate occur as the number of cycles increases. It was reported that more weight gain observed in case of commercial weld while E9M weld weight gain was recorded as the lowest. This indicates that laboratory-developed electrodes welds accumulate less weight compared to commercial electrodes. Specimens subjected to SM2 gained more weight than those exposed to SM1 at temperature of 850°C. Corrosion occurs at high temperatures, often between 700 and 950 °C. This form of corrosion incorporates the incubation and propagation processes. Since alkali metal salts like NaCl and Na_2SO_4 have high thermodynamic stability, they condense on surfaces and cause corrosion. After penetrating the protective oxide layer, the salts reach the metal. Substrate chromium depletion speeds up base material oxidation, leading to the formation of a porous scale. Sulfides also develop behind the protective oxide during this kind of corrosion. Characteristics of this type of corrosion include the following: a chromium depletion zone, internal sulphidation, and an exterior oxide scale that is both porous and non-protective, with internal oxides beneath. At high temperatures, metals are lost in corrosion

environments when chloride is present, either alone or together with sulphates to generate volatile chlorides, which are far more dangerous. The report states that chlorides can speed up corrosion by migrating into materials (Birks et al., 2006; Reid, 1971). The basic electrodes can minimise the hydrogen level of the molten weld pool. This results in high-quality welds with improved structural integrity. Basic coatings try to reduce high-stress locations that can lead to early weld failure. Welds with Cr and Ni exhibit enhanced corrosion resistance. Laboratory-developed electrodes result in greater Cr and Ni content in produced welds than commercial electrodes, according to investigations.

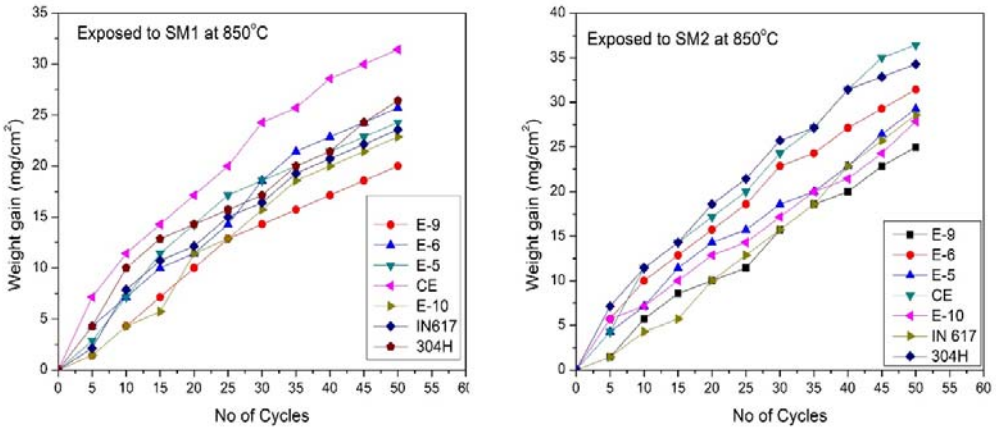

Figure. 5.47 (a,b) Weight change/ area (mg/cm²) vs. no of cycles subjected to hot corrosion for 50 cycles at 850 ◦C under different (SM1 and SM2) salt environments

Table 5.19 Parabolic rate constant (K_p) values for different environment

Substrate	Kp (10^{-10} g^2 cm^{-4} s^{-1}) SM-1	Kp (10^{-10} g^2 cm^{-4} s^{-1}) SM-2
IN 617	0.326	0.454
304H	0.374	0.704
E10M	0.319	0.406
E6M	0.401	0.569
CE	0.585	0.777
E5M	0.348	0.459
E9M	0.237	0.353

5.10.5.2 XRD analysis of welds

XRD analyzed the corroded samples to identify the phases on the surfaces of all the specimens after exposure to different salt environments. Figures 5.48 (a) and (b) represent the different phases that were present on the corroded surface. The XRD analysis revealed the presence of Cr_2O_3, NiO, Fe_2O_3, $NiCr_2O_4$, and $FeCr_2O_4$ spinel as the major and minor phases on the specimen's surface. In the welded samples, the distinct oxide layers of Cr_2O_3 and NiO along with a dense spinel of chromium rich with combination of nickel and iron forms a protective coating layer when chromium reacts with hematite and nickel oxide at high temperatures (Kamal et al., 2010). This indicate that the corrosion rate slow down due to the formation of protective layers. The oxide scale that forms on specimen is often thin, compact, and adherent. The thermodynamics and kinetics of the reactions between the alloy constituents and the corrosive species present in the environment drive the formation of these phases. Further sulphidation and oxidation of the grain boundaries can be caused by the inner anion migration of oxygen (O^{2-}) and sulphur (S^{1-}) in corroded specimens. The corrosion rate is increased because these grain boundaries facilitate the migration of cations and anion along rapid diffusion pathways. Since sulphides are far more corrosive than

oxides, elemental sulphur has a far greater impact than oxygen. (Ghosh and Mitra, 2014) found that cations, mostly iron, may quickly diffuse outward via sulphides, leading to an aggressive corrosion assault.

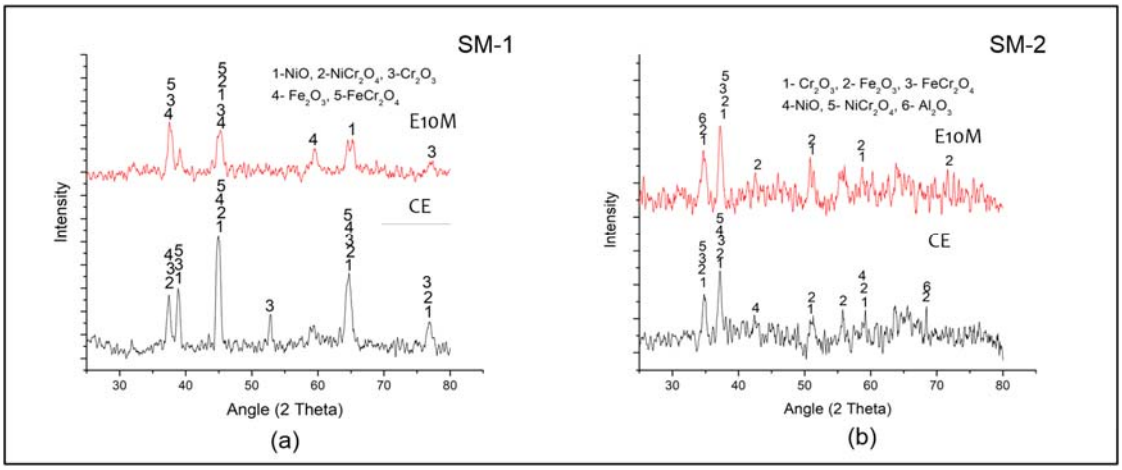

Figure. 5.48 XRD graph of corroded specimens

5.10.5.3 Surface morphology of oxide scales

Scanning electron microscopy (SEM) photographs are used to examine the surface morphology of the oxide scale on the corroded specimens subjected to salt environments for 50 cycles at 850 °C. Figure 5.49 and 5.50 show the SEM images for surface analysis of weld E10M after cyclic hot corrosion exposed to different salt mixture. The specimen's surface scale has a distinct nodular structure. The surface of the samples showed signs of oxide spalling and wrinkles (Figure 5.49 a). When a compressive force acts laterally within a scale, it causes the oxide to develop, which in turn causes the oxide scale to spall and wrinkle (Kamal et al., 2010). The formation of oxide scale on the surface is more consistent in samples containing vanadium in the salt combination than in those that do not contain vanadium (Figure 5.50a). When exposed to a salt mixture containing vanadium, samples developed cracks and porous oxide scales on their surface. Hence, oxygen penetrates more to the substrate, which causes a high oxidation rate. At high temperatures, the oxidation process coats the samples with nodular oxides. At higher magnification, the morphology of oxide scales formed is well structured and layer-wise. The EDAX analysis of scale weld E10M reveals the presence of O, Cr, and Ni-rich elements, hence suggesting the formation of NiO, Cr_2O_3, and spinels ($NiCr_2O_4$, $FeCr_2O_4$). The presence of these phases was supported by XRD analysis. Similarly, the scale formed on the weld CE corroded samples (Fig 5.51 and 5.52) depicts the presence of O, Cr, and Ni-rich elements, therefore, Cr_2O_3 and Cr-rich spinel in combination with nickel and iron phases formed. XRD also supports the formation of phases. At higher magnification, figure 5.51 shows the morphology of the scale, which is a needle-like shape with cracks and porous. The diffusion of more Fe from the substrate into oxide scales occurs on the surface, which enhances the corrosion rate and weight change. It also reported less chromium content compared to E10M specimen due to which less corrosion resistance occurs.

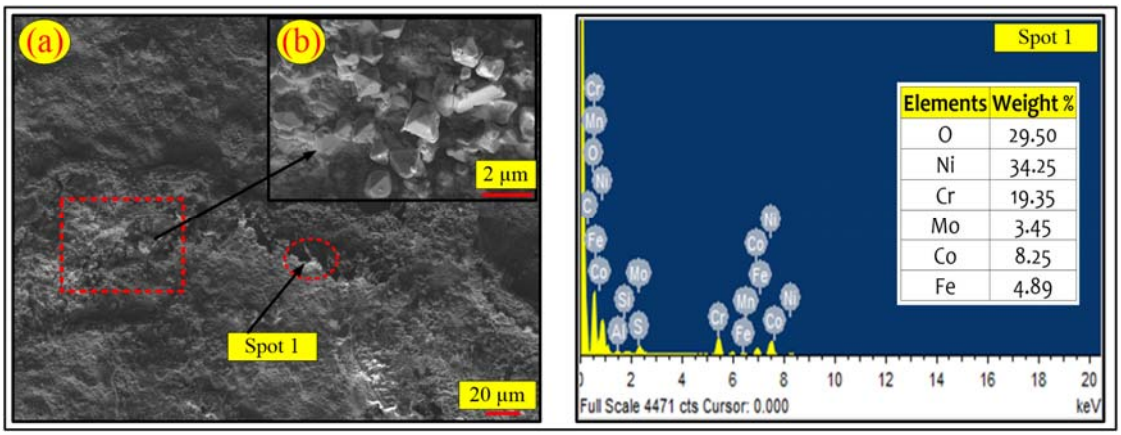

Figure.5.49 Surface scale analysis and EDAX for weld E10M specimens exposed to salt mixture (SM1)

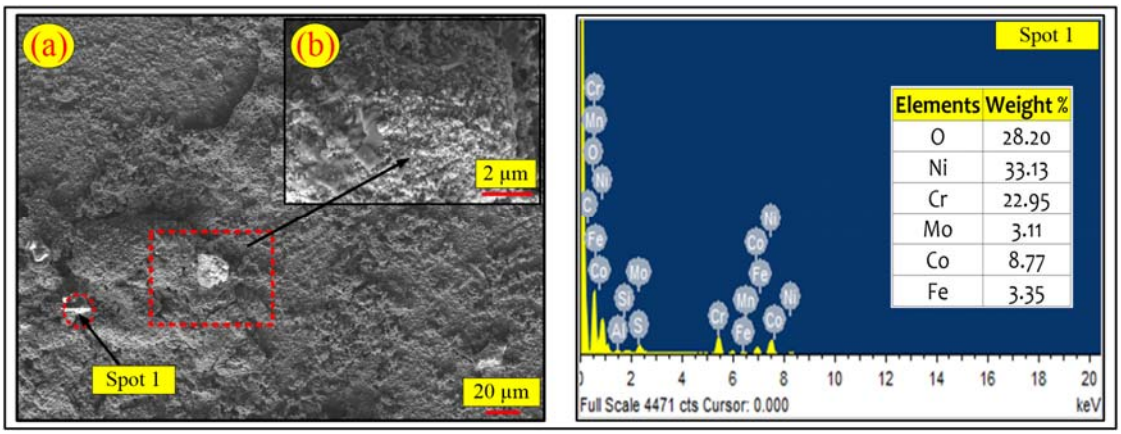

Figure.5.50 Surface scale analysis and EDAX for weld E10M specimens exposed to salt mixture (SM2)

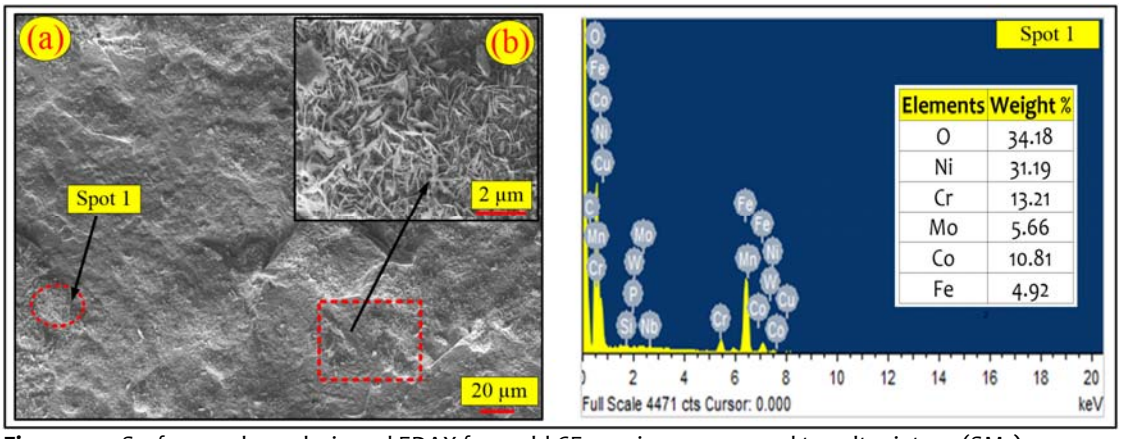

Figure.5.51 Surface scale analysis and EDAX for weld CE specimens exposed to salt mixture (SM1)

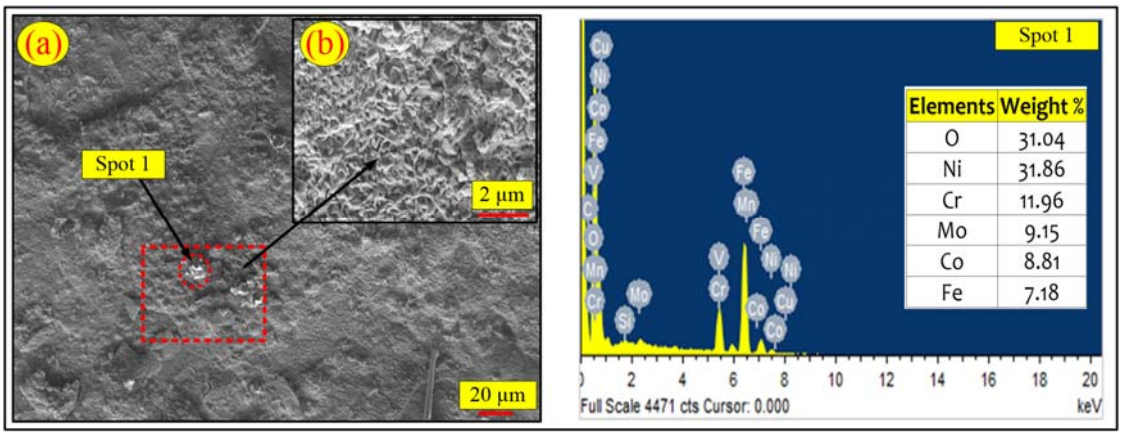

Figure.5.52 Surface scale analysis and EDAX for weld CE specimens exposed to salt mixture (SM2)

5.10.5.4 Cross-sectional analysis of oxide scales

The corroded samples were cut across the cross-sections using a precision cutter at a slow speed. They were then embedded in resin and polished to achieve a mirror-like finish. SEM/EDAX analysis was carried out at several points of interest along the cross-section of corroded weld E10M and weld CE samples; the results are depicted in Figure 5.53 - 5.56. In all the cases, a thin, dense, compact oxide scale formed on the corroded sample, maintaining its compact nature. SEM/EDS back-scattered micrograph with elemental analysis taken across the cross-section of the corroded E10M samples in molten salt mixture 1 indicates the top surface of scale (Fig 5.53, point 1), mainly composed of O, Ni, and Cr-rich elements. Further oxygen decreases from the subscale region to the weld, and Ni and Cr-rich elements are observed. It is clear from the EDAX analysis, as evident at point 3 (Fig. 5.53), that Cr and Ni inter diffusion occurs from oxides into the substrate and vice versa. This indicates the existence of chromium and nickel oxides and their spinel oxides, which act as a protective barrier against corrosion, which is also supported by XRD examination. The oxide scale formed on the top surface is homogenous, thin, and compact. Cross-sectional analysis of the corroded E10M samples in the salt mixture 2 (having vanadium oxides) (Fig.5.54) showed that the top surface of the scale mainly consists of uniform, porous, and adherent. The scale at point 1 is mainly consisting of oxygen, nickel, and chromium-rich elements. This indicates the formation of chromium and nickel oxides and their spinel oxides, and the existence of these phases is confirmed by XRD analysis. At point 3, the oxygen percentage decreases, and the nickel-chromium percentage increases in the weld. Hence, it suggests the dark and light regions corresponding to the Cr and Ni-rich area (Kamal et al., 2009). The inter diffusion of chromium and nickel occur from oxides to weld and weld to oxides respectively, as shown from EDAX at point 3. The thickness of the oxide scale is higher than that of salt mixture 1, which is thereby supported by line mapping.

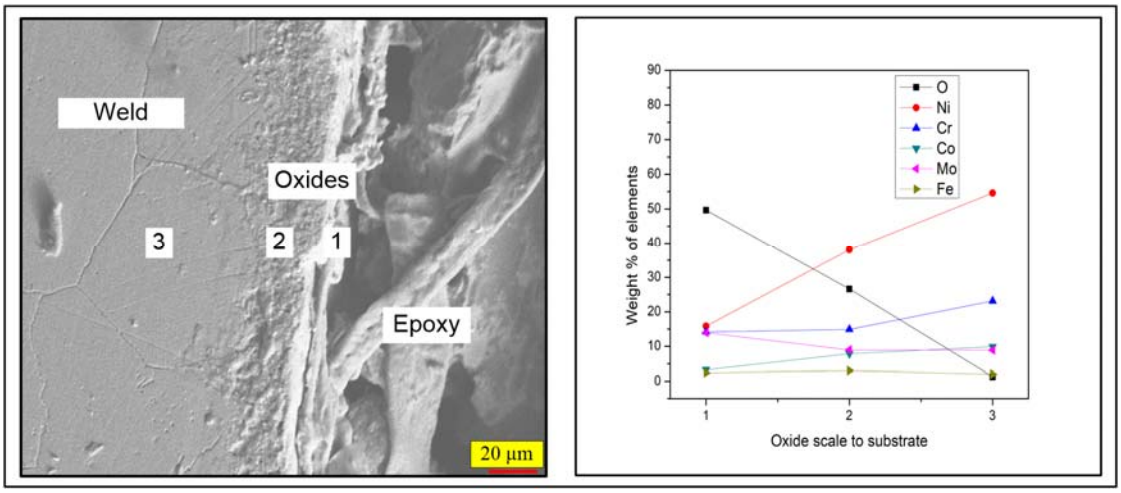

Figure.5.53 Oxide scale morphology and variation of elemental composition across the cross-section of weld E10M specimens exposed to salt mixture (SM1)

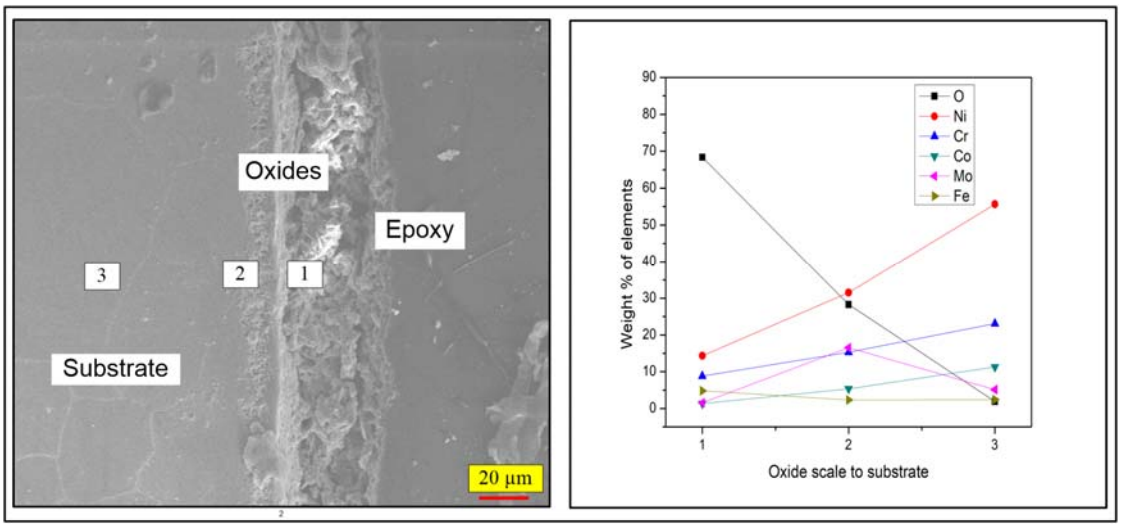

Figure.5.54 Oxide scale morphology and variation of elemental composition across the cross-section of weld E10M specimens exposed to salt mixture (SM2)

SEM/EDS back-scattered micrograph with elemental analysis taken across the cross-section of the corroded weld CE samples in molten salt mixture 1 (having higher chlorine content) (Fig 5.55) shows a thin, homogenous, and porous oxide layer. The chloride-rich deposits can cause scale spallation, resulting in a higher corrosion rate. The oxide scale (point 1) mainly consists of nickel, oxygen, and chromium-rich elements. Hence, it suggests the formation of chromium oxide, iron oxide, along with spinel as a predominant phase, which is to be supported by XRD analysis. Figure 5.55 shows that the oxygen concentration decreases and Fe, Ni, and Cr content rise as one move from an oxide scale area to the weld region (point 3). This merely depicts the elemental transfer at the specimen's surface as the molten salt fluxes during the hot corrosion process. The inter diffusion of nickel, iron and chromium takes place from oxides to weld and weld region to oxides, respectively, as evident from EDAX at point 3. The oxide scale thickness is lower than that of salt mixture 2, which is supported by line mapping of cross-section. Similarly, cross-sectional analysis of the corroded CE samples in the salt mixture 2 (Fig.5.56) showed that the top surface of scale (point 1) mostly consists of uniform, compact and adherent scales mainly consisting of O, Ni, Fe and Cr-rich elements. This indicates the formation of iron and chromium oxides and their spinel oxides, which provide protective spinel coatings and phases present, as confirmed by XRD analysis. A higher concentration of chromium content in the oxide scale

leads to the formation of chromium spinel-protecting coating and improves corrosion resistance. (Ren et al., 2005) reported that $NiCr_2O_4$ spinel can be formed through a solid phase reaction involving NiO and Cr_2O_3 on oxide scales. This process aids in developing oxidation resistance since the spinel phase typically has lower cation and anion diffusion coefficients than the parent oxides (Chatterjee et al., 2001). The presence of chlorine and vanadium an oxidising environment causes the formation of oxide scale that is crack, and porous. Scale with pores improves oxygen accessibility and the reaction with substrate occurs, leading to increased corrosion (Nielsen et al., 2000; Skrifvars et al., 2010). The weld specimen that was subjected to SM2 developed a porous, thick, and non-adherent oxide scale. The cracks and pores show near the oxide scale and metal surface. This causes higher corrosion rate to occur in SM2 environments than in SM1. Eutectoids with a low melting point are formed when alkali sulphate is heated with vanadium and chlorine.

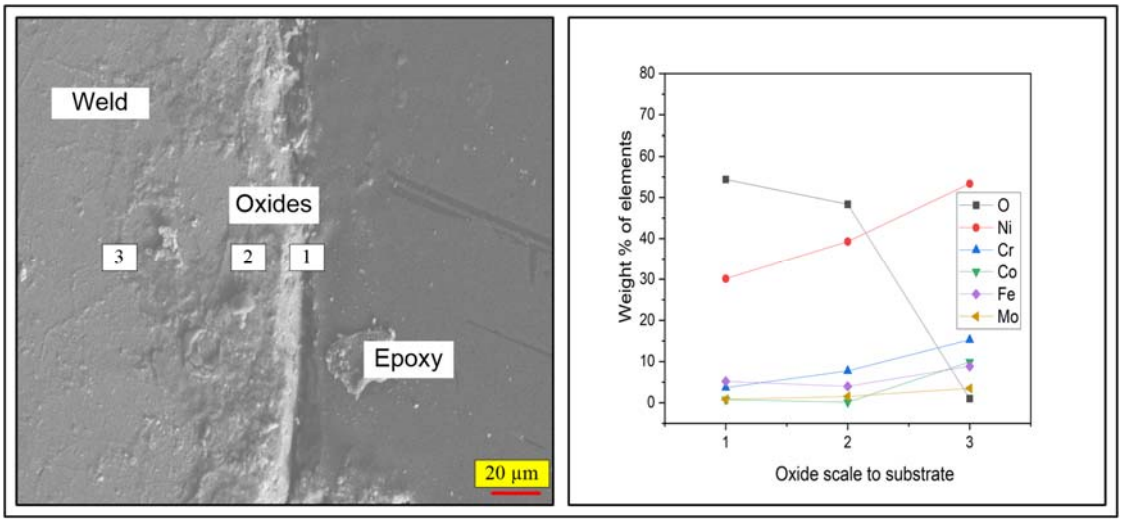

Figure. 5.55 Oxide scale morphology and variation of elemental composition across the cross-section of weld CE specimens exposed to salt mixture (SM1)

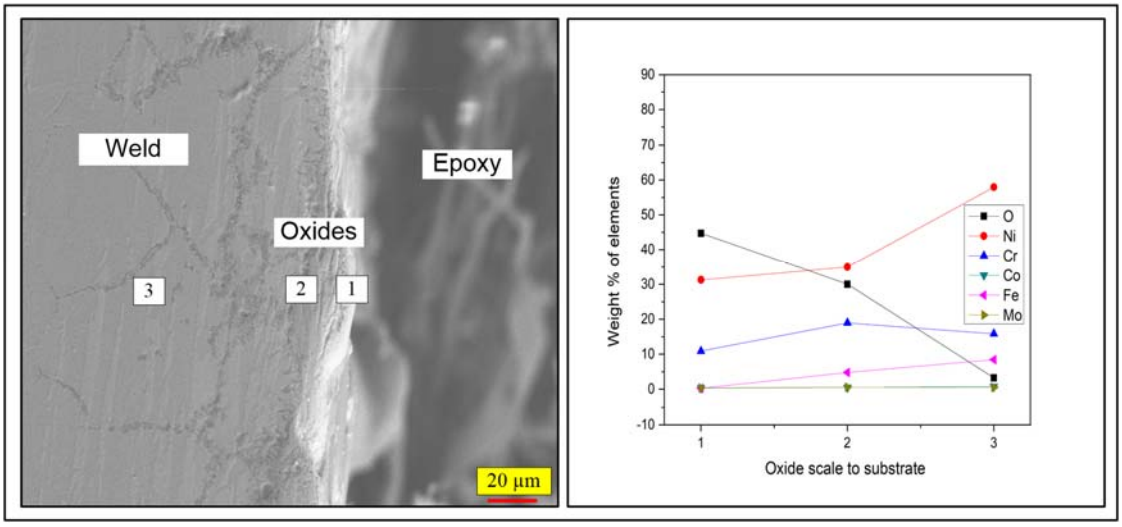

Figure. 5.56 Oxide scale morphology and variation of elemental composition across the cross-section of weld CE specimens exposed to salt mixture (SM2)

5.10.5.5 Line scale mapping analysis

A precision cutter cut the corroded samples across the cross-sections slowly. After that, it was mounted it in resin, polished it to achieve a mirror-like finish, and applied silver paste between the stub and sample to ensure conductivity. Gold sputtering was used to

facilitate the line scan mapping analysis of elements present across the oxide scale. Backscattered images with line scan mapping of weld E10M and CE samples exposed to salt environments 1 and 2 are shown in Figure. 5.57-5.60. The E10M specimen showed a higher oxide scale thickness (37.05µm) when exposed to salt 2 compared to salt 1, while the weld CE sample showed a lower scale thickness (24.07 µm) when exposed to salt 1 compared to salt 2. It was evident that due to the crack and porous oxide scales, more oxygen penetrates the substrate, and inter diffusion occurs between the corrosive gases and substrate. The cracking and spalling of scale occur due to the difference in the thermal coefficient in scale; further internal oxidation produces more stress, which causes the scale to break (Niranatlumpong et al., 2000). Figure.5.57-5.60 shows the distribution of elements throughout the substrate and oxide scale for both weld E10M and CE. It also indicates the variation of scale thickness formed after the hot corrosion.

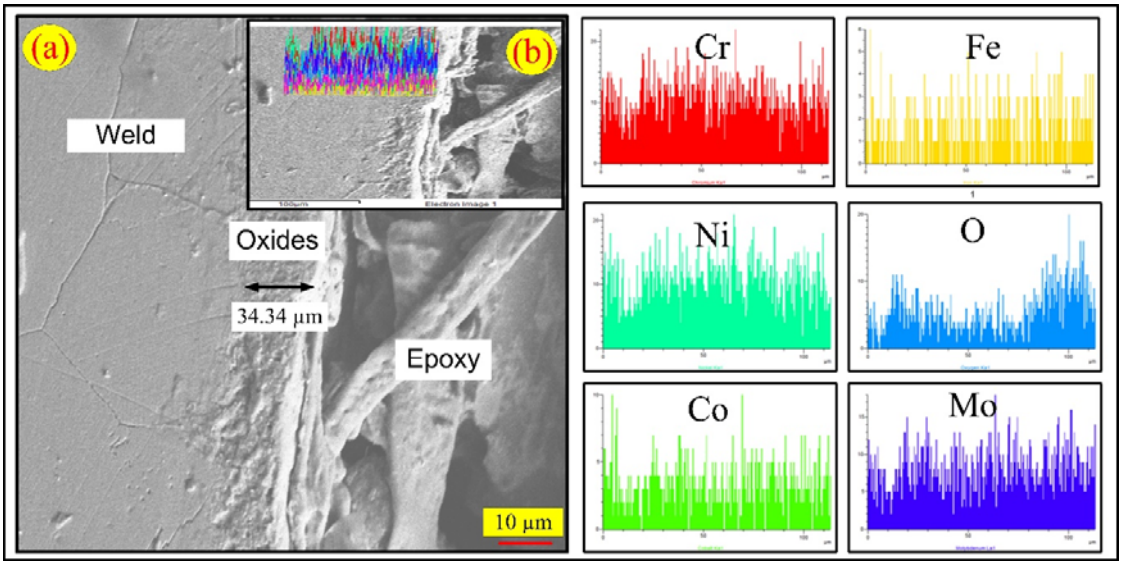

Figure. 5.57 Back scattered image and line scan mapping on the weld E10M specimen exposed to salt mixture (SM1)

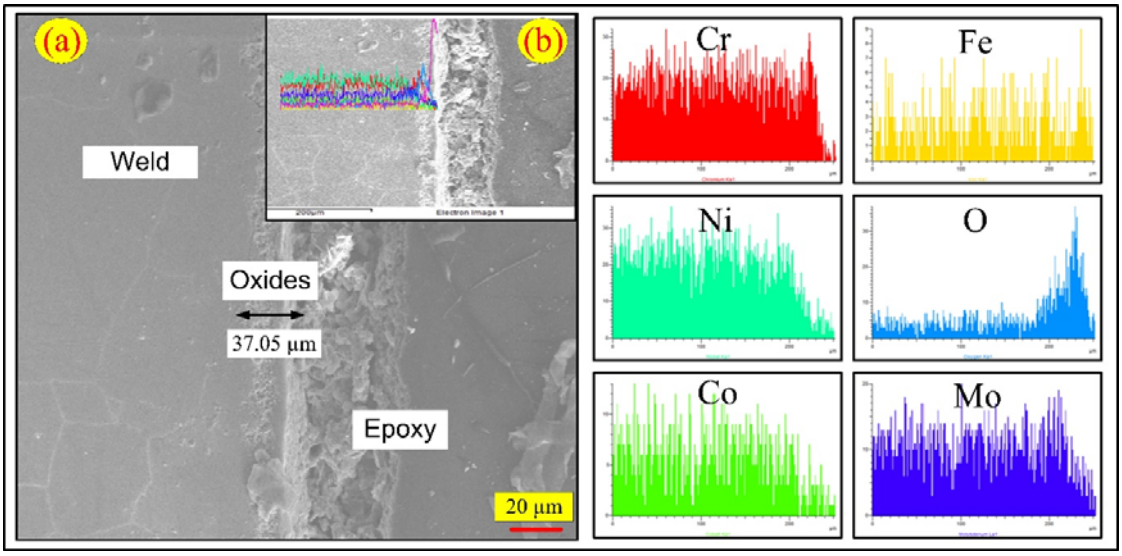

Figure. 5.58 Back scattered image and line scan mapping on the weld E10M specimen exposed to salt Mixture (SM2)

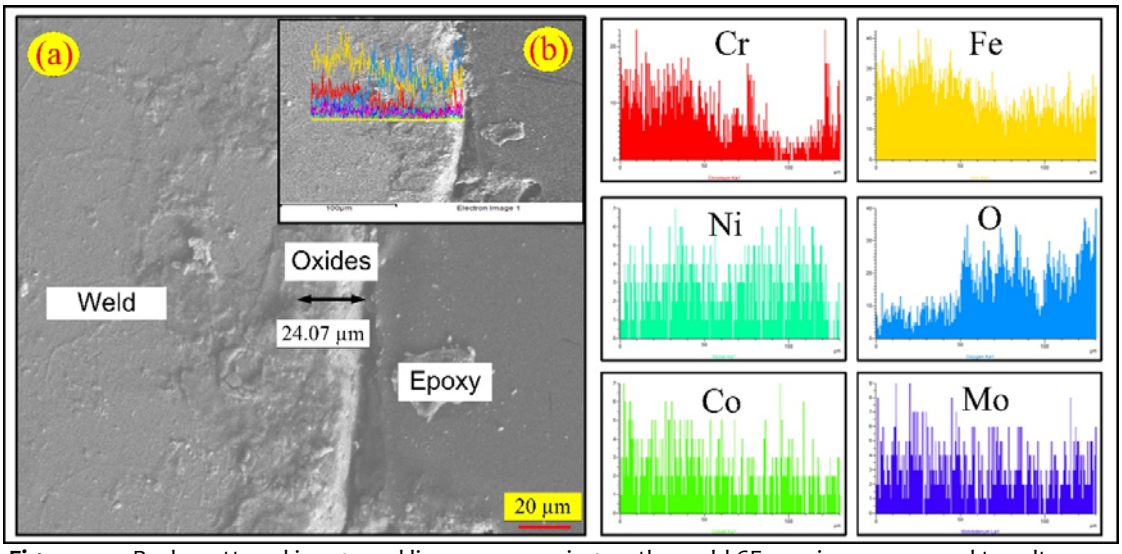

Figure.5.59 Back scattered image and line scan mapping on the weld CE specimens exposed to salt Mixture (SM1)

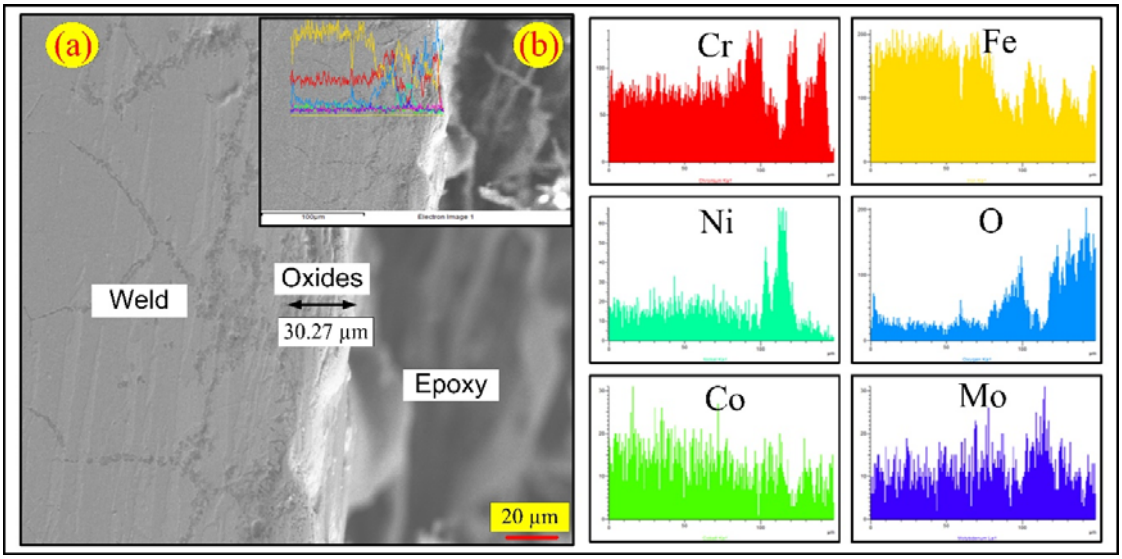

Figure. 5.60 Back scattered image and line scan mapping on the weld CE specimens exposed to salt Mixture (SM2)

5.11 Environmental implications of the developed electrodes

5.11.1 Welding fume measurement

The airborne emissions from the welding process pose significant risks to both welders and the environment. The operator's risk is directly linked to the dose of toxic substances inhaled from the fumes, while the environmental risk depends on the emission rate and concentration of contaminants released into the atmosphere. Numerous studies have reported the hazardous effects of welding fumes' particle size, shape, and biological activity on human health and the environment (Beach et al., 1996; Han et al., 2016; Rahul et al., 2021). In the present study, two different grades of experimental electrodes were developed with the primary objective of enhancing mechanical performance. These electrodes were tested for fume emissions to evaluate their environmental impact and health hazards to workers. The Fume Formation Rate (FFR) signifies the concentration of welding fume in a confined workplace with hardly any ventilation. It calculates how much fume a certain consumable

emits in a given time under established welding conditions. Bead-on-plate welding was carried out on circular base plates inside the fume test chamber, constructed according to the guidelines of the American Welding Society (AWS) ISO 15011-1, 2009 (ISO 15011-1(2009)). Figure 5.61 illustrates the fume test chamber used for the study. Before welding, the base plates were thoroughly cleaned using a wire brush to remove dust and rust. Welding was performed by a trained welder using a RILION ARC 400 constant-current DC rectifier set to 100 A.

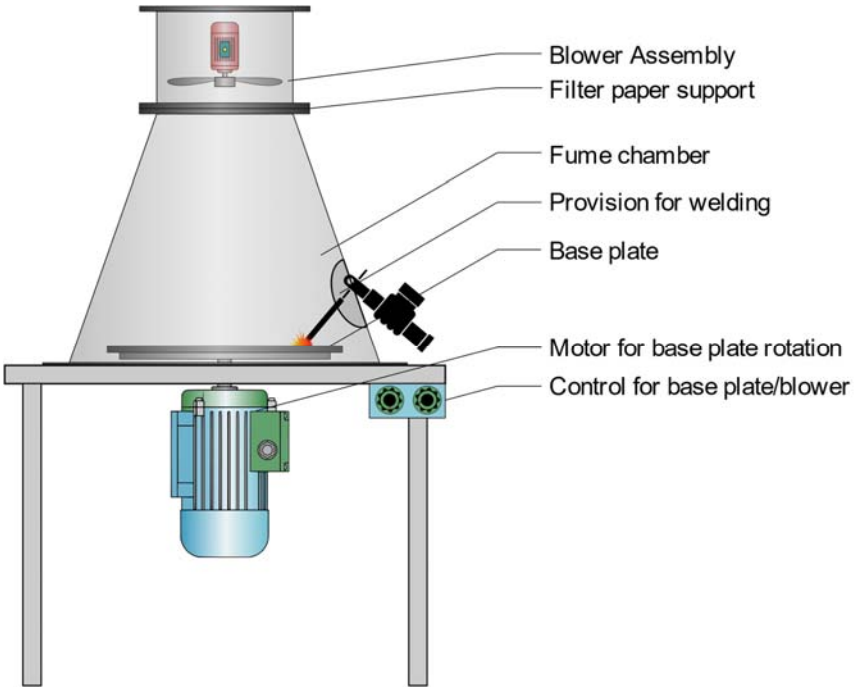

Figure. 5.61 Schematic Diagram of Fume Test Chamber (Madhusoodhanan et al., 2022)

The process was conducted at a welding speed of 15 cm/min**,** with an average feed rate of 18 cm/min and an electrode pull angle of 15°–30°**.** The generated fumes were extracted at a flow rate of 900 L/min and collected on a 253 × 204 mm Whatman GF/A filter paper with a pore size of 1.6 µm**.** To enhance collection efficiency, the extractor fan was operated for an additional 90 seconds after the initial 60 seconds of welding. The Fume Formation Rate (FFR) was determined based on the weight difference of the filter paper using Equation 5.18.

$$\text{Fume formation rate (FRR)} = \frac{F_w - I_w}{\text{t}}\ g/min \qquad \text{Eq. (5.18)}$$

Where, I_w denotes the initial weight of filter paper, F_w denotes the final weight of filter paper, and 't' represents the time taken for welding. The fume collection and measurement were carried out in triplicate for each type of electrode, and an average value of FFR was recorded. Figure 5.62 shows the fume emission rates of commercial and laboratory developed electrodes. The results indicate that the developed electrodes demonstrated a substantial reduction in fume emissions compared to commercial welding electrodes. The experimental combination E9M achieved a 24.57% reduction in the fume formation rate (FFR), while E10M exhibited a remarkable 44.72% reduction compared to its commercial counterparts. The novel flux formulations used in the experimental electrodes contribute to lower fume emissions and superior mechanical properties compared to conventional electrodes. Among the tested combinations, the experimental electrode E10M exhibited the better mechanical properties, followed by E9M. This enhancement is obtained through the optimized flux

composition, which improves elemental transfer efficiency, particularly for Ni, Mo, Co, and Mn, facilitating their incorporation into the weld bead rather than forming fumes.

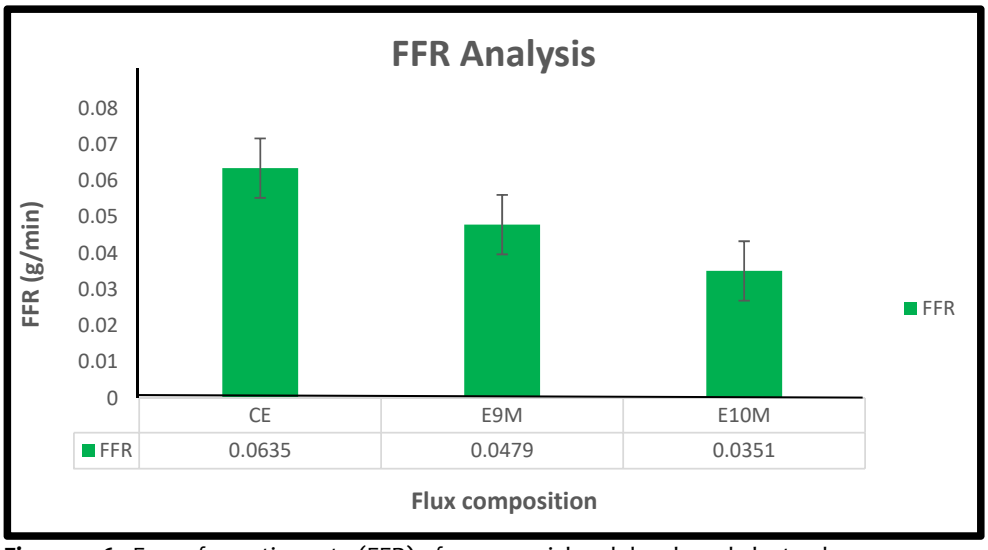

Figure. 5.62 Fume formation rate (FFR) of commercial and developed electrodes.